Universiteit Utrecht

ISES

Netherlands Research Centre
for Integrated Solid Earth Science

The intriguing geometry of the Central Iberian Orocline: a combined paleomagnetic and structural approach

Msc. Thesis

Subject:	Master Thesis, 2nd version
Date:	18-11-2014
Student:	Thomas Groenewegen
1st supervisor:	Dr. Daniel Pastor Galán
2nd supervisor:	Prof. Dr. Wout Krijgsman

Table of contents

Abstract

The Variscan Belt in Iberia forms an "S" shape double orocline. The northern orocline, the Cantabrian Orocline (CO), is kinematically constrained as a secondary orocline and thought to be a thick-skinned feature. The geometry, kinematics and mechanism of formation of the southern orocline, the Central Iberian Orocline (CIO), are still unclear. Several geometries have been proposed for the CIO, most of them suggesting that the Morais allochthonous complex (NE Portugal) is in its core and that the axial trace is parallel to the fold axis of the last major Variscan deformation phase. The aim of this study is to get better constraints on the geometry and kinematics of the CIO, by combining paleomagnetic directions from the hypothesized hinge with structural analyses of an outcrop in the core of the orocline.

Paleomagnetic directions indicate that no differential rotations occurred around the hypothesized hinge zone. The directions from syn-kinematic granites and the Cambrian Tamames limestone formation range from ENE to SE, while post-kinematic granites have directions pointing to the SE. The range of directions is interpreted as a remagnetization during rotation, which is happening because of the intrusion of the post-kinematic granites. This constrains the timing of rotation to the age of the post-kinematic granites, which is between 310 and 298 Ma. No differential rotations were observed around the hypothesized hinge. The ENE direction is similar to directions from the southern flank of the CO, while the SE direction represents the Permian direction and the end of rotation.

Structural analyses indicate that three phases of deformation affected the studied outcrop. Deformation phases D_1 and D_3 are quasi-coaxial, whereas perpendicular directions would be expected in the hinge zone if the orocline is the result of buckling of an originally straight mountain belt. This implies that the orocline is not formed by buckling because of D_3 deformation.

The results from the paleomagnetic directions and the structural analysis are consistent and indicate that the CIO is not a secondary orocline with the Morais complex in its core. Instead, the studied area forms part of the southern limb of the CO. This means that the geometries proposed by previous authors are not compatible with the data presented in this study. Therefore, taking into account the new data from this study, three new possible geometries for the CIO are proposed.

Introduction

Oroclines, which are mountain belts that are curved in map-view, are the largest-scale folds on Earth (Carey 1955). Oroclines are important structures in the Earth-system, although many open question remain regarding their geometry and formation (Johnston et al. 2009). It is important to know whether an orocline is thin-skinned or thick-skinned, since ore deposits could form if the mantle is involved. Understanding the geometry and kinematics of oroclines is also important for tectonics, since most models assume that plates are rigid, while oroclines can represent up to thousands of kilometres of intra-plate shortening (Pastor-Galán et al. 2012; Weil et al. 2013). Furthermore, understanding the timing and the amount of rotation related to oroclines is crucial for making correct paleogeographic reconstructions, since rotations can have influence on the position of tectonic terranes, microcontinents or even full continents.

The Central Iberian orocline (CIO; Aerden 2004; Martínez Catalán 2011b; Shaw et al. 2012) forms a crucial part of the European Variscides (*figure 1*), since understanding its geometry and kinematics is fundamental for understanding the amalgamation of Pangea. If the CIO is a secondary orocline, formed because of late-orogenic processes, a major revision of the Variscan orogeny is needed. This would require a new plate-tectonic configuration for that time, with the Rheic ocean in a different position relative to Gondwana. A secondary orocline would also imply a westward continuation of the Variscan orogeny. If the CIO is not a secondary orocline, this would be consistent with the configuration of the Variscan orogeny that is currently accepted in literature, with the Rheic ocean in the position as illustrated in *figure 1*. On a smaller scale, the scale of Iberia, the geometry and kinematics of the CIO have implications for possible resources, depending on the exact geometry and whether the CIO is a thick-skinned or a thin-skinned feature.

The CIO forms the south-western end of the Variscan belt in Europe, which comprises several other oroclines as well, such as the Bohemian Orocline in Central Europe (Franke & Zelazniewicz 2002), the

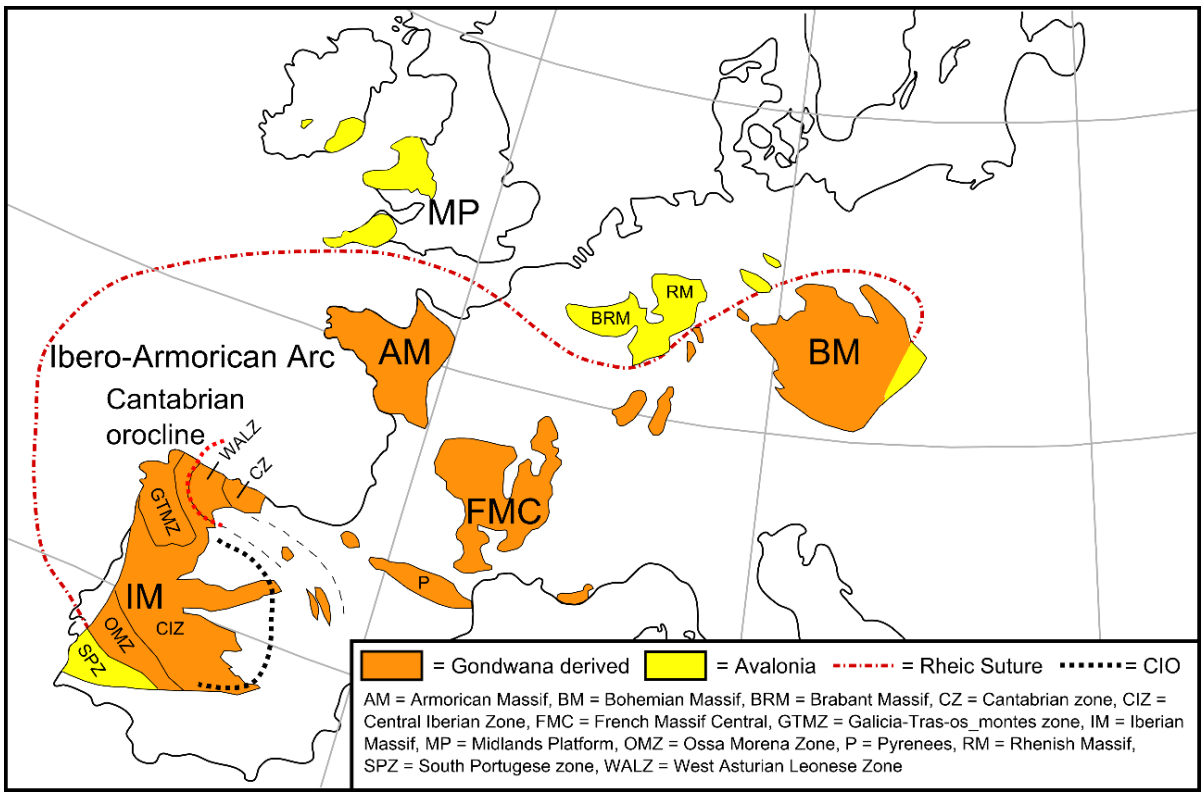

Figure 1. Overview map showing the major Variscan massifs of Europe. The map was redrawn as a simplified version from Nance et al. (2010).

Massif Central in France and the Ibero-Armorican arc in Western Europe (*figure 1;* Matte & Ribeiro 1975; Matte 1986; Matte 2001; Dias & Ribeiro 1995). The Ibero-Armorican arc links the Variscan belt in Brittany (France) with the Iberian Massif (Ballèvre et al. 2014). There is a smaller orocline situated in the core of the Ibero-Armorican orocline, which is called the Cantabrian orocline (CO) (Matte & Ribeiro 1975). The CO has been well studied, and it has been documented as a secondary orocline formed due to buckling of an originally linear mountain belt (Gutiérrez-Alonso et al. 2004; Pastor-Galán et al. 2011; Weil et al. 2001; Weil et al. 2010).

The CIO forms the southern continuation of the CO, with curvature of opposite direction. Contrary to the CO, the CIO has been less studied, and its geometry and kinematics are therefore not fully constrained. Three different geometries have been proposed for the CIO (*figure 2;* Aerden 2004; Martínez Catalán 2011b; Shaw et al. 2012). The geometries are based on the scarce amount of data that is available so far, and there is no consensus on the exact geometry of the CIO. Details concerning the three geometries will be described in the geological setting. Despite the differences in geometry, all three geometries have two common features: (1) the Morais Allochthonous complex is the core of the orocline; and, (2) the axial trace of the orocline is oriented WNW-ESE, which is sub-parallel to the fold axes of the last major Variscan deformation phase in Iberia (*figure 2*).

A possible way for classifying curved mountain belts is to make a distinction between kinematic classes (Weil & Sussman 2004; Weil et al. 2010; Yonkee & Weil 2010). A distinction is made between primary arcs, progressive arcs and secondary oroclines. This terminology can be confusing, since the term "arc" is also used for other geological features (i.e. volcanic arcs). A different classification was proposed by Johnston et al. (2013). This classification makes a distinction between primary curvature, a progressive orocline and a secondary orocline.

I will follow this classification, but instead of using the term primary curvature, a mountain belt with original curvature will be called a primary orocline. Following this terminology, all orogenic curvature can be described with the term "orocline", while the terms primary, progressive and secondary indicate the kinematic description of the orogenic curvature. A primary orocline is a mountain belt that was originally curved and experienced no subsequent rotation, a progressive orocline is a mountain belt that acquired curvature during its formation, or a belt with some primary curvature that was tightened during later deformation, and a secondary orocline is an originally linear mountain belts that has experienced rotation during subsequent orogeny (*figure 3;* Weil & Sussman 2004; Johnston et al. 2013).

In this study, a twofold strategy was developed to better constrain the geometry and the kinematics of the CIO. The first part consists of a paleomagnetic analysis, with the purpose of unravelling any vertical axis rotations around the prospective hinge. The second part consists of a detailed structural analysis of a section that is about 40 metres long. The results from this structural analysis will be incorporated in the larger-scale structure of the area surrounding Morais, and the relationship between the orientations of different generations of structures will be used to constrain the geometry of the orocline. The results

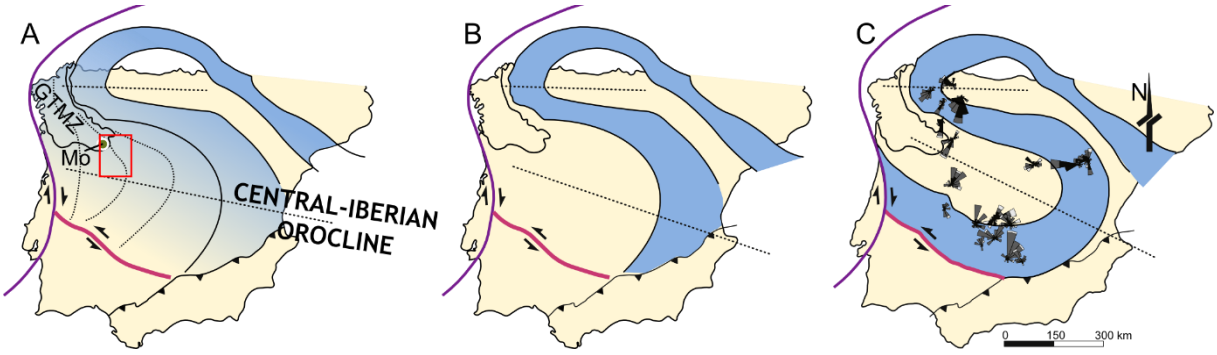

Figure 2. Previously published models for the geometry of the Central Iberian Arc. Mo indicates the position of the Morais complex. Geometries from: A) Aerden (2004)*; B)* Martínez Catalán (2011b)*; C)* Shaw et al. (2012).

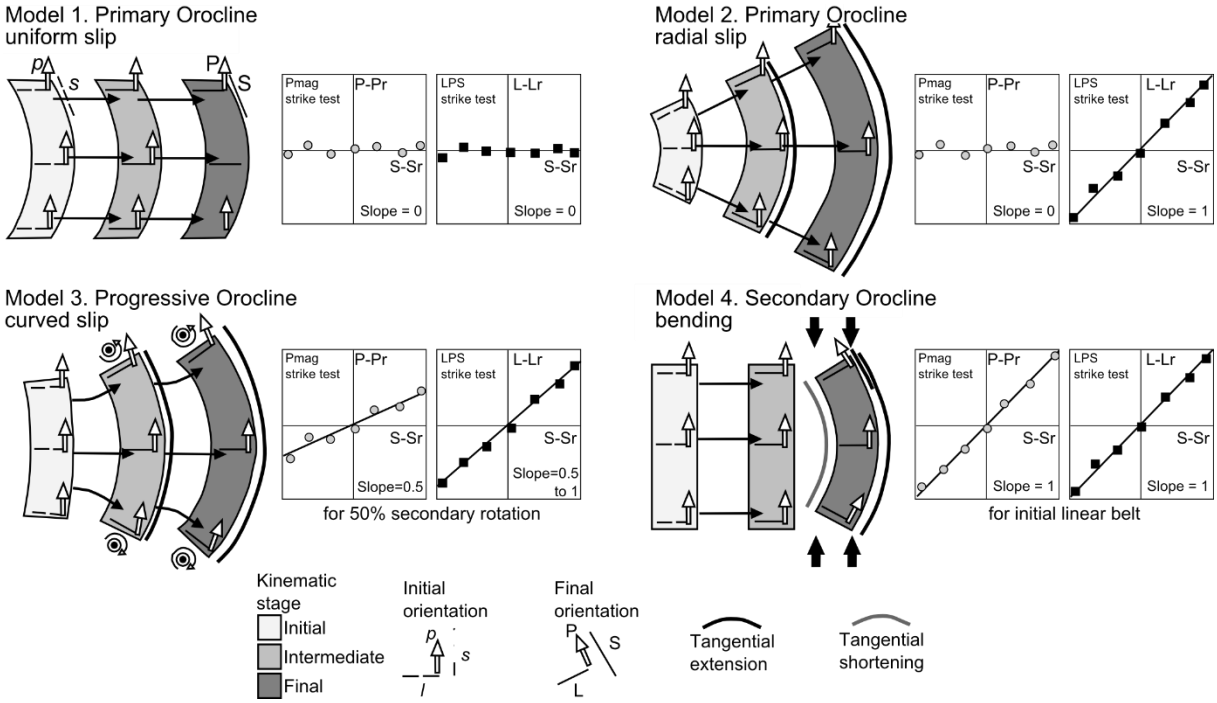

Figure 3. Classification scheme for curved mountain belts. Model 1 and 2 correspond to a primary orocline, model 3 corresponds to a progressive orocline and model 4 corresponds to oroclinal bending. Figure from Yonkee & Weil (2010).

will be compared with the geometries that have been proposed before, and implications for the geometry of the CIO will be discussed.

Geological setting

Continent-scale background

The Variscan belt is a Paleozoic orogenic belt which can be traced from the Ouachitas of North America in the west to the Caucasus in the east (Matte 2001). The Variscan belt is the result of the closure of the Rheic ocean and the collision between Laurussia and Gondwana (Matte 1986; Stampfli et al. 2002; Murphy et al. 2006; Nance et al. 2010; Martinez Catalan et al. 2014), which lead to the formation of part of Pangea. Opening of the Rheic ocean is associated with the drifting of the Avalonia micro-continent (Matte 2001; Murphy et al. 2006; Nance et al. 2010). Closure of the Rheic ocean occurred at ca. 370-330 Ma (Nance et al. 2010; Torsvik et al. 2012). The Variscan orogenic cycle was taking place between the Upper Devonian (360 Ma) and the Lower Permian (280 Ma) (Nance et al. 2010).

The Variscan belt in Europe can be traced from southern Iberia to north-eastern Bohemia (*figure 1*) (Dias & Ribeiro 1995; Matte 2001; Murphy et al. 2006; Martínez Catalán et al. 2007). The Iberian Massif forms the south-western limit of the European Variscan belt. It forms the largest section within the European Variscides, and it has escaped penetrative Alpine reworking (Quesada 1991). A complete through-orogen cross-section is preserved (Pérez-Estaún et al. 1991; Azor et al. 1994; Aerden 2004; Martinez Catalan et al. 2014).

Iberia

The Variscan belt in Iberia can be divided into several zones with distinctive tectono-sedimentary histories (Julivert et al. 1972). These zones are, from south to north: South Portuguese zone, Ossa-

Morena zone, Central Iberian zone, West Asturian-Leonese zone, and the Cantabrian zone. There is also the Galica-Tras-Os-Montes zone, which is positioned structurally on top of the Central Iberian zone.

The South Portuguese Zone is allochthonous to Gondwana, consisting of Laurussia derived units (Braid et al. 2011). The Ossa-Morena zone was originally a part of Gondwana (Rodríguez-Alonso et al. 2004), but is separated from the Central Iberian zone by a major ductile fault zone, the Coimbra-Córdoba Shear Zone (Azor et al. 1994). The zircon age populations and geochemical signatures are comparable for the Ossa-Morena zone and the Central Iberian zone in Neoproterozoic to Lower Cambrian sediments (Rodríguez-Alonso et al. 2004). Sedimentation is explained by Rodríguez-Alonso et al. (2004) as different basins on both sides of a magmatic arc, related to the Cadomian orogeny. Cessation of this Cadomian orogeny (ca. 700-500 Ma) was followed by opening of the Rheic ocean (Nance et al. 2010), with the South Portuguese zone drifting away from the Gondwana margin. The Ossa-Morena zone, the Central Iberian zone, the West Asturian-Leonese zone, and the Cantabrian zone were always part of Gondwana, with the Ossa-Morena zone forming the most distal zone (Pastor-Galán et al. 2013).

The GTMZ, which forms the hypothesized hinge of the CIA, consists of a nappe pile with units of different affinities. The nappe pile was formed due to Lower and Middle Devonian shortening. The nappe pile was thrust over the Paleozoic sedimentary sequence of the CIZ during the Upper Devonian-Lower Carboniferous (Martínez Catalán et al. 1997). The first age of deformation recorded in both the GTMZ and the CIZ is dated at 365 Ma, and deformation in the autochthon propagated towards the WALZ until 336 Ma (Dallmeyer et al. 1997). A distinction can be made between different units, based on their relative position in the nappe pile. These are the autochthonous basal unit (Martínez Catalán et al. 1997), the intermediate unit of oceanic affinity and the upper units which are allochthonous to Gondwana (Martínez Catalán et al. 1997).

The CIZ is the largest zone of the Iberian Massif, and it forms an internal zone of the orogen (Julivert et al. 1972; Diez Balda et al. 1995). The CIZ is defined by its stratigraphy, consisting of Upper Proterozoic and Lower Cambrian terrigenous sequences, and the transgressive character of the Lower Ordovician quartzite (Julivert et al. 1972; Diez Balda et al. 1995). Another characteristic of the CIZ is the occurrence of large amounts of pre-Variscan volcanic and plutonic rocks, mainly in its northern and eastern parts. These can be related to the Cadomian Orogeny and Lower Paleozoic extensional events (Diez Balda et al. 1995). There was also a phase of inversion, leading to unconformities of Late Proterozoic and Early Paleozoic age (Diez Balda et al. 1995).

A common feature in both the GTMZ and the CIZ is the occurrence of widespread syn-kinematic magmatism, and lesser amounts of post-kinematic magmatism. The syn-kinematic granitoids occur in regional metamorphic domes. The age of the syn-kinematic granites has been constrained at 325-318 Ma in the CIZ (Dias et al. 1998; López-Moro et al. 2014). Granites of a similar age have been found in the WALZ, close to the CIZ (Fernández-Suárez et al. 2000).

Three main deformation events have been described in the CIZ (Viruete et al. 1994; Viruete 1998; Diez Balda et al. 1995; Sá et al. 2011; Díez Fernández et al. 2013). The first phase, D_1, affected rocks at all structural levels. Differences in geometry of D_1 structures in the CIZ occur spatially, and two structural domains can be distinguished: the Domain of Recumbent Folds to the east and north, and the Domain of Upright Folds to the south (Diez Balda et al. 1990). Some major D_1 folds, like the Tamames Syncline, are striking NW-SE (Diez Balda et al. 1995). The second phase, D_2, formed some major angular folds with a penetrative sub-horizontal crenulation cleavage S_2. D_2 lead to the refolding of D_1 structures, while the S_1 foliation was overprinted by a penetrative S_2 foliation. Pre-Variscan granitoids were mylonitized during this phase. Variscan granites, which were emplaced during D_2, were heterogeneously deformed (Diez Balda et al. 1995). D_2 can be attributed to an extensional event, related to syn-collisional gravitational collapse induced by the thickening of the continental crust (Diez Balda et al. 1995). The third and last major phase, D_3, formed open vertical folds of large wavelength and small amplitude (Diez Balda et al. 1995). D_3 folds are striking roughly 100^0-120^0 (Viruete et al. 1994; Viruete 1998; Diez Balda

et al. 1995; Aerden 2004; Arango et al. 2013; Díez Fernández et al. 2013; Dias da Silva 2013). The orientation of D_3 folds changes towards the north to a more N-S oriented strike (Dallmeyer et al. 1997; Pamplona et al. 2006; Gómez Barreiro et al. 2007; Fernandez et al. 2011).

Regional setting: the study area

The study area is located to the south-east of the Morais complex (*figure 2*). The area comprises (meta)sedimentary rocks ranging in age from Neo-Proterozoic to Silurian (Diez Balda et al. 1995), and three generations of granitoids. The oldest generation of granites were emplaced during the Cadomian orogeny (Diez Balda et al. 1995) The second generation of granites are syn-kinematic, and were emplaced during the Variscan D_2 phase of Iberia (Diez Balda et al. 1995; Bea et al. 1999). They are situated in the Tormes Gneiss Dome, and are derived from the melting of Ediacaran rocks (Bea et al. 1999). These batholiths are composed of peraluminous K-rich S-type granodiorites and granites (Bea et al. 2003; López-Moro & López-Plaza 2004). Recent studies have dated the syn-kinematic granites of the Tormes Gneiss dome at 325-318 Ma (López-Moro et al. 2014).

A late-orogenic magmatic pulse also occurred, which post-dates the main orogenic events. The post-kinematic granites have been interpreted in the context of the formation of the Ibero-Armorican arc, as the result of the foundering of a thickened lithosphere (Gutiérrez-Alonso et al. 2011). There are multiple outcrops of post-kinematic granites in the study area, of which three plutons are directly relevant to this study. The Villavieja de Yeltes pluton and the Cipérez pluton were intruded into the Tormes Gneiss dome, and have been dated at 303.8 ± 2.3 Ma and 300 ± 2.9 Ma respectively (Gutiérrez-Alonso et al. 2011). The La Alberca granite, which is situated directly to the south of the Tamames syncline, has been dated at 308.7 ± 1.4 Ma (Gutiérrez-Alonso et al. 2011).

An important location for the paleomagnetic analysis is the Tamames Syncline (*figure 6*), a large D_1 structure that is trending NW-SE (Diez Balda et al. 1995). The Tamames Syncline preserves a succession ranging in age from the Upper Proterozoic to the Silurian (Diez Balda et al. 1995). Important for this study is the Tamames Limestone formation of Cambrian age (Corrales et al. 1974; Corrales & Valladares 1980; Valladares & Corrales 1980). This limestone formation is overlying the Tamames Sandstone Formation, with a gradual transition from sandstone to limestone (Valladares et al. 2000; Ugidos et al. 2003). The Lower Ordovician, the base of which is formed by the Armorican Quartzite, rests unconformably on the Tamames Limestone and other formations (Diez Balda et al. 1995).

The Tamames Limestone Formation is estimated to have a thickness which is ranging between 120 and 600 meters (Corrales et al. 1974; Valladares & Corrales 1980; Álvaro et al. 2003; Liñán et al. 2004), and is composed of alternating limestones and dolomitic carbonates (Liñán et al. 2004). It is characterised by two distinct sedimentary facies: the first facies is tidal flat deposits, and the second facies is that of a reef. This reef has been interpreted as a barrier, that allowed for the formation of the tidal flat deposits (Corrales & Valladares 1980; Valladares & Corrales 1980).

Detailed structural work around the Morais complex has revealed different generations of folds (*figure 4;* Dias da Silva 2009; Dias da Silva 2013). The direction of major D_3 folds is consistent throughout the area, with an axial trace that is oriented WNW-ESE. The orientation of D_1 folds is more variable. The D_1 folds are described at limited locations around the Morais complex. One of those locations is situated close to the outcrop that will be described in this study (*figure 5*). The map of *figure 5* draws D_1 folds of thick quartzitic layers, which are oriented WSW-ENE (Dias da Silva 2013). D_3 folds close to the outcrop of this study are oriented WNW-ESE.

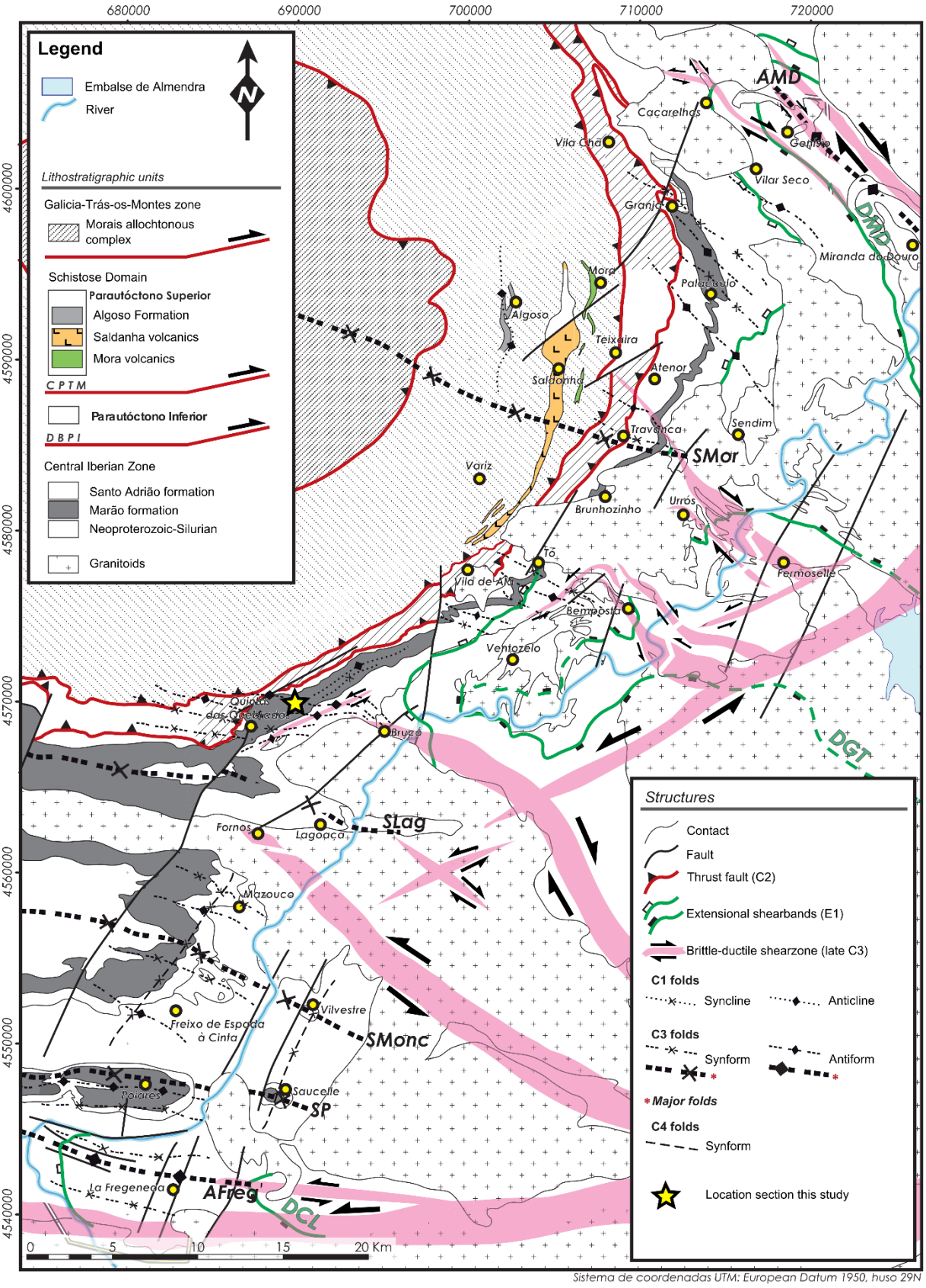

Figure 4. Structural map showing the major structures in the area surrounding the Morais Complex. Figure from Dias da Silva (2013).

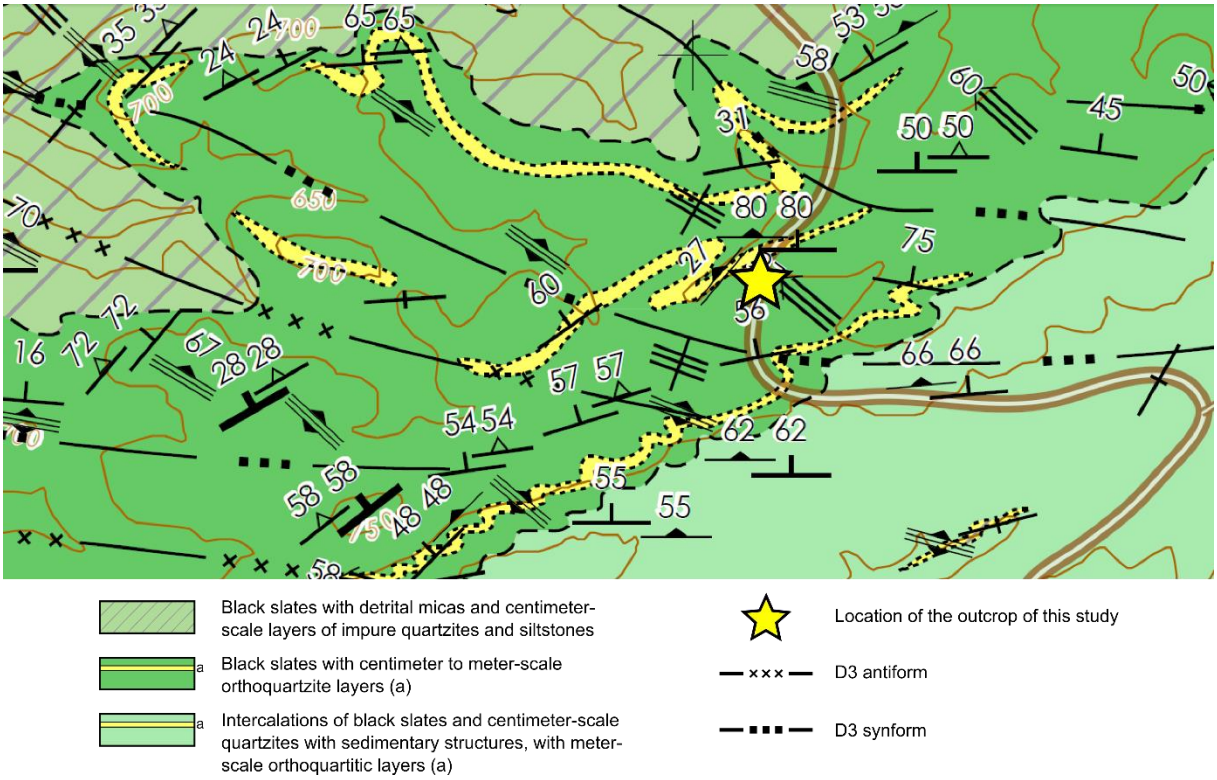

Figure 5. Detailed structural map of an area situated to the south-east of the Morais complex. The location of the outcrop that will be described in this document is indicated by the yellow star. Figure from Dias da Silva (2013).

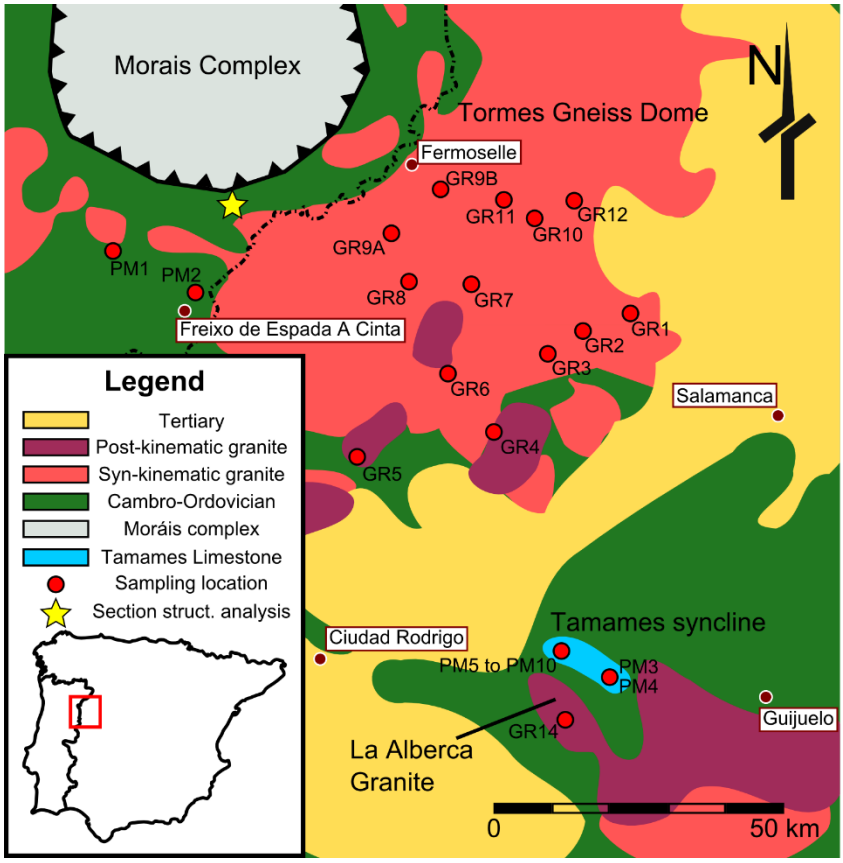

Figure 6. Detailed map of the studied area, with the locations that have been sampled for the paleomagnetic analysis and the the location of the outcrops of the structural analysis. The different colours indicated the different lithological units. Some of the major cities are showed, for a rough indication of the locations.

Existing geometries

Three different geometries have been proposed for the CIO, based on different data sets (*figure 2*). The first geometry (ordered on date of publication) is based on porphyroblast inclusion trails combined with data from previous structural studies (Aerden 2004). This geometry implies a differential rotation in which the distal part of the orocline rotates more than the core and the proximal areas. There is a gradational transition from "no orocline" in the west to an "orocline" in the east. The hinge of the orocline is trending NNW-SSE, with an axial trace that is parallel to most of the D_3 folds.

The second model (Martínez Catalán 2011a; Martínez Catalán 2011b; Martínez Catalán 2012) is based on a combination of data sets. The first data set consists of the axial traces of Variscan folds. The trace of D_1 contractional folds runs sub-parallel to the Ibero-Armorican arc in the north, and rotate to a N-S direction in the eastern limit of the CIZ. The D_2 extensional and later D_3 contractional folds are grouped together, and are mostly oriented NNW-SSE. It is suggested that D_3 folds are axial planar to the CIO. A second data set is based on the magnetic anomaly map by Ardizone et al. (1989). These magnetic lineations are correlated with the axial traces of the Variscan folds (Martínez Catalán 2012). Formation of the CIO was attributed to late-Variscan right-lateral transpression. Nucleation of the fold was attributed to the emplacement of the Galicia-Tras-os-Montes Zone (GTMZ), which is suggested to be in the core of the orocline.

The third model is based on paleocurrent directions (Shaw et al. 2012). The directions were measured in the Lower Ordovician Armorican Quartzite, which is part of the passive margin sequence of the northern margin of Gondwana (Sá et al. 2011). The paleoflow directions are consistent with the CO in northern Iberia. The paleoflow directions also delineate a second orocline to the south of the CO, drawing a curvature of 180^0 which is of opposite sign than the CO. The hinge of this orocline is drawn through the GTMZ, and is trending NNW-SSE. This S-shape geometry double orocline is interpreted as an original linear N-S trending belt formed by the passive margin of Gondwana, with the Rheic ocean located to the west (Shaw et al. 2012).

Methods

Paleomagnetism

A paleomagnetic analysis of rocks situated around the Morais complex was performed to delimit any rotation around the hypothesized hinge of the CIO. If the directions are changing systematically around the hypothesized hinge, this might indicate differential rotations and the possibility of an orocline (*figure 3*). If no rotations are observed, this means no rotations occurred after the magnetization was acquired. In this case, there are two possible explanations: (1) there have been no rotations in the area, or (2) rotations did happen, but those rotations occurred before the magnetic signal was acquired.

Samples for measuring the paleomagnetic directions were obtained from 24 locations (*figure 6; appendix A*). Sample sites were selected at different locations around the Morais Complex. The sampled rocks included limestones of the Tamames Syncline (8 sites), Ordovician sedimentary rocks to the south-west of the Morais Complex (2 sites), syn-kinematic granites of the Tormes Gneiss dome (11 sites), and post-kinematic granites from the Tormes Gneiss dome and the La Alberca granite which is situated to the south of the Tamames Syncline (3 sites).

Syn-kinematic granites were emplaced during orogenic collapse (D_2), and were strongly deformed during D_3 deformation (Viruete 1998). To avoid foliated samples, locations were selected that are at least one kilometre away from major D_3 shearzones. If any foliation was observed in the granite, no

samples were taken from that location. The post-kinematic granites were emplaced after the last deformation phase, and are thus undeformed (Yenes et al. 1999).

The sampling of two different generations of granites allows for some age constraints if rotations are found. If rotations are observed in the syn-kinematic granites, this rotation took place after the emplacement of the syn-kinematic granites. If rotations are observed in both the syn-kinematic and the post-kinematic granites, this rotation took place after the emplacement of the post-kinematic granites. If rotations are observed in the syn-kinematic granites, but not in the post-kinematic granites, this implies that rotations occurred in between the emplacement of the syn-kinematic and the post-kinematic granites.

Two different methods were used for collecting the samples: some sites were sampled by drilling and orienting cores in the field, and other sites were sampled by taking oriented handsamples. Sites PM8, PM9 and PM10 of the Tamames limestone were sampled by drilling in the field, the other sites were collected as handsamples because of technical difficulties. All the other sites were collected as handsamples. Drilling in the field is the preferred method of sampling, because samples can be taken with different orientations and from different layers if a bedding structure is present. Handsamples, on the other hand, only give specimens of the same orientation from a single layer. Cores were drilled from the handsamples using a static drill. All cores were cut into specimens of equal volume (around 10.5 cm^3).

A magnetomineralogical analysis was done using the Curie Balance method of Mullender et al. (1993). This analysis was performed to get insights on which minerals are carrying the remanent magnetization, which is needed for the interpretation of the magnetic directions. A small amount of rock was ground into powder, and subsequently heated and cooled to get information on how the magnetic signal changes with changing temperatures. A sinusoidally cycling magnetic field was applied at all times (Mullender et al. 1993). The strength of the magnetic signal is constantly measured, both during the heating and the cooling phases. Heating provides information on the magnetic carrier mineral, while cooling in between the heating steps can provide information on alterations of the magnetic minerals. Heating steps are 100 ^{0}C, after which it is cooled by 50 ^{0}C, up to a maximum temperature of 750 ^{0}C. If the heating and the cooling curve are different, the magnetic mineralogy is changed due to heating. If the heating and the cooling curves are similar, there has probably been no alteration. If alteration does occur, special care needs to be taken for the interpretation of paleomagnetic directions from thermally demagnetized specimens.

The samples were demagnetized using both the thermal (TH) and the alternating field (AF) methods. Demagnetizing the samples is needed to obtain their paleomagnetic directions. Thermal demagnetization was done manually by heating the specimens at increasing temperature steps. Each temperature step leads to the unblocking temperature at which some grains reach their unblocking temperature. If there is no applied magnetic field, these grains will get a new magnetization. Lowering the temperature again leads to exponentially increasing the relaxation time, until the magnetic moment is fixed. The contribution from these grains to the NRM is thus removed, and this process can be repeated up to the Curie temperature, at which the temperature of all magnetic grains is randomized and no NRM remains (Tauxe 2010). The magnetic signal after each step was measured on a 2G Enterprises DC-SQUID magnetometer.

Alternating field demagnetization uses a similar principle, but instead of increasing the temperature the samples were demagnetized by applying an alternating magnetic field which increases in strength at each step. All grain moments with coercivities below the applied field are realigned to the applied field, thus removing part of the NRM at each step (Tauxe 2010). AF demagnetization was done using a special designed machine, which can do both the demagnetizing and the measurements automatically. The measurements are done by a 2G Enterprises RF-SQUID magnetometer. Samples which were too strong

(i.e. outside of the measuring range of the cryogenic magnetometers) were measured using a JR3 spinner magnetometer.

Weak samples were measured twice in opposite positions. Measuring in two positions allows for better measurements, since this averages out any magnetic signal which is not part of the magnetism of the specimen. The first measuring position is with the orientation arrow pointing towards the cryogenic magnetometer, the second position is with the orientation arrow pointing away from the cryogenic magnetometer (*figure 7*).

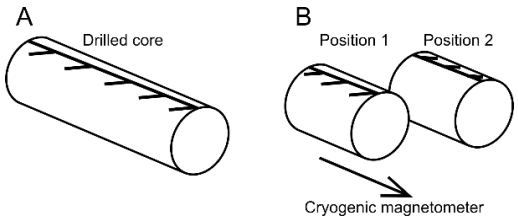

Figure 7. Sketch of the sample geometry. A) full core as drilled in the field, with orientation arrow pointing in the down-dip direction. B) The two measuring position, not the opposite directions of the orientation arrow.

The measured signal consists of a direction and an intensity, which is generally plotted with Zijderveld diagrams (Zijderveld 1967). Paleomagnetic directions were obtained from the demagnetization data by performing principal component analysis (Kirschvink 1980), using the Virtual Paleomagnetic Directions software by Ramón & Pueyo (2012). Specimens with a single magnetic carrier yielded a single magnetic direction. Some specimens could not be interpreted as a line, but did show a curved graph in the Zijderveld plots and a greatcircle in stereographic projections. If a specimen yields a greatcircle, the best fitting point of each greatcircle is obtained using the PalFit program, which analyses all available data per site, including both directions and greatcircles, to find the best fitting point on each greatcircle. This point will then be treated as the direction of that specimen. A 45 degree cut-off was applied on all directions per site, by using the Pal_45_s program. This excludes any points outside of the secular variation range, while the program also calculates the mean direction of the points that are within the secular variation range.

There are some requirements for the obtained directions to be valid. During the Carboniferous and early Permian, Iberia was located at an equatorial position. The sampled granites, which are of this age, are therefore expected to have shallow inclinations. If steeper inclinations are found, it is likely that later processes either reworked the rock or caused a remagnetization of the magnetic signal. Sites not showing the expected shallow inclination will be discussed.

The inclination requirement for sedimentary rocks is different. Their magnetization could have been obtained at different times. If the magnetization is primary, the inclination should correspond to the latitude of deposition. Gondwana was moving from the South Pole in the Cambrian to equatorial latitudes in the late Carboniferous and Permian and afterwards it continued moving north to its present latitude (Torsvik & Renhström 2001; Torsvik et al. 2012). Some authors place Iberia at lower latitudes during the Cambrian (less than 60^0), where the formation of the limestones took place (Pereira et al. 2012). Any inclination between 60^0S and the present latitude are therefore possible, and will be discussed.

A fold test was performed for samples from the Tamames syncline, following the method of Tauxe & Watson (1994). This fold test was used to determine whether the magnetization was obtained before or after folding. The method applies a progressive unfolding of the bedding planes and the paleomagnetic directions corresponding to these bedding planes, to find out at which amount of unfolding has the best clustering of the magnetic vectors. If the best clustering is at 100% unfolding, the magnetic signal is pre-folding. If the best clustering is at 0% unfolding, the paleomagnetic signal is post-folding. If the best clustering of the magnetic vectors is between 0% and 100% unfolding, the magnetization is syn-folding. If the magnetization is pre-folding, it could be the primary direction or the direction obtained during any remagnetization event which pre-dates the folding. The magnetic signal is primary if it represents the magnetic direction obtained during the formation of the rock.

Structural analysis

The studied outcrop consists of quartzitic and pelitic strata of Ordovician age (Sá et al. 2011; Dias da Silva 2013). The section is located to the SW of the Morais complex, in the North-Eastern part of Portugal (GPS coordinates: 41.25212 N, 6.73172 W). It is a road section along the N221, between Mogadouro in the north and Freixo de Espada A Cinta in the south (*figure 4; figure 5; figure 6*). The section is about 40 meters long, with outcrops on both sides of the road.

The main purpose of the structural analysis was to obtain the orientation of the structures that formed during different deformation phases, and to incorporate them in the regional structure. The relationship between different generations of structures could have implications for the geometry and the kinematics of the CIO. If the orocline is formed by buckling, orthogonal directions are expected in the hinge of the orocline, between structures of the first orogenic phase and structures of the orocline phase (*figure 8*). Orthogonal directions could also be explained by a change in the stress field. Non-orthogonal directions could have multiple explanations, including a primary or progressive orocline, no orocline or two tectonic events with oblique shortening directions. Parallel directions could indicate a primary orocline formed during an early orogenic phase, or no orocline but just separate tectonic events with the same shortening-direction.

The structural analysis consisted of the description of different structures, the analysis of thin sections to obtain the temporal and geometrical relationships between different structures, and of retrodeforming different structures to obtain their original orientations. Over 350 measurements were collected in the field, and 19 oriented handsamples were collected for the creation of thin-sections and petrographic analysis. Plane orientations will be noted as dip azimuth/dip, lineations will be noted as trend/plunge. The field measurements included measurements of bedding (151), tectonic foliations (80), intersection lineations (69), and fold axes (66). Structural data was processed using Richard Allmendingers stereonet software (Cardozo & Allmendinger 2013). Different deformation phases were observed, which will be described as D_x for the oldest phase, D_{x+1} for the second oldest phase, and so on. The interpretation and correlation with regional structures will follow in the discussion.

The first step of the structural analysis was the description of the structures observed at the outcrop-scale. A good understanding of the structures is needed at later steps, for obtaining the directions of the different deformation phases. This section aims to describe all structures, and if possible the temporal relationship between the different structures. The temporal relationships can be deduced from fold interference patterns and from the folding of lineations and foliations. Any observed structure will be described, which can include bedding planes, foliation planes, different types of folds and different types of lineations.

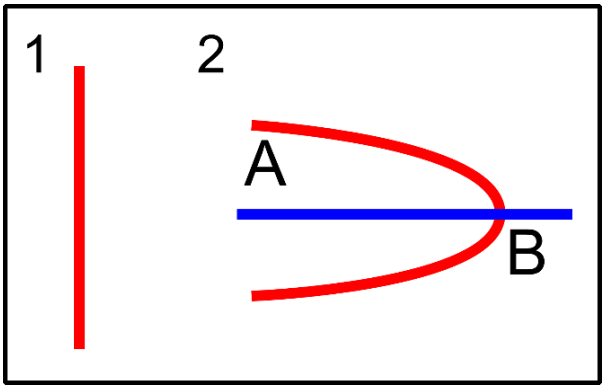

Figure 8. Illustration of the relationship between different deformation phases for a secondary orocline. 1) The initial straight mountain belt. 2) The initinial mountain belt (red) has been folded around a vertical axis by a stress field that also formed structures axial planar to this orocline (blue). At A), in the flank, structures from both phases are parallel, while at B), the phases have perpendicular directions.

The second step of the structural analysis was the analysis of thin-sections, which were created from handsamples that were collected at key locations in the outcrop. Thin-section analysis was used to study the mineralogy and for estimating the metamorphic grade, which was done by analysing the metamorphic mineral assemblages. A careful distinction had to be made between metamorphic minerals and detrital minerals, the latter of which are not part of the metamorphic assemblage. Detrital grains can be recognized by more rounded shapes and no crystallographic preferred orientation, while metamorphic minerals often have a preferred direction in which they grow.

The next part of analysing the thin-sections consisted of analysing the structures that are visible in thin-section. Studying the structures in thin-section can provide information on different phases of deformation, and the temporal relationship between these phases. The tectonic foliations were classified following the method of Passchier & Trouw (2005). This classification includes the geometry of the foliation, the minerals defining the foliation, and the temporal relationship between different foliations. The angles of the foliations were measured relative to a lab arrow. Since the orientation of the thin sections is known, the true orientations of these lines can be calculated. This results in the true orientation of the measured line, which is the intersection of the foliation plane with the plane of the thin section. The foliation planes were restored by finding the plane containing both the measured direction and the intersection lineation.

The last step of the structural analysis is to retrodeform the outcrop to obtain the strain pattern of older deformation phases. Retrodeforming the outcrop was done by sequentially undoing the effect of deformation phases, starting with the youngest phase. The structure I used for unfolding is the oldest generation of mullions, which is representative of the fold axis of the oldest deformation phase.

Results

Paleomagnetism

Rock magnetism

Syn-kinematic granites

The results of the Curie balance for the syn-kinematic granites (*Appendix B*) show a large decay at the lower heating steps, while the decay becomes smaller at higher temperature steps. There are no clear steps in the demagnetization curve, the change from rapid to slow decay is gradual. This result of the Curie balance method is indicative for titano-magnetite. The cooling curve is following the heating curve, so no alteration of the magnetic minerals occurred. The strength of the magnetic signal was varying between different sites, sometimes even between different specimens. All intensities were within the same range, only site GR1 had a much higher intensity than the other sites.

Post-kinematic granites

This generation of magmatic rocks (GR4, 5 and 14) includes granitoids and lesser amounts of mafic rocks. Although differences in isotopes are present between these granitoids and the syn-kinematic ones, their magnetic behaviour is similar since both are the result of crustal melting. The Curie Balance (*Appendix B*) shows results that are similar to those of the syn-kinematic granite. There is rapid decay at lower temperatures which gradually changes to no decay at higher temperatures, which is indicative of titona-magnetite. The cooling curves show that no alterations of the magnetic minerals took place. The post-kinematic granites have a clear magnetic signal, although it is not very strong.

Ordovician sediments

Two sites of these sediments (PM1 and PM2) were sampled, both having different lithologies. The first site, PM1, is part of the Armorican Quartzite. Secondary precipitation of new minerals occurred, giving it a really dark colour. The Curie Balance (*Appendix B*) shows that little decay occurs at lower temperatures. The decay in strength per temperature step keeps increasing, until the decay stops at 580 ^{0}C. This is diagnostic for magnetite. The cooling curve shows that no major alterations occurred. This rock is extremely magnetic, the magnetic signal is strong enough to make magnets stick to a flat surface of the handsample (*figure 9*).

The second site, PM2, is formed by a siltstone. The Curie Balance diagram shows rapid decay at low temperature steps, which stabilizes at higher temperatures, which indicates that titona-magnetite is the

magnetic carrier. The heating and the cooling curve are similar, so no alterations occurred. The magnetic signal is measurable, although it is not strong.

Tamames limestone

The Curie Balance diagrams (*Appendix B*) indicate a rapid decay at the lowest temperatures, which stabilizes towards higher temperatures. There appears to be no alteration in the magnetic behaviour, with the exception of PM3. During heating and cooling, new minerals are formed around 250 ^{0}C and also around 330 ^{0}C. This means any magnetic vector obtained above 250 ^{0}C is probably not valid for this site. Demagnetization of specimens from site PM3 was attempted, but no magnetic vector was obtained because of the alteration, and the site was left out of further analysis. The rest of the Tamames limestone samples have a magnetic signal of sufficient strength.

During thermal demagnetization of the samples, the mineral carrying the natural remanent magnetization (NRM) proved to be a different mineral. There is very little decay up to 250 ^{0}C, after which it increases rapidly and the samples were magnetically empty at 330 ^{0}C (*figure 10*). This Curie temperature is similar to the Curie temperature of 325 ^{0}C described for the mineral pyrrhotite by Dekkers (1989). Pyrrhotite is a solid solution series of Fe-S compounds, with composition $Fe_{1-x}S$, where x can vary between 0 and 0,13 (Dekkers 1988; Dekkers 1989). The formation of pyrrhotite in metacarbonates depends on the amount and composition of metamorphic fluids. Very low amounts of H_2S fluids will favour the in situ growth of pyrrhotite crystals at the expense of iron-bearing minerals in its surroundings (Wehland et al. 2005). The magnetic behaviour of pyrrhotite depends on grain-size. The pyrrhotite in the Tamames limestone is probably very fine-grained, close to single domain, as evidenced by its resistance against alternating field demagnetization (*figure 10*, Rochette et al. 1990). It is not uncommon for magnetic sulphides to not become apparent using mineralogical techniques (Rochette et al. 1990), although the reason for this behaviour is still uncertain (Dekkers, personal communication).

Demagnetization data

Demagnetization of the specimens resulted in the principal components, which were analysed to obtain paleomagnetic directions. The syn-kinematic granites yielded results of varying quality (*appendix C*). The appendix shows an example of a "good" result and a "bad" result for each site. Some sites yielded a really clear direction (e.g. GR1 and GR9), all other syn-kinematic granite sites were interpreted through a combination of directions and greatcircles (*appendix D; appendix E*). Some specimens yielded no clear results, like the "bad" result from site GR12 (*appendix C*), so it was not possible to get either a greatcircle or a direction from those. The best fitting point on each greatcircle was calculated for each separate site, to get the best fitting direction from the greatcircles (*appendix E*).

The post-kinematic granites show a similar behaviour as the syn-kinematic granites, with some specimens which were interpreted as directions and some as greatcircles (*appendix C*). The relative amount of specimens that were interpreted as greatcircles is higher compared to the syn-kinematic

Figure 9. Picture illustrating the strong magnetic signal of rocks from site PM1.

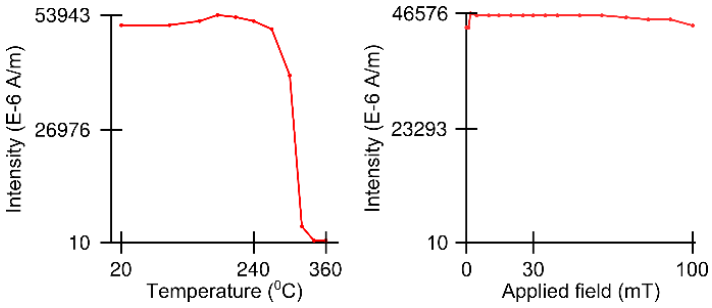

Figure 10. Demagnetization plots from the Tamames limestone. The left plot represents thermal demagnetization, with rapid decay between 270 C^0 and 330 C^0. The right plot represents alternating field demagnetization, and there is little to no decay.

granites (*appendix D; Appendix E*). Some specimens did not have a signal that was interpretable, so these were left out from further analysis. The best-fitting direction on each greatcircle was calculated (*appendix E*).

The Ordovician sediments have different magnetic behaviour. The demagnetization data from PM1 were more often interpreted as directions, while greatcircles were only needed for some specimens (*appendix C, appendix D*). Most of the interpreted greatcircles were plotting close to the directions, which indicates that at least one component of the greatcircle is the direction. This is different for site PM2, which shows a variety of greatcircles at different orientations. Four results could be interpreted as directions for this site, which is important for calculating the best fitting points on the greatcircles (*appendix E*).

The Tamames Limestones yielded good results, where the magnetic signal could be interpreted as a direction. These directions are interpreted from straight lines that go to the origin (*appendix C*). Most sites were interpreted with directions only, but site PM6 and PM8 required greatcircles for the interpretation of some specimens (*appendix D, appendix E*). Site PM8 required just one greatcircle, which has a good fit with the other directions. Site PM6 was interpreted using more greatcircles, but these also show a good fit with the directions.

Directions

The Palfit program calculated a direction for each specimen, and these directions were used to calculate the average direction per site, averaging the effects of secular variation but discarding any points that are outside of the secular variation range (*appendix F*). The resulting directions (*figure 11, table 1*) show a range of directions, with different directions for different lithologies. The syn-kinematic granites (*figure 11a*) show a range of directions, ranging from WNW to SSE, which might represent two separate

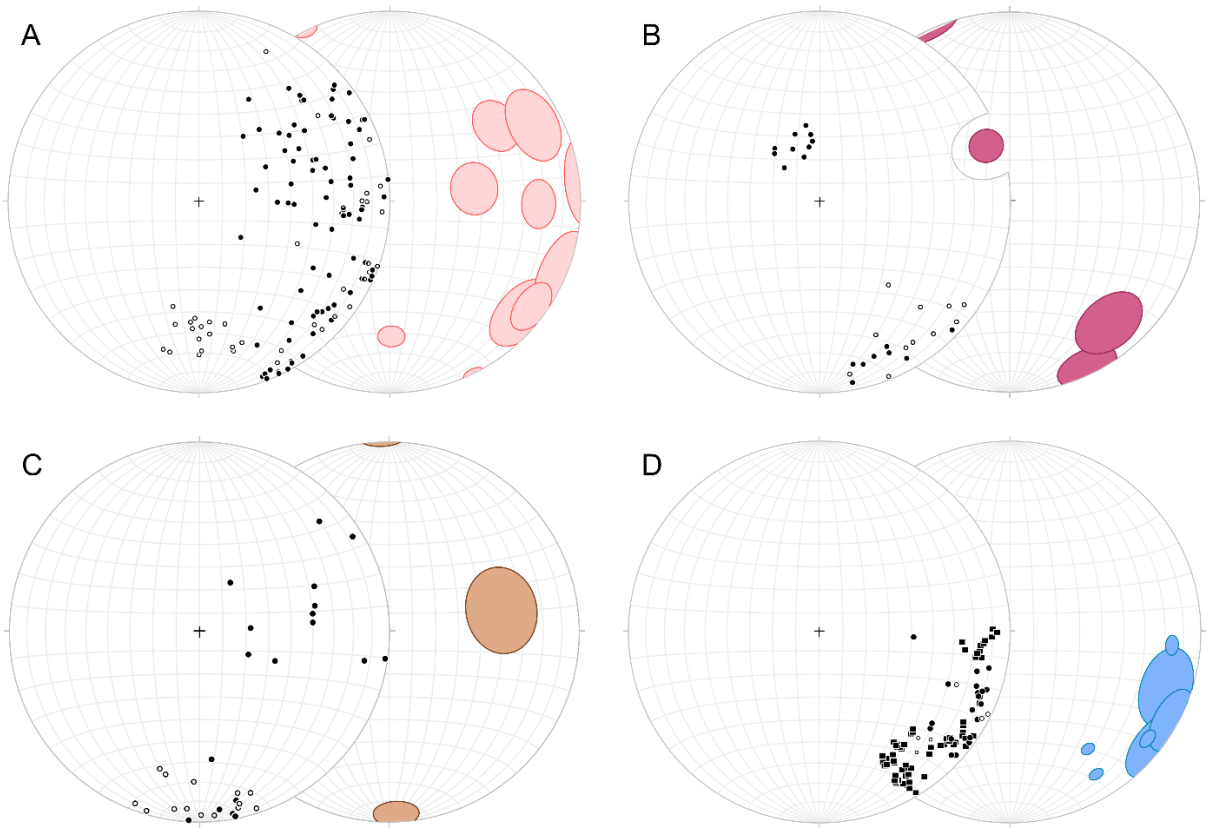

Figure 11. Equal area projections showing the results of the paleomagnetic analysis. The left plot shows all individual data points, the directions per specimen, while the right plot shows the small-circles that represent the site mean and the a95 confidence interval. A) Syn-kinematic granites. B) Post-kinematic granites. C) Ordovician sediments. D) Tamames limestones.

	n	Declination	Inclination	k	a95
Syn-kinematic granites					
GR1	13	154.1	-0.5	160.5	3.3
GR2	20	054.3	31.9	11.2	10.2
GR3	11	130.3	10.3	13.8	12.8
GR6	17	179.3	-30.3	52.9	5.0
GR7	10	112.9	1.4	13.0	13.9
GR8	13	126.4	8.2	23.3	8.8
GR9	12	090.8	22.8	26.1	8.7
GR9B	11	061.8	15.1	13.3	13.0
GR10	8	081.0	52.9	28.1	10.6
GR11	9	084.1	-4.4	16.6	13.0
GR12	-	-	-	-	-
Post-kinematic granites					
GR4	10	337.4	63.8	102.8	7.2
GR5	12	154.8	4.2	20.2	9.9
GR14	7	140.6	-18.1	21.9	13.2
Ordovician sediments					
PM1	20	177.8	-4.6	21.4	7.2
PM2	12	079.1	39.1	7.6	16.8
Tamames Limestone					
PM3	-	-	-	-	-
PM4	22	148.8	13.9	146.0	2.6
PM5	16	146.3	27.2	198.0	2.6
PM6	12	094.7	15.9	168.0	3.4
PM7	16	127.8	9.6	128.2	3.3
PM8	9	128.1	3.4	19.6	11.9
PM9	9	109.6	13.6	15.1	13.7
PM10	8	118.7	3.3	28.7	10.5

Table 1. Mean paleomagnetic direction per site, with statistical parameters. No results are present for sites GR12 and PM3, since the data quality was too poor for these sites to obtain at least seven directions.

groups. Most of the sites show the expected shallow inclination, although some sites like GR2 (054/32), GR6 (179/-30), and GR10 (081/53) show a

steeper inclination. There is some overlap between the directions from most sites, but sites GR1 (154/-1) and GR6 (179/-30) show no overlap with other syn-kinematic sites. Site GR12 is not included in the results, since the data quality was not good enough to obtain seven directions for this site.

The post-kinematic granites show a different direction (*figure 11b*, *table 1*). Sites GR5 and GR14 show a direction that is oriented more towards the SE, and the a95 confidence interval is overlapping for these sites. Sites GR5 and GR14 show the expected shallow inclination. Site GR4 (337/64) shows a direction pointing towards the north, with a steep inclination, and is different than the other post-kinematic granite sites.

The Ordovician sediment sites show different directions (*figure 11c*, *table 1*). PM1 has a direction pointing to the south (178/-5), with the expected shallow inclination. The data points for site PM1 show a good cluster, with some variation but generally pointing towards the same direction. The data points for site PM2 are less clustered, with a large variation in directions. The mean direction (079/39) is steeper than the expected shallow inclination.

The Tamames limestones yield a range of direction, all of them showing the expected shallow inclinations (*figure 11d, table 1*). The limestones show a range of direction, ranging from E to SE. Most of the sites have an overlapping a95 confidence interval, except for sites PM4 and PM5. However, the direction from these sites are still close to the directions from the other sites. There is also a good overlap in data points between sites that were drilled in the field and sites were handsamples were collected. This indicates that both sampling methods yielded viable results. The only difference is that the sites with handsamples show a much better clustering, since all the cores were drilled in the same orientation from a single layer.

The Tamames Limestone sites were sampled from different locations along the outcrop, from different layers. I investigated if there is a spatial pattern in the change in directions (*figure 12*), but there appears to be no direct relationship between the directions and either the site location or its stratigraphic height.

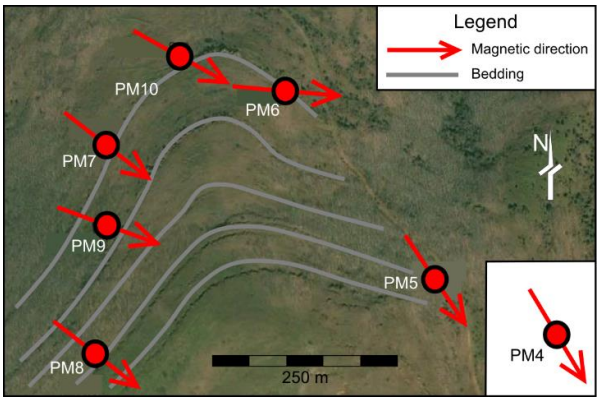

Figure 12. Map of the Tamames limestone outcrop, showing the bedding trace and the paleomagnetic directions. Photograph from Google Earth.

Figure 12 shows an orthophotograph showing the bedding attitude of the syncline. A fold-test was applied, which gave a negative result with the best clustering at -25% unfolding (*figure 13*). The negative fold-test implies that the magnetic directions were obtained after folding. Furthermore, the result shows that the best clustering is at -25% unfolding, which means that the clustering of data points is worse after unfolding.

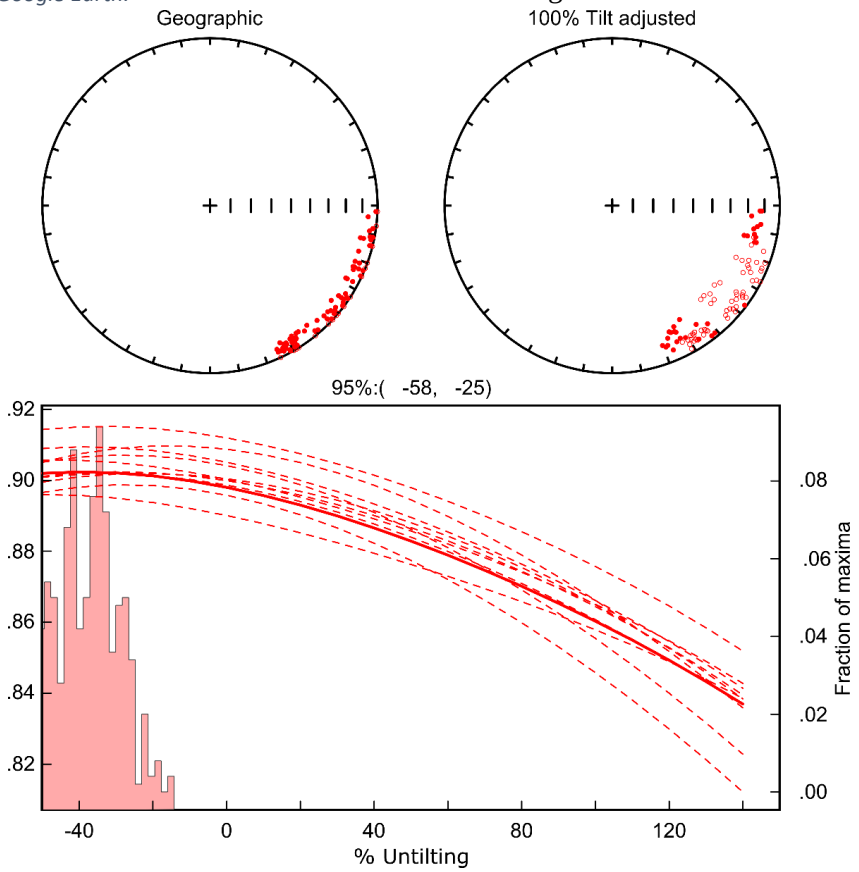

Figure 13. Results of the fold-test for the Tamames limestones. The upper left stereonet shows an equal-area projection of the measured directions, the upper right stereonet shows an equal-area projection of the unfolded directions. The lower graph shows the unfolding, which shows that the best clustering of the directions occurs at -25% unfolding.

Structural analysis

Outcrop-scale structures

The studied outcrop consists of quartzitic and pelitic layers of varying thickness. The most consistent structure in the section is a penetrative cleavage, that is developed in all the pelitic layers (*figure 14A,B; figure 15 A,C*). The orientation of this cleavage is varying in orientation through the section, both in dip and dip azimuth (*figure 16B*). However, all the cleavage planes are crossing through one place in the stereographic projection, so the variation in the cleavage orientation can be explained by just one folding event. The competent quartzitic layers are influencing the cleavage orientation, which changes from

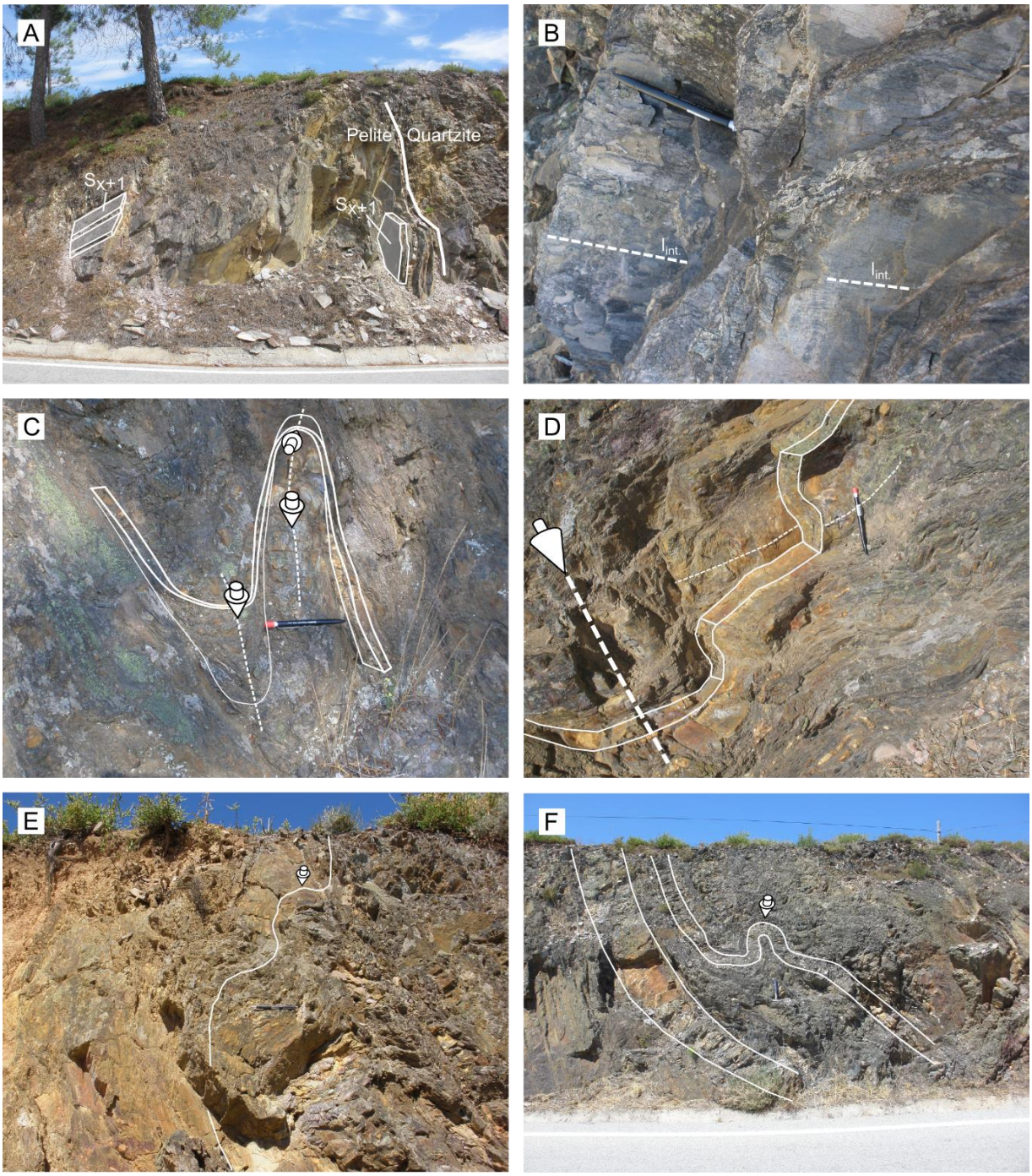

Figure 14. Field pictures with tracings to illustrate the different structures in the section. A) Penetrative foliation steepening against quartzitic layer. B) Top view of penetrative foliation, with lines indicating the intersection-lineation. C and D) Fold interference pattern of horizontal and vertical fold axes. E and F) Folds in quartzitic layers with steep fold axes.

shallower dip angles in the pelitic domains to steeper dip angles closer to the quartzitic domains (*figure 14A*). Despite the influence of the quartzitic layers, the cleavage is not perfectly parallel to the bedding plane (*figure 15A*).

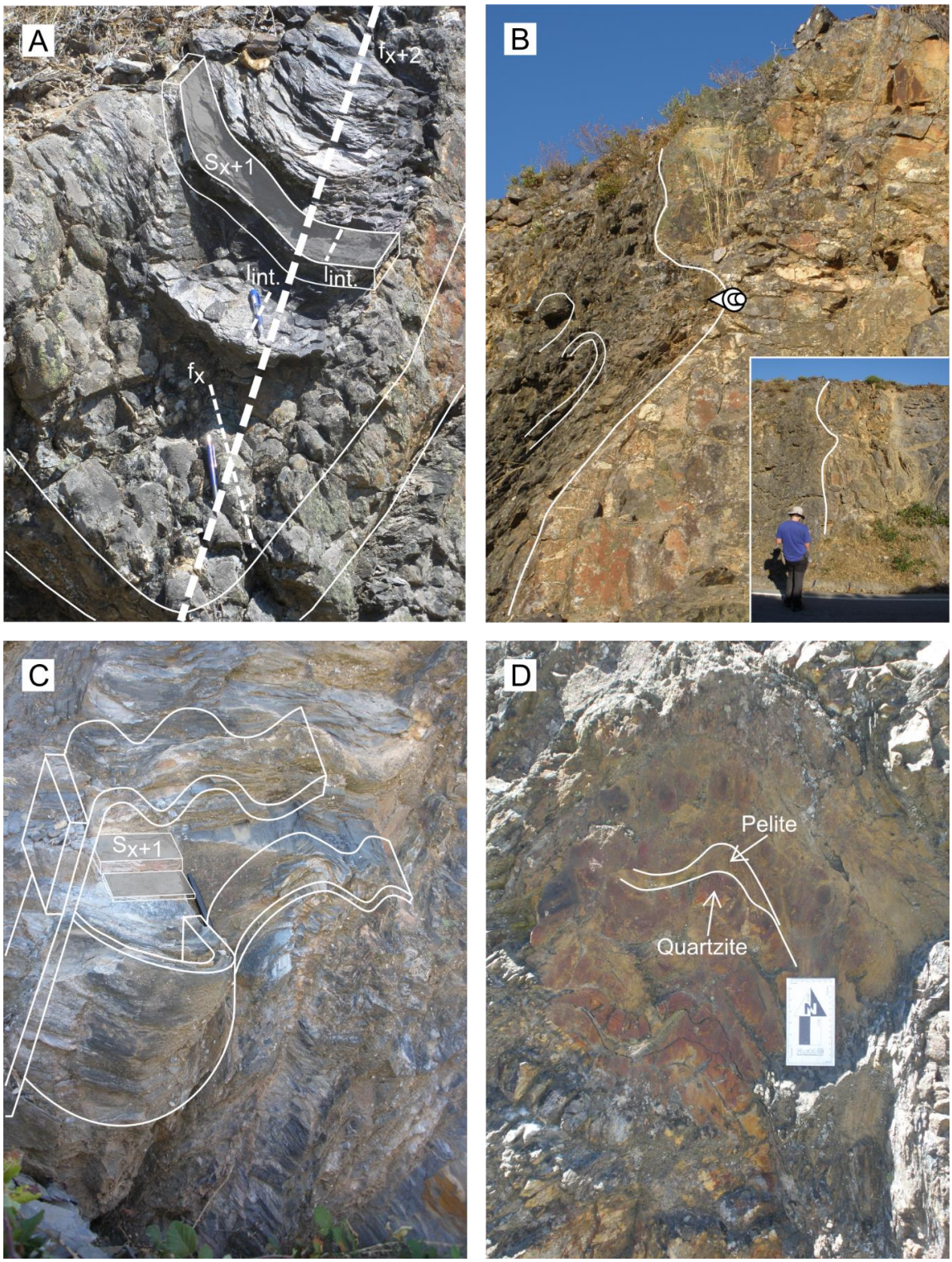

Figure 15. Field pictures with tracings to illustrate the different structures in the section. A) folded quartzitic layer with foliated pelitic layer in the core of the fold. Mullions are present on the quartzite-pelite interface. B) Quartzitic layer that appears to be thinned in front-view (small inset), but that is actually folded with a sub-horizontal fold axis. C) Complex fold interference pattern in pelitic domain. D) Competence contrast between the quartzite and the pelite, the latter of which is thinned in the flanks of the fold.

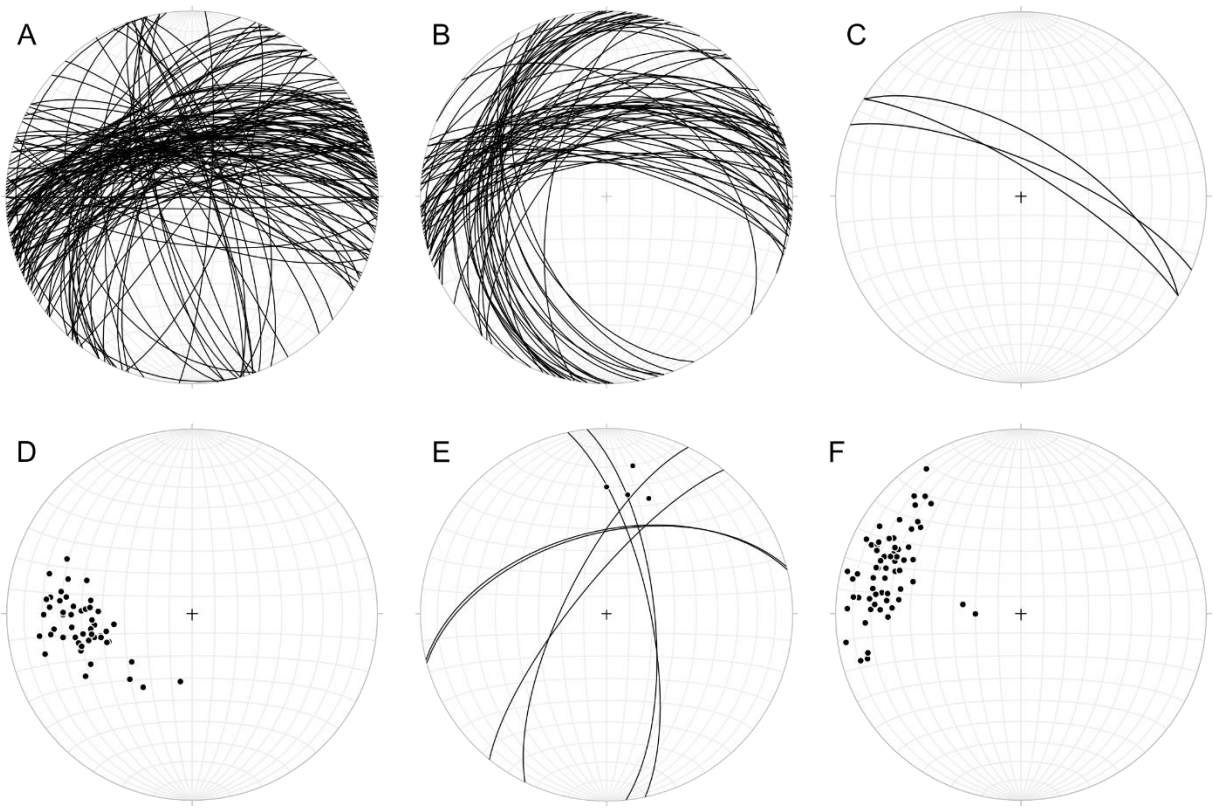

Figure 16. Equal area projections showing the orientations of different structures that were measured in the field. A) bedding. B) S_2. C) S_3. D) f_1. E) the dots represent the measured fold axis f_2, the planes represent the bedding planes around the mullion, which cross through the fold axis. F) Intersection lineation.

The oldest deformation phase, hereby called D_x, is represented by mullions on the quartzitic beds (*figure 15A*, *figure 17*, *appendix G*). Mullions are cylindrical fold structures with rounded lobes convex into the least competent layer and cusps pointing towards the more competent layer (Sokoutis 1987). Mullions form by deformation under a compressional stress regime with layer-parallel shortening, as a result of the competence contrast between different layers (Sokoutis 1987; Kenis et al. 2004; Kenis et al. 2005). The mullions form an anastomosing pattern, although the continuity along the long axis is inhibited by mullions of a later phase. The mean direction of these mullion axes is 264/39. More data on the mullions can be found in appendix G.

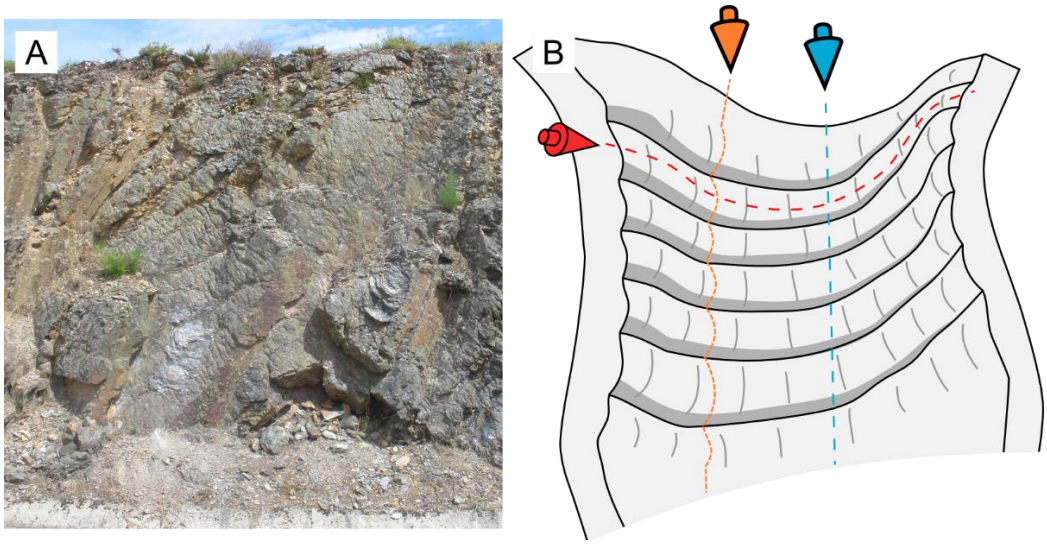

Figure 17. A) field picture of folded quartzite beds which were affected by different deformation phases. B) Interpretation of the field picture.

The D_x mullions are folded by a second generations of mullions, D_{x+1} (*figure 17*). These D_{x+1} mullions are spaced further apart than the D_x mullions, with the distance between separate mullions ranging from 17 to 39 centimetres with an average of 26 centimetres. The mean fold axis the D_{x+1} mullions is 010/30, although the intersection from bedding planes around these mullions gives a slightly steeper fold axis (*figure 16E*). The penetrative foliation can be coeval with the D_{x+1} mullions, since both have one event pre-dating the structures and one event post-dating the structures. I therefore call the penetrative foliation S_{x+1}. Folds with shallow fold axes are not restricted to mullions only, but are present throughout the section (*figure 14C,D; figure 15B,C*).

Both D_x and D_{x+1} structures have been refolded by a later event D_{x+2}. This event formed open folds with a steep fold axis (*figure 14C,D,E,F; figure 15A,C; figure 17*). The mean fold axis f_{x+2} is 293/35, which is the axis calculated from the intersection of the S_{x+1} cleavage (*figure 16*). These folds are observed mainly in the quartzitic layers, but they might have been formed as well in the pelitic layers. Some pelitic layers in the core of D_{x+2} folds have a foliation that is axial planar to these folds, but this foliation is not as well developed as the penetrative S_{x+1} foliation. The thin-section analysis will provide more information on the different foliations.

Another important set of structures is formed by a lineation that is visible on the S_{x+1} planes (*figure 14B; figure 15A*). The orientations of this lineation forms an elongated cluster, with a mean direction of 289/23 (*figure 16*). The origin of this lineation could not be determined from field observations, although it is clear that the lineation is an intersection lineation, rather than any other type of lineation.

The influence of three different deformation events resulted in complex fold interference patterns at many locations in the section, in which the influence of separate events is hard to distinguish. Fold interference patterns were formed in both the quartzitic layers and the pelitic layers (*figure 14C,D; figure 15C; figure 17*). *Figure 17* shows f_x mullions that are refolded by f_{x+1} mullions, and both are folded by D_{x+2} folds. Fold interference patterns in multilayer domains are more complicated, since the pelitic layers are less competent and thus easier to deform. The fold interference patterns are often a combination of folds with a steep axis and folds with a shallow axis.

There are differences in the structures between the quartzitic and the pelitic layers. The quartzitic layers are more competent, and thus harder to deform. This results in relatively simple folds in the quartzite layers, but the pelitic layers often contain complicated structures. The wavelength of folding is often smaller in the pelitic layers, or it has more complex geometries (*figure 14E,F; figure 15B*). In multilayer domains, the pelitic layers are often thickened in the hinge zones (*figure 15D*).

Since the three different deformations were observed at different locations in the outcrop, I will hereby assign a more specific name to each phase. The oldest phase, with the first generation of mullions, is D_1. The second phase, which is responsible for the folds with sub-horizontal axes and the sub-horizontal penetrative foliation is D_2. The last phase, which produced open folds in all older structures, is D_3.

Thin section analysis

Mineralogy

The studied outcrop is uniform in its mineralogical composition, although variations in the relative abundance of different minerals occur in different parts of the outcrop. All thin sections contain quartz, muscovite and oxides in different ratios (*Appendix H*). The quartzitic domains contain lesser amounts of muscovite and oxides, that do not form more than ten percent of the total composition. The pelitic domains have a variable composition, containing quartz, muscovite and oxides in varying relative amounts. Most of the thin sections have some accessory tourmaline crystals, which are more common in the (*figure 17*). Staurolite is present in the thin-sections, where it is more common in the quartzitic domains (*figure 18*). Different types of oxides occur, but they were treated as “oxides” because a more

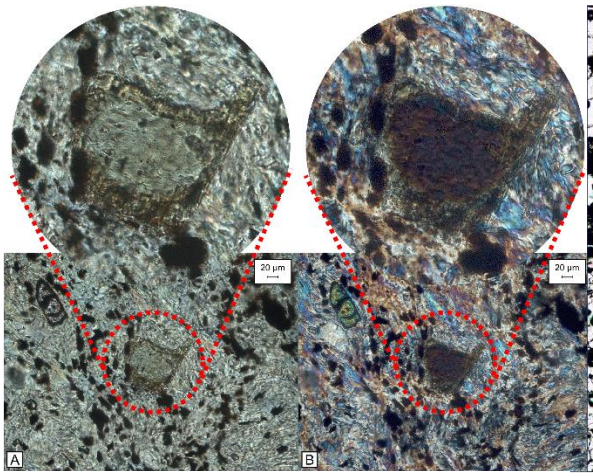

Figure 17. Thin-section pictures of tourmaline crystals, plane-polarized light on the left and cross-polarized on the right. The tourmaline crystals has a core with high birefringence, with colourless metamorphic overgrowths.

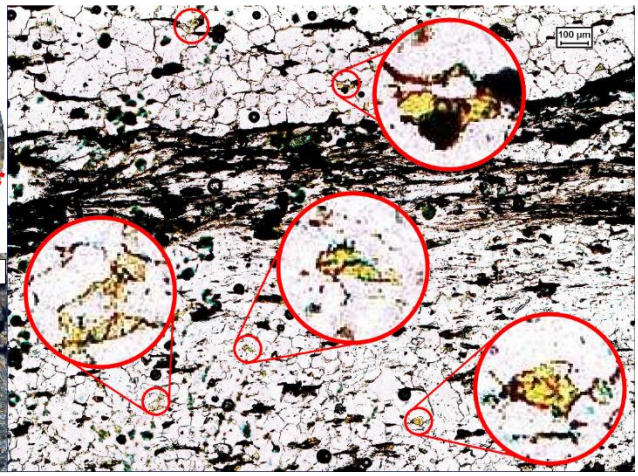

Figure 18. Thin-section fotograph (plane polarized light), showing some detrital staurolite crystals. Scale bar is 100 µm.

detailed analysis was outside of the scope of this project. The oxides may include illmenite, magnetite, hematite and rutile.

Structures

There are different generations of foliations visible in the thin-sections (*Appendix H*). The compositional layering is well-preserved, because of the strong compositional difference between the quartzitic and the pelitic layers. The strongest foliation, S_x, is present in all the pelitic domains. This S_x foliation is crenulating a different foliation, S_{x-1}, older than S_x. The penetrative foliation is folded (*figure 19; appendix H 1B,6,6i,9A,13A,14,15B,19*), and it appears that the S_{x-1} foliation is axial planar to these folds. It is chronologically impossible that D_{x-1} folded S_x, the folds can only be the result of a deformation phase post-dating D_x. A possible explanation is that a deformation phase, D_{x+1}, re-activated the S_{x-1} foliation during the folding of S_x. This implies that S_{x-1} is the result of both D_{x-1} and D_{x+1}. From here onwards, the bedding, S_{x-1} and S_x will be called S_0, S_{1+3} and S_2 respectively.

The S_{1+3} foliation (*appendix H, orange lines*) is a continuous foliation formed by elongated quartz and muscovite crystals. It is crenulated by S_2, so S_{1+3} is present in microlithons bordered by the S_2 planes. Iron oxides are present in between the elongated crystals, but it was not possible to determine the timing at which the oxides were formed. The oxides might have been formed during D_1, or they could have formed by precipitation along existing grain boundaries during a later event. The foliation must have formed during D_1, while it was reactivated during D_3.

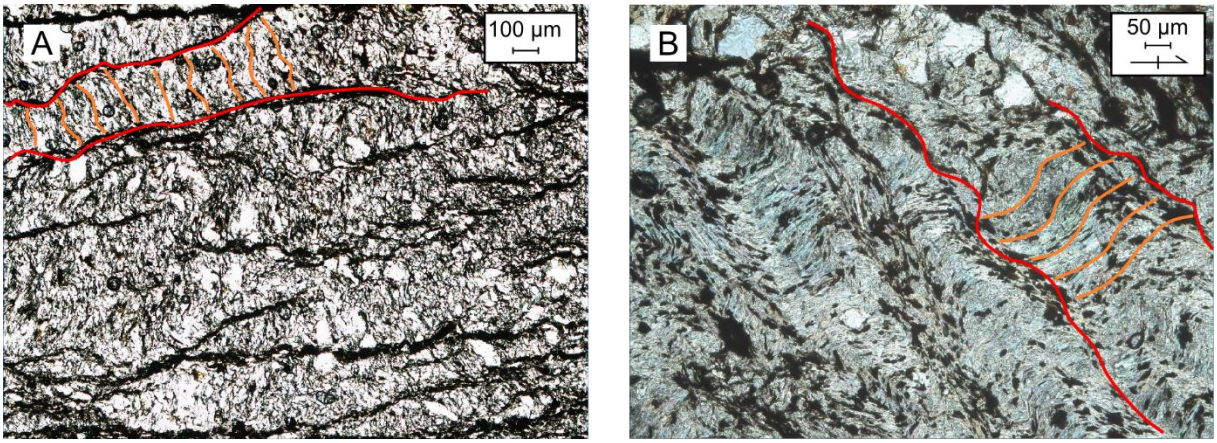

Figure 19. Thin-section photographs showing the folding of the S_2 (red) foliation. A) thin-section 6. B) thin-section 14.

S_2 (*Appendix H, red lines*) is a spaced foliation, defined by the orientation of muscovite and oxides. The shape of the cleavage domains is varying, ranging from a smooth to a wiggly pattern. The cleavage domains are spaced to zonal (cleavage domain area ranging from 5 to 50%), draw a parallel or anastomosing pattern and have a discrete transition to the microlithons. which appears to be depending on the lithological composition. The area-percentage occupied by the S_2 cleavage is also depending on the lithology. S_2 is better developed in pelitic layers, so the area-percentage increases with the amount of muscovite. This cleavage did not form in the quartzitic layers (*Appendix H, 9B*). It was not possible to determine the timing of the oxides in this foliation, whether they formed as part of the foliation or whether they were formed during a later event.

The folding of S_2 is not the only type of folding visible in the thin-sections, some folds of the compositional layering are also visible (*figure 20, appendix H, thin-section 9B*). The S_2 foliation is axial planar to this fold, so the fold could be the result from D_2 deformation. The layers are thickened in the hinge zone, while the flanks are thinned. This effect is developed more strongly in the less competent pelitic layer, where the flanks are thinned so much that they are not continuous anymore. This fold can be classified as a class 3 fold following the classification by Ramsay (1967). The image also shows how the S_2 foliation is fanning around the hinge, as a result of a strain shadow around the hinge of the more competent quartzitic layer. Another interesting feature is the more complex fold in the core of the fold, which could have formed because of limited space in the core.

Figure 20. High-quality scan of thin-section 9B, showing a thinning of the pelitic layers in the flanks of the fold, while it is thickened in the hinge zones.

Orientations

The orientation of the foliations in the thin sections allowed for the restoration of the true orientation of S_{1+3} and S_2 (*Figure 21*). The fold axis as derived from S_{1+3} is 279/11. This fold axis is most likely a combination of F_2 and F_3. The fold axis as derived from S_2, which is F_3, is 294/22. The plunge of the F_3 axis is steeper than the older fold axes. This is because the older axes were deformed by D_2, which was vertical flattening and thus lead to flattening of older structures.

Metamorphism

The outcrop has only been affected by low grade metamorphism during tectonic processes. The metamorphic assemblage for the first phase is formed by muscovite. The first foliation S_{1+3} has been overgrown at some places by larger muscovite crystals, which are limited to the microlithons of the S_2 crenulation foliation. The foliation of S_2 is formed by muscovite and oxides only, without any quartz.

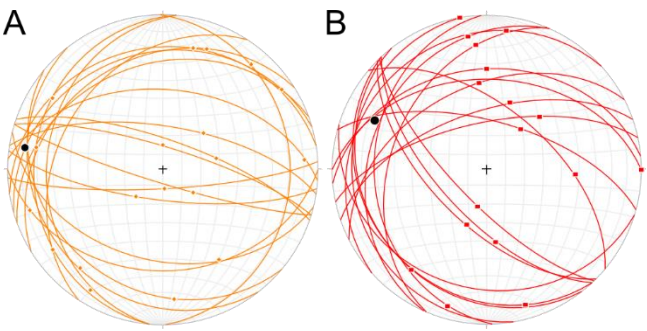

Figure 21. Equal area projections showing the orientations of planes measured from the thin sections. The symbols indicate the orientations measured in the thin sections. A) S_{1+3}. B) S_2.

Although staurolite is present in some of the thin sections (*figure 18*), it is found only in the quartzitic domains, but not in the pelitic domains. Staurolite growing in the quartzitic domains is possible, but more staurolite crystals would be expected in the pelitic domains. This is not the case, so the staurolite crystals are not the result of metamorphic growth, but they are detrital grains. This observation can still be used as an indication of metamorphic conditions. No metamorphic staurolite was formed, so the PT-conditions in these rocks remained below the staurolite field at all times.

The thin-sections also contain tourmaline crystals, consisting of a well-formed core with intense pleochroism and high interference colours, and some colourless overgrowths attached to these cores (*figure 17*). This type of tourmaline has been described in literature as detrital tourmaline with a metamorphic overgrowth (Henry & Dutrow 1992). Tourmaline can grow under a variety of metamorphic conditions, so it provides no information on the metamorphic grade of the outcrop. Tourmaline can be used as an indicator of the host rock conditions (van Hinsberg et al. 2011), but this requires detailed petrological analysis that was outside of the scope of this study.

Field measurements analysis

Measurements were taken from bedding, foliations, mullion axes, fold axes and intersection lineations (*figure 16*). This is the raw data that was used to retrodeform the outcrop. The youngest and latest deformation that formed structures at the scale of the outcrop is D_3. The orientation of this phase can be calculated from the folding of the S_2 foliation. The poles to S_2 plot on a greatcircle, which indicates that deformation was cylindrical (*figure 22*). The fold axis of D_3 deformation is 293/35.

Unfolding of the bedding plane around this fold axis allows for the restoration of the D_2 fold axis. This F_2 has been measured directly from D_2 mullions, and has also been calculated from the bedding planes around them. The measured D_2 axes are 010/30, the calculated axes are a bit steeper with an orientation of 043/14. These values are close together, so it will not have a large influence on the further analysis. Since D2 will be assumed to be sub-horizontal, we chose the most shallow orientation for of F_2 for unfolding the D_1 mullions.

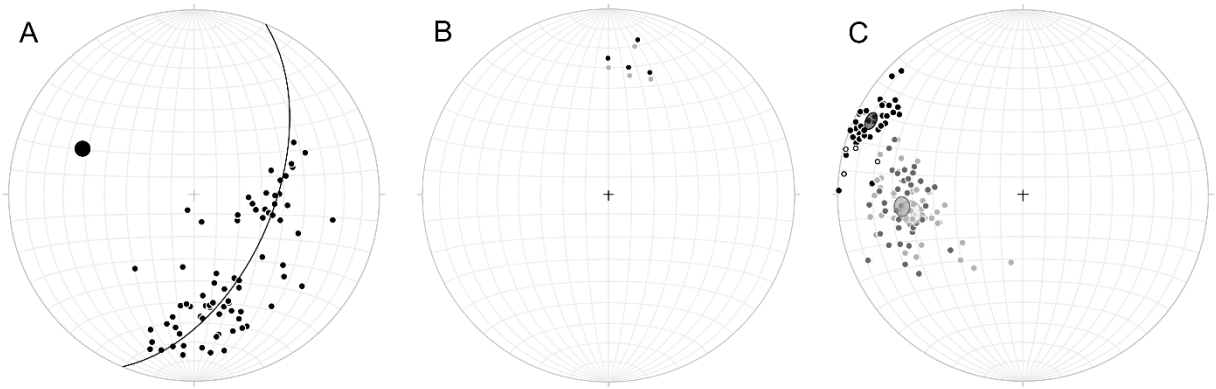

Figure 22. The results of the unfolding of the field measurements. A) The small dots represent the poles to the S_2 foliation, the greatcircle represents the best fitting plane through these points. The large dot is the pole to this greatcircle, and it represents the fold axis. B) Light grey dots represent the measured f_2 axes, the black dots represent the f_2 axes without the effect of D_3. C) Unfolding of D_1 mullions. The lightest grey dots represent the mullion axes as measured in the field, the intermediate grey dots represent the axis after undoing the effect of D_3, the black dots represent the fold axes after undoing the effects of D_2.

	n	Trend	Plunge	k	a95
D1 mullions post D3	45	261.2	38.8	20.8	6.0
D1 mullions post D2	45	264.8	34.8	32.3	4.8
Restored D1 mullion axis	45	294.7	07.3	43.4	4.1

Table 2. Orientation of the fold axis and statistics for different stages in the unfolding fo D_1 mullions.

Now that the fold axes of D_3 and D_2 are known, it is possible to retrodeform the D_1 mullions to their original orientations (*figure 22; table 2*). The measured D_1 mullions have a mean direction of 261/39. After undoing the effects of D_3, the mean orientation is 265/35. After undoing the effects of D_2, we find an original F_1 direction of 295/07. Both the orientation and the clustering of the F_1 directions change with each unfolding step. There is a better clustering after each step, which can be seen from different statistical parameters (*table 2*).

Directions from outcrop-scale measurements and thin sections are consistent, although there are some small differences in the plunge of the axes. The directions of F_1 and F_3 are close, and the foliation S_{1+3} appears to be the result of two separate phases. This similarity in direction will be discussed in more detail in the discussion chapter.

Discussion

Data interpretation

Paleomagnetism

Most of the directions from syn-kinematic granites have the expected shallow inclination, but there are some exceptions. For the syn-kinematic granites, sites GR2, GR6 and GR10 have an inclination that is steeper than expected. The assumption is made that the granites are undeformed at the sampled locations, but this is impossible to test because there is no good control of the structural evolution of the sampled granites. A possible explanation for the steep inclinations is that the granites have been tilted during later deformation. Despite the steep orientation, the directions of GR2 and GR10 still have the same declination as the other syn-kinematic granites. Therefore, I interpret the directions from these sites as valid, despite being tilted by later deformation. Site GR6 has a different declination, which is pointing to the south. The outcrop where the handsample was taken might have been a loose block, or the direction might correspond to a Cretaceous direction. Therefore, site GR6 will be discarded.

Another site of the syn-kinematic granites, with a different direction, is site GR1. This site does have the expected shallow inclination, but the direction is more towards the south than the other syn-kinematic granites. The magnetic behaviour of this site is also different, with a very clear signal with a much higher intensity compared to the other syn-kinematic sites. The direction of GR1 is similar to the Permian pole of Iberia, as described by Weil et al. (2010). This leads to two possible explanations: 1) site GR1 is remagnetized by later post-kinematic intrusions, or 2) site GR1 has been misinterpreted before, and forms part of the post-kinematic granites instead of the syn-kinematic granites. An age constraint on this granite is needed to distinguish between both options.

Another feature of the syn-kinematic magnetic directions is the range of declinations, that are varying from pointing NNE to SE. The sites that are pointing more to the SE are GR3, GR7 and GR8. There are some possible explanations for this feature. A map showing the paleomagnetic directions (*figure 23*) shows that the syn-kinematic sites with the more SE orientation are located around a post-kinematic granite. A good explanation for the orientation is the influence from the post-kinematic granites, leading to a remagnetization of the older granites.

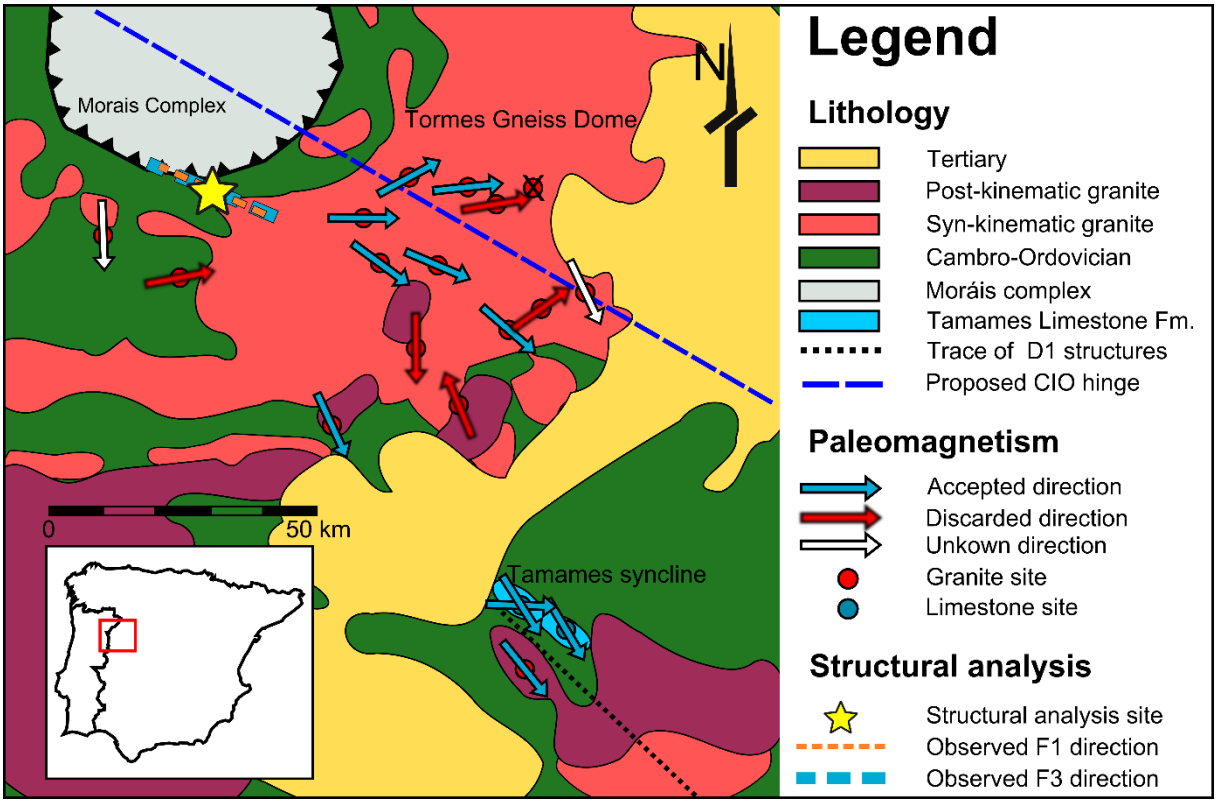

Figure 23. Overview map that shows the results of this study. The arrows are indicating the paleomagnetic directions, while the lines at the structural analysis location show the orientation of the different structures.

The paleomagnetic vectors from the post-kinematic granites plot in two different positions. GR4 has a direction of 337/64, which I interpret as a present day field direction. The direction from this site is thus an overprint, and the site can therefore be discarded. Sites GR5 and GR14, that represent two different locations, have a similar direction. This direction corresponds to the Permian pole for Iberia (Weil et al. 2010). Since the Permian represents the end of any Variscan deformation, no rotations occurred after this time.

The Ordovician sediments have been sampled at two locations only. Site PM1 yielded good paleomagnetic result, with a consistent direction. However, this direction is hard to interpret, because the mean direction is pointing south (178/-5), which is even more south than the Permian direction for Iberia. The rocks from this site are very magnetic (*figure 9*), and the orientation was measured with a regular compass, so there might be an inaccuracy in the measured orientation. Therefore, this site is discarded from further analysis. More measurements might help solve this problem, with cores oriented with a sun compass instead of a magnetic compass. Site PM2 has an inclination that is too steep, so the site is discarded as well.

The Tamames limestones show a range of directions, ranging from E to SE. The directions from the Tamames limestone plot in between the extreme directions of the syn-kinematic and the post-kinematic granite, while they show overlap with part of the syn-kinematic granites (*figure 24*). Another feature of the Tamames limestones is the magnetic carrier, fine-grained pyrrhotite, which is the result of chemical alteration related to fluids. The fold-test gave a negative result, meaning that the magnetization was obtained after folding, which is the result of D_1 deformation. The best clustering in the fold-test was found to be at -25% unfolding, which might indicate a later event took place after the magnetization of the rocks. Because of the range of the directions, I interpret the directions from the Tamames limestone as the result of remagnetization during rotation. The best explanation for this remagnetization is the influence of fluids related to the emplacement of the post-kinematic granites.

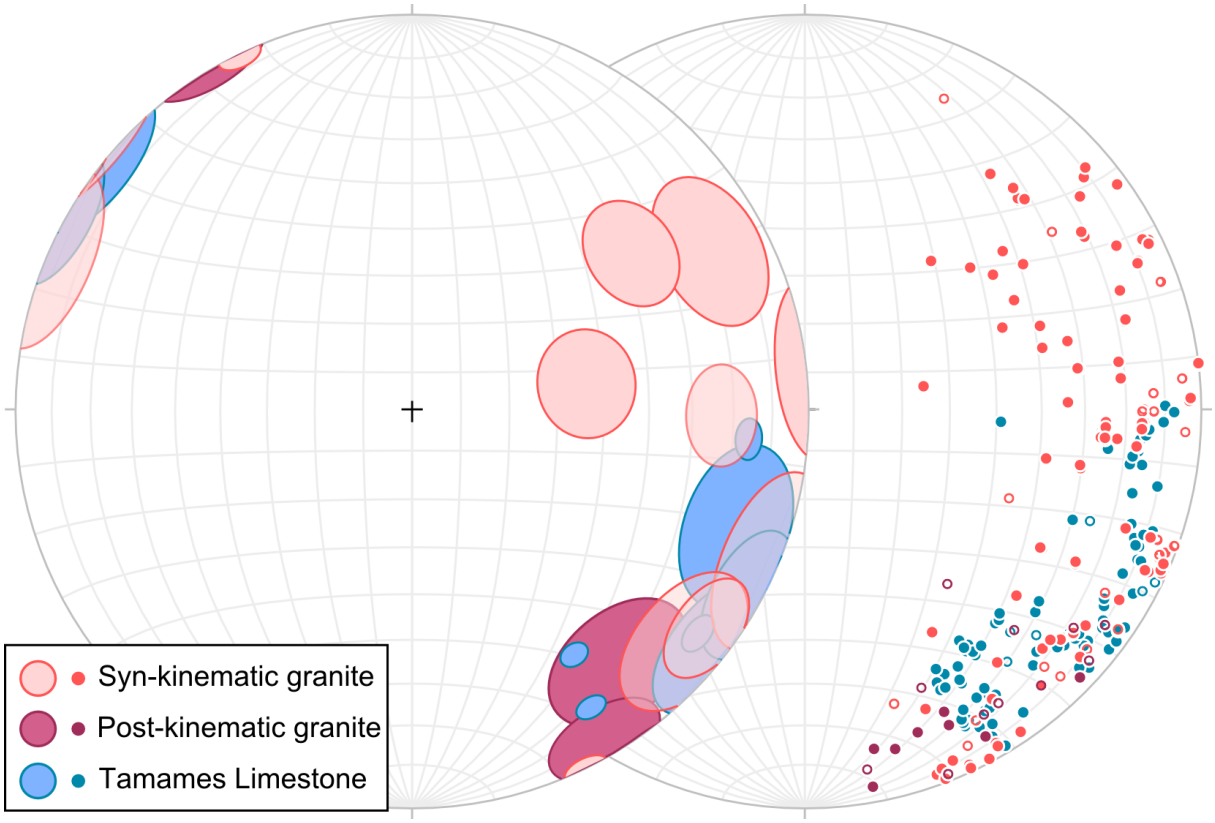

Figure 24. Equal area projection showing all the accepted paleomagnetic results in the same plot. The left plot shows the site means with the a95 confidence interval, while the right plot shows all the individual directions.

The remagnetization of the limestone by fluids can explain different characteristics as well, like the partial dolomitization of the rock. A possible explanation for the range of direction can be related to the initial porosity of the layers. The porosity is important for letting the first fluids through, to initialise the alteration of the rock. I searched for a spatial relationship between paleomagnetic directions in the limestone and the site locations, but no spatial relationship was found. A more detailed study, with a higher sampling resolution, is required to constrain a possible pattern of the magnetic directions throughout the Tamames limestone.

The directions from all sites combined show a range of directions (*figure 24*), ranging from syn-kinematic granite directions that are similar to directions from the southern hinge of the CO (Weil et al. 2013; Van der Voo 2004) to post-kinematic granites that have the Permian pole of Iberia (Weil et al. 2010). Some of the syn-kinematic granites and all of the Tamames limestones have been remagnetized by the post-kinematic granites. The syn-kinematic granites and the Tamames limestones were sampled at different locations around the hypothesized hinge of the CIO, but both show the same range of directions. Therefore, I conclude that no differential rotations occurred around the Morais complex.

The range of direction implies a counter-clockwise rotation of 100 degrees between 325 Ma and 300 Ma. Because the range of directions in the syn-kinematic granites and the Tamames limestones are best explained by remagnetization by the post-kinematic granites, the age constraint can be reduced. It is most likely that most of the rotation happened during the emplacement of the post-kinematic granites, which means that the rotations happened between 310 and 298 Ma (Gutiérrez-Alonso et al. 2011).

Structural analysis

The thin-sections contained chlorite and muscovite, but no staurolite or other medium to high-grade metamorphic minerals were observed. This constrains the metamorphism to the greenschist facies. There are high-grade rocks close to the studied outcrop, both in the allochthonous units and in the Tormes

Gneiss dome. The only explanation for the low-grade metamorphism in studied outcrop is that the outcrop formed part of the hanging wall, above the detachment along which the Tormes Gneiss dome was exhumed. If the Morais Complex would have been thrust over the rocks of the studied outcrop, the metamorphic grade would have been higher than it actually was.

Three deformation phases were observed in the outcrop, and the fold axes of all different phases have been calculated. These three phases were observed in the outcrop, but they can be placed into the regional structure of the area surrounding the Morais Complex. The youngest phase, called D_3 in the section, has the same type of structures and the same orientation as the regional D_3 phase, so both can be correlated.

The second oldest phase, called D_2 in the section, formed a penetrative foliation and folds with a subhorizontal fold axis. This phase can be correlated to the regional D_2 phase, which is related to orogenic collapse and the emplacement of metamorphic domes. The orogenic collapse is a gravitational effect, so the largest principal stress is vertical, which explains the subhorizontal foliation. Emplacement of the metamorphic domes lead to heating of the crust and peak-metamorphic conditions, which explains why the S_2 foliation is so penetrative (Dias da Silva 2013).

The D_1 phase from the section can be correlated to the regional D_1 phase, because it has been folded by D_2. Understanding the exact geometry of D_1 is difficult, because the two later phases reworked the oldest structures. D_1 structures have been interpreted to be trending NE-SW close to the section (*figure 4; figure 5*), but the data from this study shows that their original orientation is oriented NNW-SSE.

The unfolding of the D_1 mullions was based on some assumptions, because the mullions were restored by unfolding the fold axes together with the bedding plane. But the fold interference of the different phase made it impossible to determine the exact orientation of the bedding plane after the D_1 and the D_2 phase. However, the clustering of the measured mullion axes did show a better clustering after each unfolding step, which is a good indication that the unfolding results are valid.

The structural analysis revealed that the fold axes of D_1 and D_3 have approximately the same orientation. The evidence for similar directions between both phases was obtained from two different results of the structural analysis. The first results that infers coaxiality is the same direction of the fold axes of D_1 and D_3. Undoing the effects of D_3 and D_2 yielded a fold axis of 295/07 for D_1. This orientation is close to the fold axis of D_3, which is 295/35. Similar directions have been obtained from the thin section analysis, with the fold axis from S_{1+3} being 279/11 and F_3 as calculated from the S_2 foliation is 294/22.

Although the directions are the same, there is a difference in the plunge between both fold axes. The measured D_3 axis is steeper. This can be the result of large D_1 folds, if this phase resulted in tilting the bedding planes to a steep orientation at this location. Since the quartzite layers are so competent, the orientation of any later structures will be influenced by the orientation of these layers. This is compatible with observations from the outcrop, where the S_2 foliation is oriented sub-parallel to the quartzite layers at the interface between quartzite and pelite layers.

The second result that infers similar directions for D_1 and D_3 is the geometry of the foliations that were observed in thin section. The S_2 foliation is crenulating the S_{1+3} foliation, while it is also folded by this same foliation. This can only be the case if the directions of D_1 and D_3 are similar, where D_3 reactivated the S_1 foliation.

Because of the similarity in the fold axis orientations and the foliation geometries, I conclude that D_1 and D_3 are coaxial. The coaxiality between D_1 and D_3 implies that the CIO cannot be a secondary orocline formed by buckling (*figure 8*). The outcrop is situated in the hinge of the orocline, so perpendicular directions would be expected between D_1 and D_3 if the orocline is formed by buckling.

Comparison with previous results

The results from this study can be combined with the results from previous studies (*figure 25*). Several data sets concerning the geometry of the CIA exist, based on a variety of data sets: fold interference patterns (Aerden 2004) and the structural trend of Variscan structures (Aerden 2004; Martínez Catalán 2011b; Shaw et al. 2012) crustal magnetic lineations (Aerden 2004; Martínez Catalán 2011b), and paleoflow directions (Shaw et al. 2012).

The axial trace of Variscan structures is inferred to represent the curvature that forms the CIO. However, the Variscan outcrops are fragmented, especially in the eastern part of the orocline. Therefore, it is hard to delimit a full geometry based on these structures. There are some curved segments in the south, but while these could represent oroclinal curvature, they could also be explained by other local effects, like the exhumation of the granite domes. The southern part of the Variscan outcrops could also be affected

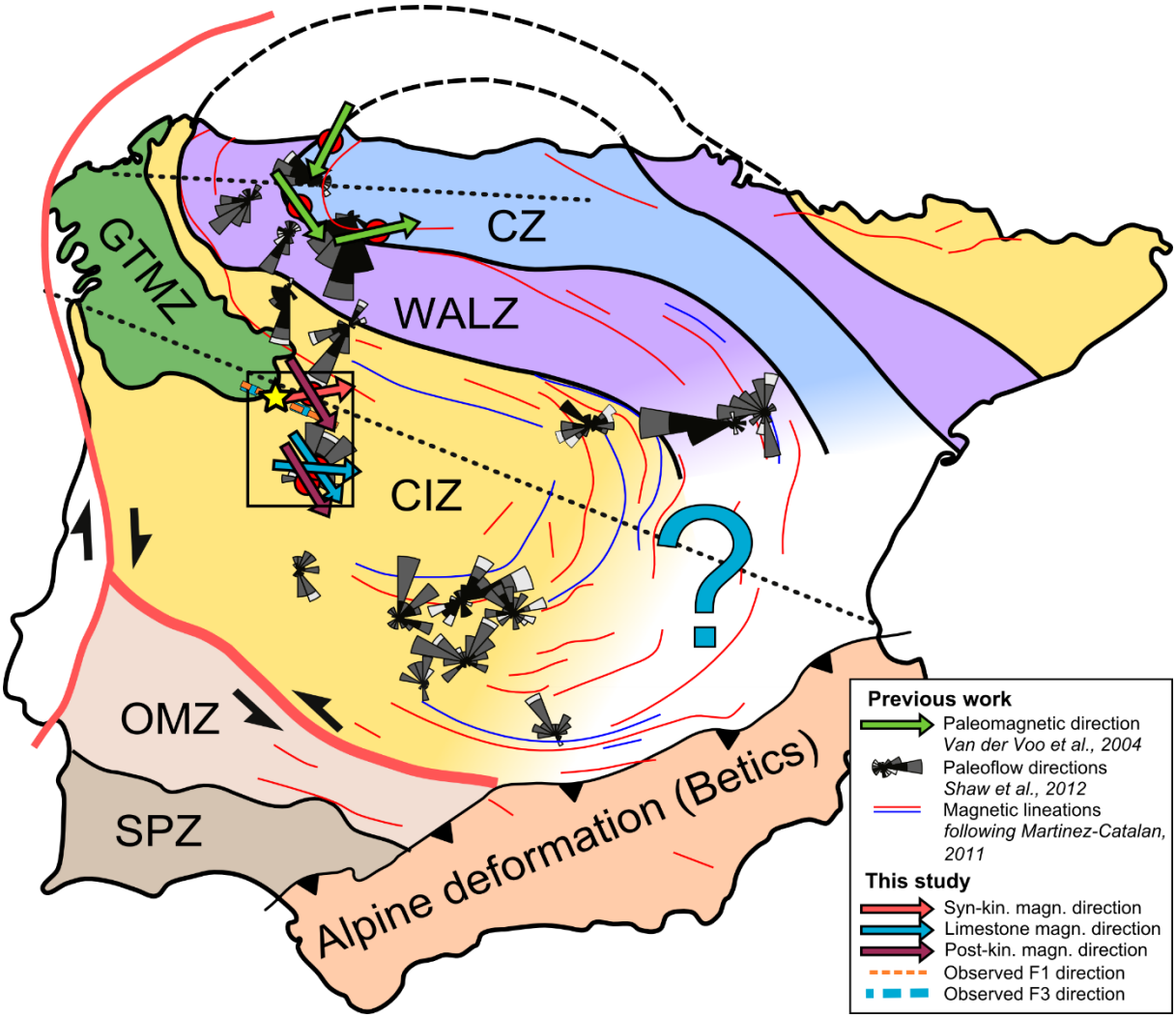

Figure 25. Map of Iberia showing a combination of data sets concerning the CIO, both from this study and from previous studies.

by Alpine deformation, with some possible curvature, although a better understanding of the influence of the Alpine deformation is required to test this possibility.

The magnetic lineations (*figure 25*) are based on aeromagnetic anomalies. They are inferred to represent the axial traces of Variscan folds, or to represent ultrabasic rocks in the allochthonous complexes. However, the interpretation that the magnetic anomalies delineate an orocline is not the only possible interpretation. Some of the large rounded magnetic highs can be correlated with the granitic domes

related to the Variscan. Some other structures do not necessarily represent Variscan structures, since some of the magnetic lows can be correlated with the Tertiary basins.

Paleoflow directions were also used for delineating an orocline (*figure 3; figure 25*). It is assumed that the paleoflow structures formed at a 90 degree angle to the coastline. Whereas this may be true, the orientation of the former coastline is not known. At the present-day, few coastlines are straight, so local variation in the coastline orientation could control the results of paleoflow structures. It is clear that the paleoflow directions delimit a rotation, but it is uncertain what this rotation represents. One paleoflow direction was obtained at the Tamames syncline, and while the paleoflow direction indicates a direction opposite to that of the southern flank of the CO, the paleomagnetic data from this study indicate that no rotations occurred in this area. Therefore, there needs be an alternative explanation for the paleoflow directions, which could be related to local effects.

New possible geometries

The data that is presented in this study shows that the Morais complex is not in the hinge of the orocline, because the same paleomagnetic directions are observed in both the Tormes Gneiss dome and the Tamames syncline, so there are no differential rotations. Furthermore, the structural trends D_1 and D_3 are coaxial, where perpendicular orientations are expected if the orocline is secondary and formed by buckling. The paleomagnetic directions are similar to those from the southern flank of the CO, and the area surrounding the Morais complex can be interpreted to form part of the southern flank of the CO. Because this new data is not compatible with the geometries that were proposed before (*figure 2*; (Aerden 2004; Martínez Catalán 2011b; Shaw et al. 2012), I will propose three new geometries that are consistent with the presented data (*figure 26*).

Our data can only constrain part of the geometry of any possible CIO, since the studied area is located around the hypothesized hinge only. More research is needed in areas to the south and to the east of the area from this study, to better constrain the full geometry of the Iberian Variscides.

The first option is that the CIO represents a progressive orocline, which was produced during the initial collision between Gondwana and Laurussia. The orocline could be the result of indentation, the emplacement of a lateral extrusion wedge (i.e. the GTMZ) or some other process. This is a geometry that can be compatible with the Morais complex being in the hinge. Since the orocline would be the result of the initial collision, any rotations related to the orocline formation will not be recorded through paleomagnetic directions if the magnetization is obtained after this event. This option is compatible with all the other data sets, since there is an orocline. The structures are curved as suggested, the magnetic lineations could represent orogenic curvature, and the paleoflow directions delimit an orocline.

The second option, using the definition that an orocline is the curvature of a full orogenic belt, is that there is no CIO. Any curvature is, therefore, apparent. This apparent curvature could be the result of processes like orogenic collapse, topography, thin skinned tectonics or fold interference patterns. This geometry is consistent with the data from this study, that indicate no differential rotations occurred in the area surrounding the Morais complex. This geometry requires a different interpretation of the aeromagnetic data and the paleoflow directions.

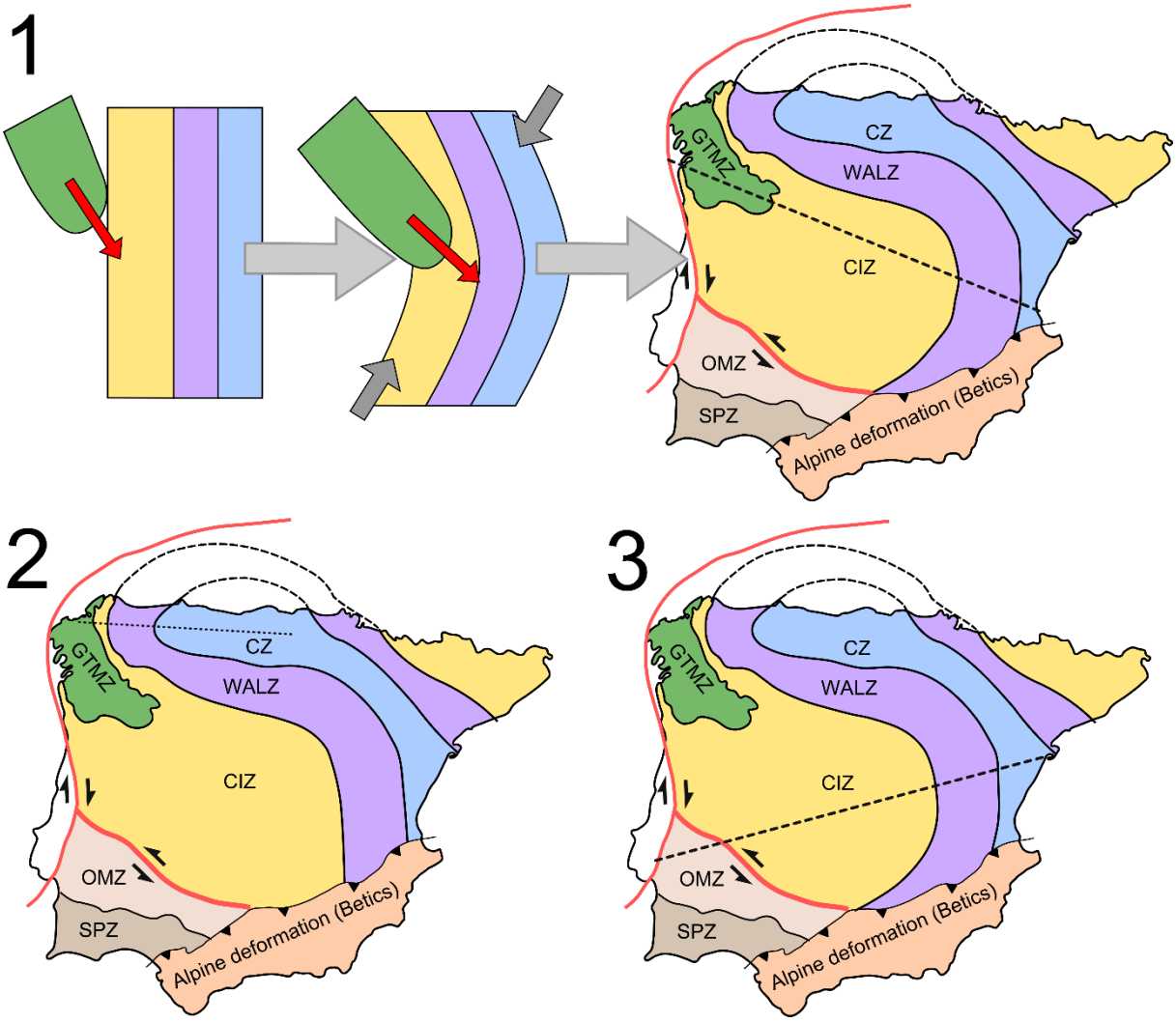

Figure 26. Three possible options for the geometry of the Iberian Variscides. 1) The CIO is a progressive orocline produced during collision (e.g. result of indentation, lateral extrusion wedge). 2) There is no orocline, following the definition that an orocline represents the curvature of a full mountain belt. The curvature is apparent (e.g. result of orogenic collapse, topography, thin-skinned tectonics, fold interference patterns). 3) The hinge of the orocline is situated to the south of Tamames.

The third option is that the CIO does exist as a secondary Variscan feature, but the hinge of the orocline is situated to the south of Tamames. This means the rotations, which have not been recorded by our data, only occurred further to the south. The axial trace could not be parallel to the D_3 trend, but a more NE-SE oriented axial trace is required. This option is consistent with the structural trend and the aeromagnetic data that was published by (Aerden 2004; Martínez Catalán 2011b), but there is an inconsistency with the paleoflow direction obtained from the Tamames syncline that indicates that the area forms the southern flank. This locality was affected by both an unconformity and a folding phase, so it is possible that the paleoflow direction could be restored in a different way, taking into account the history of the area. The data set from this study can only constrain the northern part, so more paleomagnetic data to the south of this proposed hinge is needed to better constrain the possibility of this geometry.

Conclusion

The geometry of the Central Iberian Orocline is not well constrained. Previous works describe the arc as a secondary orocline with the Morais allochthonous complex in its hinge, although the models do not agree on the precise geometry of the CIO. In this document, new data is presented from paleomagnetism and a structural analysis, to better constrain the geometry of the CIO.

The paleomagnetic analysis reveals a range of directions, ranging from ENE to SE in syn-kinematic granites, from E to SE in limestones of the Tamames syncline, and post-kinematic granites have a direction pointing to the SE. The syn-kinematic granites and the Tamames limestones were remagnetized by the post-kinematic granites, during a rotation, which explains the range of directions. The range of directions is observed in both the Tormes Gneiss dome and the Tamames syncline, indicating that no differential rotations occurred between those two locations. The ENE direction is similar to paleomagnetic directions from the southern hinge of the Cantabrian Orocline, while the SE directions represent the Permian direction and the end of any rotation.

Results from the structural analysis of a section in the hypothesized hinge of the CIO indicate that the fold axes of D_1 and D_3 have the same direction. Thin-section analysis showed that D_1 and D_3 had the same orientation, because D_3 reactivated the older S_1 foliation to fold the S_2 foliation. The directions of D_1 and D_3 are parallel, which means that the Morais complex cannot be situated in the core of a secondary orocline that is related to D_3 deformation.

The results from the paleomagnetic directions and the structural analysis are not consistent with previously published models for the geometry of the CIO. With the new data from this study, we propose three possible scenarios: 1) the CIA is a progressive arc, formed during the initial collision before the emplacement of the syn-kinematic granites, 2) there is no orocline that represents the curvature of the full Variscan belt, and the curvature is therefore apparent and 3) the hinge of the orocline is situated to the south of Tamames.

Acknowledgments

I would like to thank Daniel Pastor Galán for everything that he has done in supervising this project, which is way too much to describe in this place, but all of which made this MSc research project an incredible learning experience. I would like to thank Daniel Pastor Galán and Wout Krijgsman for their useful comments on the first version of this document, which helped greatly in improving this thesis. I would like to thank Icaro Frois Dias da Silva and Gabriel Gutierrez Alonso for their help in the field, and for their help in sampling and sending extra samples when the need was there. My thanks also goes to Maxim Krasnoperov for keeping the paleomagnetic measuring equipment up and running, to Otto Stiekema for preparing the thin-sections, and to the people at the glass works for letting me drill the handsamples in their workshop. I would also like to thank all the people at Fort Hoofddijk for making it such a nice place, with a special thank you to my fellow students, who were always there to discuss the basic problems that are also part of writing a thesis.

References

Aerden, D.G.A.M., 2004. Correlating deformation in Variscan NW-Iberia using porphyroblasts; implications for the Ibero-Armorican Arc. *Journal of Structural Geology*, 26(1), pp.177–196.

Álvaro, J.J. et al., 2003. Palaeogeographical controls on the Cambrian trilobite immigration and evolutionary patterns reported in the western Gondwana margin. *Palaeogeography, Palaeoclimatology, Palaeoecology*, 195, pp.5–35.

Arango, C., Fernandez, R.D. & Arenas, R., 2013. Large-scale flat-lying isoclinal folding in extending lithosphere: Santa Maria de la Alameda dome (Central Iberian Massif, Spain). *Lithosphere*, 5(5), pp.483–500.

Ardizone, J., Mezcua, J. & Socias, I., 1989. Mapa aeromagnético de España Peninsular.

Azor, A., González Lodeiro, F. & Fernando Simancad, J., 1994. Tectonic evolution of the boundary between the Central Iberian and Ossa-Morena zones (Variscan belt, southwest Spain). *Tectonics*, 13(1), pp.45–61.

Ballèvre, M. et al., 2014. Correlation of the nappe stack in the Ibero-Armorican arc across the Bay of Biscay: a joint French-Spanish project. *Geological Society, London, Special Publications*, 405(1), pp.77–113.

Bea, F., Montero, P. & Molina, J.F., 1999. Mafic Precursors, Peraluminous Granitoids, and Late Lamprophyres in the Avila Batholith: A Model for the Generation of Variscan Batholiths in Iberia. *The Journal of Geology*, 107, pp.399–419.

Bea, F., Montero, P. & Zinger, T., 2003. The Nature , Origin , and Thermal Influence of the Granite Source Layer of Central Iberia The Nature , Origin , and Thermal Influence of the Granite Source Layer of Central Iberia. *The Journal of Geology*, 111(5), pp.579–595.

Braid, J.A. et al., 2011. Tectonic escape of a crustal fragment during the closure of the Rheic Ocean: U-Pb detrital zircon data from the Late Palaeozoic Pulo do Lobo and South Portuguese zones, southern Iberia. *Journal of the Geological Society*, 168(2), pp.383–392.

Budd, C.J. & Peletier, M.A., 2000. Approximate self-similarity in models of geological folding. *Society for Industrial and Applied Mathematics*, 60(3), pp.990–1016.

Cardozo, N. & Allmendinger, R.W., 2013. Spherical projections with OSXStereonet. *Computers & Geosciences*, 51, pp.193–205.

Carey, S.W., 1955. The Orocline Concept in Geotectonics. *Papers and Proceedings of the Royal Society of Tasmania*, 89, pp.255–288.

Corrales, I., Manjón, M. & Valladares, M.I., 1974. La serie carbonatada de Navarredonda de la Rinconada (Salamanca, España). *Studia Geologica*, pp.85–91.

Corrales, I. & Valladares, I., 1980. Facies carbonatadas del Cambrico de Salamanca. *Studia Geologica Salmanticensia*, 16, pp.95–102.

Dallmeyer, R.D. et al., 1997. Diachronous Variscan tectonothermal activity in the NW Iberian Massif : Evidence from 40 ArP9 Ar dating of regional fabrics. *Tectonophysics*, 277, pp.307–337.

Dekkers, M.J., 1988. Magnetic properties of natural pyrrhotite Part I: Behaviour of initial susceptibility and saturation-magnetization-related rock-magnetic parameters in a grain-size dependent framework. *Physics of the Earth and Planetary Interiors*, 52(3-4), pp.376–393.

Dekkers, M.J., 1989. Magnetic properties of natural pyrrhotite. II. High- and low-temperature behaviour of Jrs and TRM as function of grain size. *Physics of the Earth and Planetary Interiors*, 57(3-4), pp.266–283.

Dias da Silva, Í., 2009. Estructura y Evolución Tectónica del Área de Palaçoulo , Este del Complejo de Morais , Portugal a Ícaro Fróis Dias da Silva.

Dias da Silva, Í., 2013. Geología de las zonas Centro Ibérica y Galicia-Trás-os-Montes en la parte oriental del Complejo de Morais, Portugal/España.

Dias, G. et al., 1998. U-Pb zircon and monazite geochronology of post-collisional Hercynian granitoids from the Central Iberian Zone (Northern Portugal). *Lithos*, 45, pp.349–369.

Dias, R. & Ribeiro, A., 1995. The Ibero-Armorican Arc: A collision effect against an irregular continent? *Tectonophysics*, 246, pp.113–128.

Diez Balda, M.A., Martínez Catalán, J.R. & Ayarza Arribas, P., 1995. Syn-collisional extensional collapse parallel to the erogenic trend in a domain of steep tectonics : the Salamanca Detachment Zone (Central Iherian Zone , Spain). *Journal of Structural Geology*, 17(2), pp.163–182.

Diez Balda, M.A., Vegas, R. & González Lodeiro, F., 1990. Central Iberian Zone. Structure. In *Pre-Mesozoic Geology of Iberia (Edited by Dallmeyer, R.D. and Martínez García, E.) Springer-Verlag, Berlin,*. pp. 172–188.

Díez Fernández, R. et al., 2013. Crustal thickening and attenuation as revealed by regional fold interference patterns: Ciudad Rodrigo basement area (Salamanca, Spain). *Journal of Structural Geology*, 46, pp.115–128.

Fernandez, F.., Diaz-Garcia, F. & Marquinez, J., 2011. Kinematics of the Forcarei Synform (NW Iberian Variscan belt). *Geological Society, London, Special Publications*, 349(1), pp.185–201.

Fernández-Suárez, J. et al., 2000. Variscan collisional magmatism and deformation in NW Iberia : constraints from U – Pb geochronology of granitoids. *Journal of the Geological Society*, 157, pp.565–576.

Franke, W. & Zelazniewicz, a., 2002. Structure and evolution of the Bohemian Arc. *Geological Society, London, Special Publications*, 201(1), pp.279–293.

Gómez Barreiro, J. et al., 2007. Tectonic evolution of the upper allochthon of the Órdenes complex (northwestern Iberian Massif): Structural constraints to a polyorogenic peri-Gondwanan terrane. *Geological Society of America Special Paper*, 423, pp.315–332.

Gutiérrez-alonso, G. et al., 2012. Buckling an orogen : The Cantabrian Orocline. *GSA Today*, 22(7), pp.4–9.

Gutiérrez-Alonso, G. et al., 2011. Diachronous post-orogenic magmatism within a developing orocline in Iberia, European Variscides. *Tectonics*, 30(5), p.n/a–n/a.

Gutiérrez-Alonso, G., Fernández-Suárez, J. & Weil, A.B., 2004. Orocline triggered lithospheric delamination. *Geological Society of America*, Special pa(2), pp.121–130.

Henry, D.J. & Dutrow, B.L., 1992. Tourmaline in a low grade clastic metasedimentary rock: an example of the petrogenetic potential of tourmaline. *Contributions to Mineralogy and Petrology*, 112(2-3), pp.203–218.

Van Hinsberg, V.J., Henry, D.J. & Marschall, H.R., 2011. Tourmaline: an ideal indicator of its host environment. *The Canadian Mineralogist*, 49, pp.1–16.

Johnston, S.T. et al., 2009. The significance of bent mountain belts. *Trabajos de Geología, Universidad de Oviedo*, 29, pp.388–392.

Johnston, S.T., Weil, A.B. & Gutierrez-Alonso, G., 2013. Oroclines: Thick and thin. *Geological Society of America Bulletin*, 125(5-6), pp.643–663.

Julivert, M. et al., 1972. Mapa tectónico de la península ibérica y baleares. , p.44.

Kenis, I. et al., 2004. Mullions in the High-Ardenne Slate Belt (Belgium): numerical model and parameter sensitivity analysis. *Journal of Structural Geology*, 26(9), pp.1677–1692.

Kenis, I. et al., 2005. Rheology of fine-grained siliciclastic rocks in the middle crust—evidence from structural and numerical analysis. *Earth and Planetary Science Letters*, 233, pp.351–360.

Kirschvink, J.L., 1980. The least-squares line and plane and the analysis of palaeomagnetic data. *Geophysical Journal International*, 62(3), pp.699–718.

Liñán, E. et al., 2004. *The Cambrian System in Iberia*,

López-Moro, F.J. et al., 2014. The magmatic response to the Variscan Belt collapse in Iberia . U-Pb LA -ICP-MS ages of syn-kinematic granitoids in the CIZ (Tormes Dome , western Iberia). *in: Gondwana 15 "North meets South" abstract book (http://eprints.ucm.es/26351/1/GONDWANA15%20FINAL_E-print.pdf)*, p.102.

López-Moro, F.J. & López-Plaza, M., 2004. Monzonitic series from the Variscan Tormes Dome (Central Iberian Zone): petrogenetic evolution from monzogabbro to granite magmas. *Lithos*, 72, pp.19–44.

Martinez Catalan, J.R. et al., 2014. The late Variscan HT/LP metamorphic event in NW and Central Iberia: relationships to crustal thickening, extension, orocline development and crustal evolution. *Geological Society, London, Special Publications*.

Martínez Catalán, J.R., 2011a. Are the oroclines of the Variscan belt related to late Variscan strike-slip tectonics? *Terra Nova*, 23(4), pp.241–247.

Martínez Catalán, J.R. et al., 2007. Space and time in the tectonic evolution of the northwestern Iberian Massif : Implications for the Variscan belt. *The Geological Society of America memoirs*, 200, pp.403–423.

Martínez Catalán, J.R., 2011b. The Central Iberian arc : implications for the Iberian Massif. *Geogaceta*, 50(1), pp.7–10.

Martínez Catalán, J.R., 2012. The Central Iberian arc, an orocline centered in the Iberian Massif and some implications for the Variscan belt. *International Journal of Earth Sciences*, 101(5), pp.1299–1314.

Martínez Catalán, J.R. et al., 1997. Variscan accretionary complex of northwest Iberia : Terrane correlation and succession of tectonothermal events. *Geology*, 25(12), pp.1103–1106.

Matte, P., 1986. Tectonics and plate tectonics model for the Variscan belt of Europe. *Tectonophysics*, 126, pp.329–374.

Matte, P., 2001. The Variscan collage and orogeny (480 - 290 Ma) and the tectonic definition of the Armorica microplate : a review. *Terra Nova*, 13(2), pp.122–128.

Matte, P. & Ribeiro, A., 1975. Forme et orientation de l'ellipsoïde de déformation dans la virgation hercynienne de Galice; relations avec le plissement et hypothèses sur la genèse de l'arc ibéro-armoricain. *CR Acad. Sci., Ser. D*, 280, pp.2825–2828.

Mullender, T.A.T., van Velzen, A.J. & Dekkers, M.J., 1993. Continuous drift correction and separate identification of ferrimagnetic and paramagnetic contributions in thermomagnetic runs. *Geophysical Journal International*, 114, pp.663–672.

Murphy, J.B. et al., 2006. Origin of the Rheic Ocean: Rifting along a Neoproterozoic suture? *Geology*, 34(5), p.325.

Nance, R.D. et al., 2010. Evolution of the Rheic Ocean. *Gondwana Research*, 17(2-3), pp.194–222.

Pamplona, J., Gutiérrez-Alonso, G. & Ribeiro, A., 2006. Superposition of shear zones during orogenic development: an example from the NW Variscan Belt (Viana do Castelo, NW Portugal). *Journal of Structural Geology*, 28(7), pp.1327–1337.

Passchier, C.W. & Trouw, R.A.J., 2005. *Microtectonics*, Berlin, Heidelberg: Springer Berlin Heidelberg.

Pastor-Galán, D. et al., 2012. Conical folding in the core of an orocline. A geometric analysis from the Cantabrian Arc (Variscan Belt of NW Iberia). *Journal of Structural Geology*, 39, pp.210–223.

Pastor-Galán, D. et al., 2009. Factors affecting finite strain estimation in low-grade, low-strain clastic rocks. *Journal of Structural Geology*, 31(12), pp.1586–1596.

Pastor-Galán, D. et al., 2013. Provenance analysis of the Paleozoic sequences of the northern Gondwana margin in NW Iberia: Passive margin to Variscan collision and orocline development. *Gondwana Research*, 23(3), pp.1089–1103.

Pastor-Galán, D., Gutiérrez-Alonso, G. & Weil, A.B., 2011. Orocline timing through joint analysis: Insights from the Ibero-Armorican Arc. *Tectonophysics*, 507(1-4), pp.31–46.

Pereira, M.F. et al., 2012. North-Gondwana assembly, break-up and paleogeography: U–Pb isotope evidence from detrital and igneous zircons of Ediacaran and Cambrian rocks of SW Iberia. *Gondwana Research*, 22(3-4), pp.866–881.

Pérez-Estaún, A., Martinez-Catalán, J.R. & Bastida, F., 1991. Crustal thickening and deformation sequence in the footwall to the suture of the Variscan belt of northwest Spain. *Tectonophysics*, 191(3-4), pp.243–253.

Quesada, C., 1991. Geological constraints on the Paleozoic tectonic evolution of tectonostratigraphic terranes in the Iberian Massif. *Tectonophysics*, 185(3-4), pp.225–245.

Ramón, M.J. & Pueyo, E.L., 2012. VPD Virtial Paleomagnetic Directions: User's manual (January 2012).

Ramsay, J.G., 1967. Folding and Fracturing of Rocks. In *Folding and Fracturing of Rocks*. p. 568.

Rochette, P. et al., 1990. Magnetic transition at 30-34 Kelvin in pyrrhotite : insight into a widespread occurrence of this mineral in rocks. *Earth and Planetary Science Letters*, 98, pp.319–328.

Rodríguez-Alonso, M.D. et al., 2004. Neoproterozoic-Cambrian synsedimentary magmatism in the Central Iberian Zone (Spain): geology, petrology and geodynamic significance. *International Journal of Earth Sciences*, 93(5), pp.897–920.

Sá, A.A. et al., 2011. Ordovician vs. "Cambrian" ichnofossils in the Armorican Quartzite of Central Portugal. *Cuadernos del Museo Geominero*, 14, pp.483–492.

Shaw, J. et al., 2012. Oroclines of the Variscan orogen of Iberia: Paleocurrent analysis and paleogeographic implications. *Earth and Planetary Science Letters*, 329-330, pp.60–70.

Sokoutis, D., 1987. Finite strain effects in experimental mullions. *Journal of Structural Geology*, 9(2), pp.233–242.

Stampfli, G.M., von Raumer, J.F. & Borel, G.D., 2002. Paleozoic evolution of pre-Variscan terranes : From Gondwana to the Variscan collision. *Geological Society of America Special Paper*, 364, pp.263–280.

Tauxe, L., 2010. *Essentials of Paleomagnetism*,

Tauxe, L. & Watson, G.S., 1994. The fold test: an eigen analysis approach. *Earth and Planetary Science Letters*, 122(3-4), pp.331–341.

Torsvik, T.H. et al., 2012. Phanerozoic polar wander, palaeogeography and dynamics. *Earth-Science Reviews*, 114, pp.325–368.

Torsvik, T.H. & Renhström, E.F., 2001. Cambrian palaeomagnetic data from Baltica : implications for true polar wander and Cambrian palaeogeography. *Journal of the Geological Society, London*, 158, pp.321–329.

Ugidos, J.M. et al., 2003. The Upper Neoproterozoic–Lower Cambrian of the Central Iberian Zone, Spain: chemical and isotopic (Sm-Nd) evidence that the sedimentary succession records an inverted stratigraphy of its source. *Geochimica et Cosmochimica Acta*, 67(14), pp.2615–2629.

Valladares, J. & Corrales, I., 1980. Las series carbonatadas del cambrico inferior de Salamanca. In *IX Cong. Nac. Sedim., Salamanca, Guía de campo, 15-25 \ \ Univ. Salamanca*. pp. 15–25.

Valladares, M.I. et al., 2000. Upper Neoproterozoic- Lower Cambrian sedimentary successions in the Central Iberian Zone (Spain): sequence stratigraphy, petrology and chemostratigraphy. Implications for other European zones. *International Journal of Earth Sciences*, 89, pp.2–20.

Viruete, J.E., 1998. Relationships between structural units in the Tormes gneiss dome (NW Iberian massif, Spain): geometry, structure and kinematics of contractional and extensional Variscan deformation. *Geologische Rundschau*, 87(2), pp.165–179.

Viruete, J.E., Arenas, R. & Martínez Catalán, J.R., 1994. Tectonothermal evolution associated with Variscan crustal extension in the Tormes Gneiss Dome (NW Salamanca , Iberian Massif , Spain). *Tectonophysics*, 238, pp.117–138.

Van der Voo, R., 2004. Paleomagnetism, oroclines, and growth of the continental crust. *GSA Today*, 14(12), pp.4–9.

Wehland, F. et al., 2005. Pyrrhotite pTRM acquisition in metamorphic limestones in the light of microscopic observations. *Physics of the Earth and Planetary Interiors*, 151(1-2), pp.107–114.

Weil, A.B. et al., 2013. Kinematic constraints on buckling a lithospheric-scale orocline along the northern margin of Gondwana: A geologic synthesis. *Tectonophysics*, 582, pp.25–49.

Weil, A.B., Gutiérrez-Alonso, G. & Conan, J., 2010. New time constraints on lithospheric-scale oroclinal bending of the Ibero-Armorican Arc: a palaeomagnetic study of earliest Permian rocks from Iberia. *Journal of the Geological Society*, 167, pp.127–143.

Weil, A.B. & Sussman, A.J., 2004. structural development and vertical-axis rotations. *Geological Society of America Special Paper*, 383, pp.1–15.

Weil, A.B., van der Voo, R. & van der Pluijm, B.A., 2001. Oroclinal bending and evidence against the Pangea megashear : The Cantabria-Asturias arc (northern Spain). *Geology*, 29(11), pp.991–994.

Yenes, M., Álvarez, F. & Gutiérrez-Alonso, G., 1999. Granite emplacement in orogenic compressional conditions : the La Alberca-Béjar granitic area (Spanish Central System , Variscan Iberian Belt). *Journal of Structural Geology*, 21, pp.1419–1440.

Yonkee, A. & Weil, A.B., 2010. Quantifying vertical axis rotation in curved orogens: Correlating multiple data sets with a refined weighted least squares strike test. *Tectonics*, 29(3), p.n/a–n/a.

Zijderveld, J.D.A., 1967. A.C. Demagnetization of rocks: Analysis of Results. In *Methods in Paleomagnetism*. Elsevier, New York, pp. 254–286.

Appendix A: Paleomagnetism sampling locations

This appendix contains a table with the locations and the lithologies of the different sites that were sampled for the paleomagnetic analysis.

Site name	*GPS coordinates*		*lithology*
	N	*W*	
PM1	41.17947	006.95565	Quartzite
PM2	41.11808	006.79325	Meta-siltstone
PM3	40.58142	005.96717	Limestone
PM4	40.58395	005.97355	Limestone
PM5	40.61578	006.05967	Limestone
PM6	40.61802	006.06200	Limestone
PM7	40.61732	006.06475	Limestone
PM8	40.61498	006.06483	Limestone
PM9	40.61648	006.06468	Limestone
PM10	40.61838	006.06367	Limestone
GR1	41.10920	005.95855	Syn-kinematic granite
GR2	41.07690	006.05170	Syn-kinematic granite
GR3	41.04632	006.11660	Syn-kinematic granite
GR4	40.93180	006.21890	Post-kinematic granite
GR5	40.87937	006.47545	Post-kinematic granite
GR6	41.01770	006.30640	Syn-kinematic granite
GR7	41.12717	006.27337	Syn-kinematic granite
GR8	41.13060	006.39430	Syn-kinematic granite
GR9	41.21625	006.42568	Syn-kinematic granite
GR9B	41.27553	006.32751	Syn-kinematic granite
GR10	41.23810	006.15200	Syn-kinematic granite
GR11	41.26540	006.21340	Syn-kinematic granite
GR12	41.26806	006.07846	Syn-kinematic granite
GR14	40.51460	006.13450	Post-kinematic granite

Appendix B: Curie balance results

This appendix contains the results of the Curie Balance analysis. The thin line represents the heating curve, while the dark line represents the final cooling curve. The coloured dots in the upper left corner represent the different lithological groups: light red for the syn-kinematic granites, purple for the post-kinematic granites, brown for the Ordovician sediments and blue for the Tamames limestones.

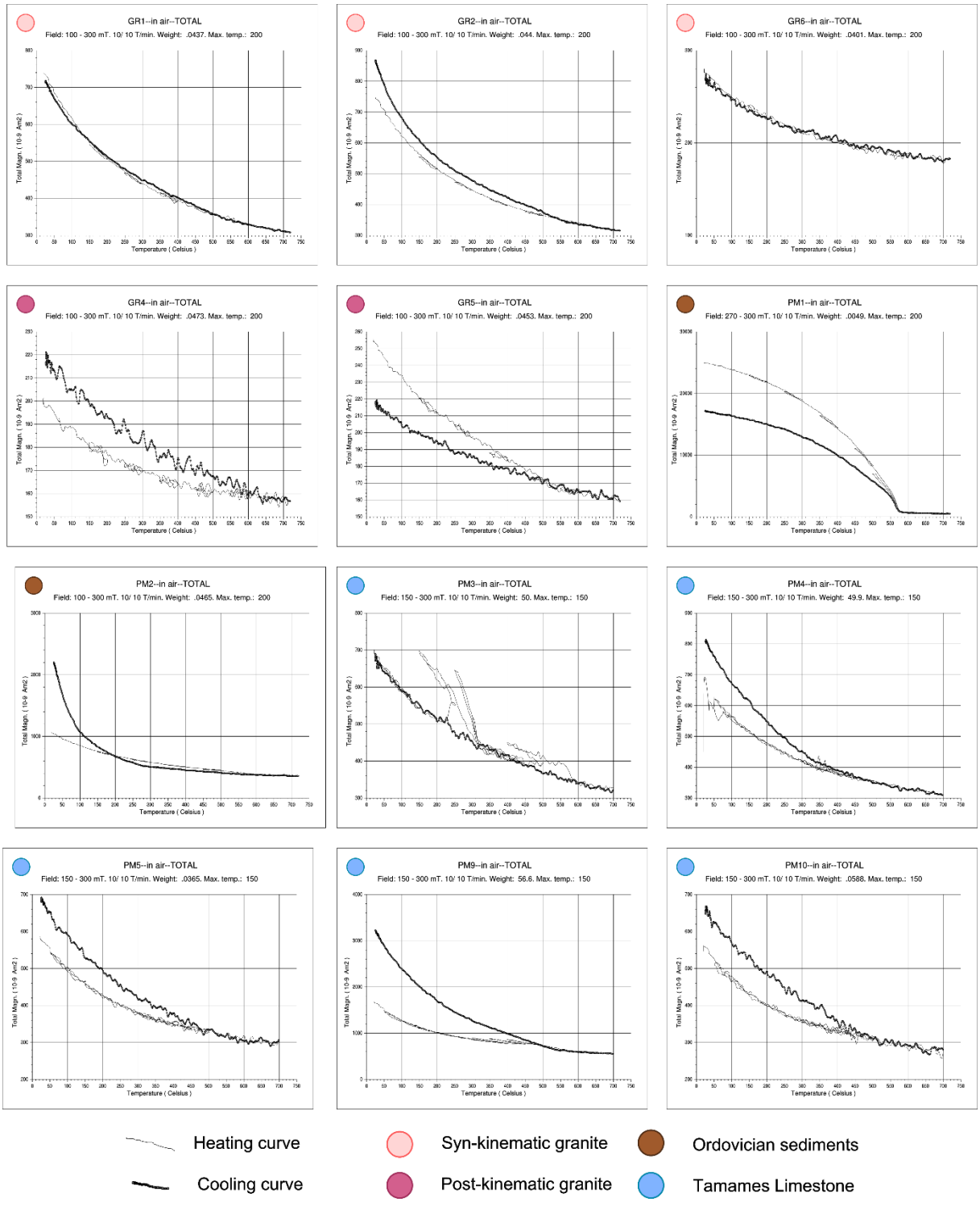

Appendix C: Zijderveld diagrams

This appendix shows examples of Zijderveld diagrams. Each site is represented by a good result on the left, and a bad result on the right. Coloured dots follow the same coding as appendix B. The term good is used if there is a clear signal, which can preferably be interpreted as a line or otherwise a greatcircle. A result is bad if the direction from the sample is unclear, or if the Zijderveld diagrams shows directions changing at each demagnetization step.

GR1

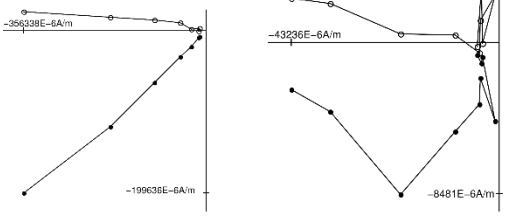

GR2

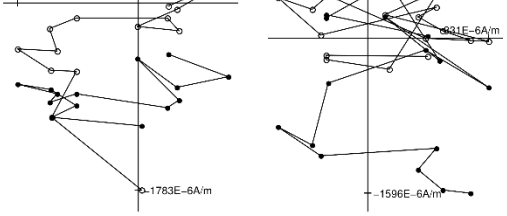

GR3

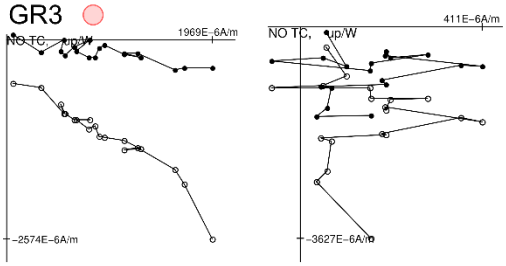

GR6

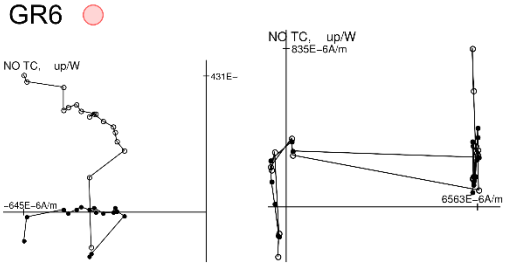

GR7

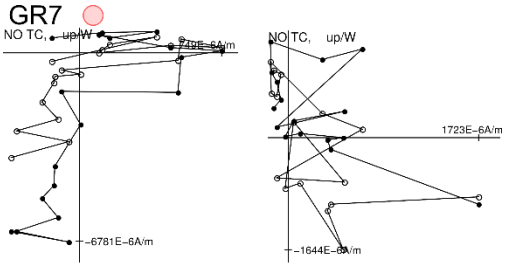

GR8

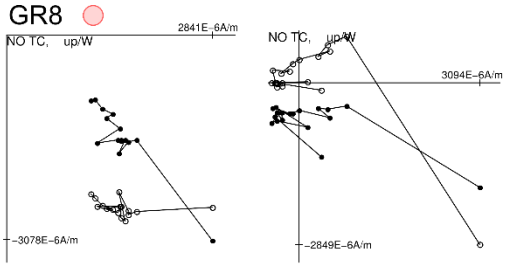

GR9

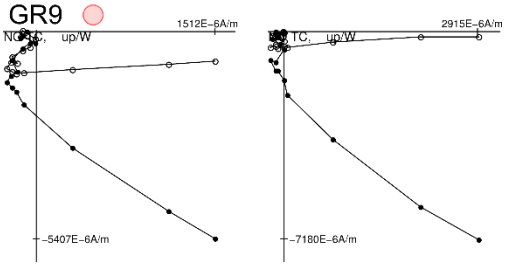

GR9B

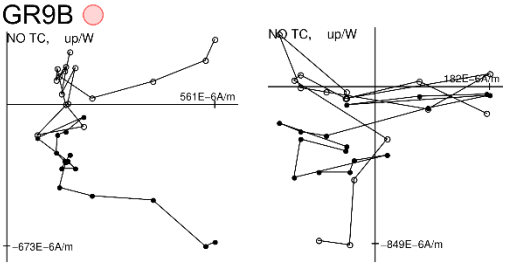

GR10

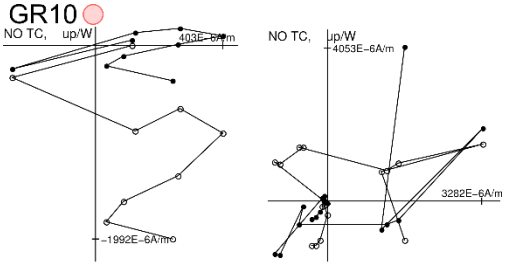

GR11

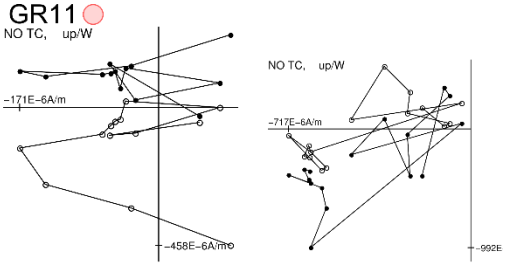

GR12

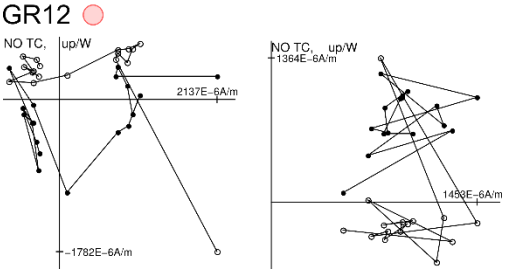

GR4

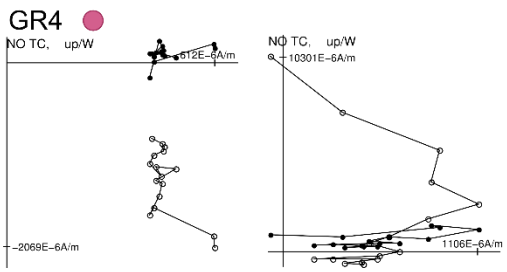

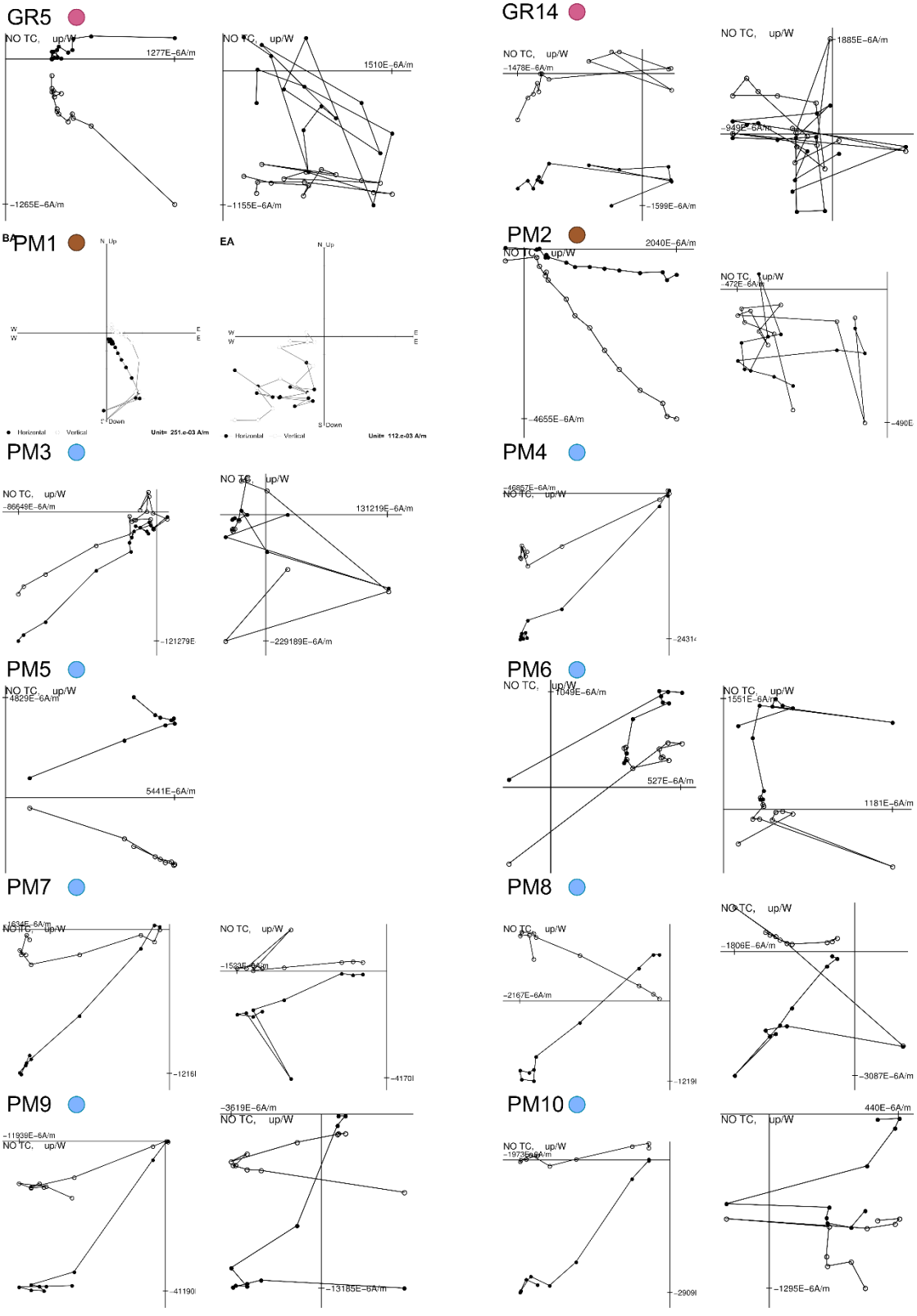
GR5
NO TC, up/W
1277E-6A/m
-1265E-6A/m
NO TC, up/W
1510E-6A/m
-1155E-6A/m
GR14
NO TC, up/W
-1478E-6A/m
-1599E-6A/m
NO TC, up/W
1885E-6A/m
-939E-6A/m
BA PM1
N Up
W
E
S Down
Horizontal
Vertical
Unit= 251.e-03 A/m
EA
N Up
W
E
S Down
Horizontal
Vertical
Unit= 112.e-03 A/m
PM2
2040E-6A/m
NO TC, up/W
-4655E-6A/m
NO TC, up/W
-472E-6A/m
-490E
PM3
NO TC, up/W
-86649E-6A/m
-121279E
NO TC, up/W
131219E-6A/m
-229189E-6A/m
PM4
-48657E-6A/m
NO TC, up/W
-2431
PM5
NO TC, up/W
-4829E-6A/m
5441E-6A/m
PM6
NO TC, up/W
-10499E-6A/m
527E-6A/m
NO TC, up/W
1551E-6A/m
1181E-6A/m
PM7
-1634E-6A/m
NO TC, up/W
-1216
NO TC, up/W
-1593E-6A/m
-4170
PM8
NO TC, up/W
-2167E-6A/m
-1219
NO TC, up/W
-1806E-6A/m
-3087E-6A/m
PM9
-11939E-6A/m
NO TC, up/W
-4119
-3619E-6A/m
NO TC, up/W
-13185E-6A/m
PM10
NO TC, up/W
-1973E-6A/m
-2909
440E-6A/m
NO TC, up/W
-1295E-6A/m

Appendix D: Greatcircle fits

This appendix shows examples of some results that were interpreted using the greatcircle method. The figure represents how I fitted the greatcircle through the data points

GR2_QB

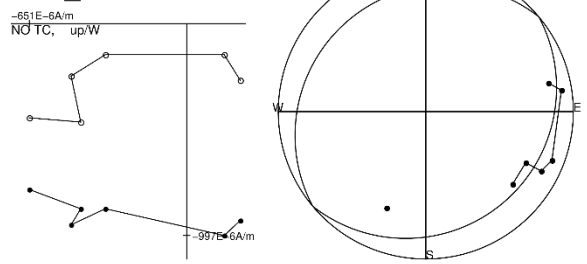

GR3_HA

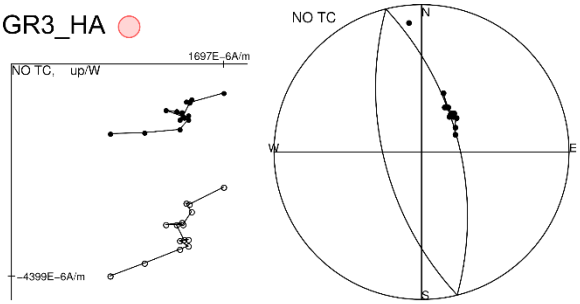

GR6_FA

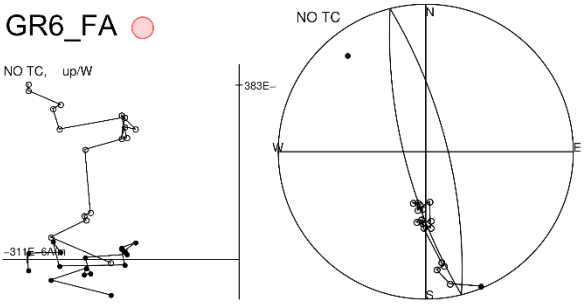

GR7_GA

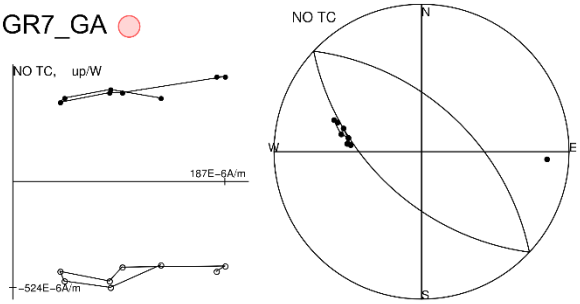

GR8_K

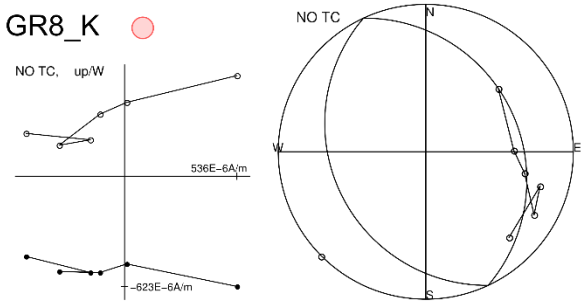

GR9_E

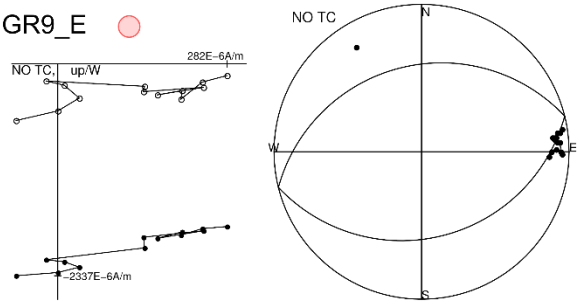

GR9b_GA

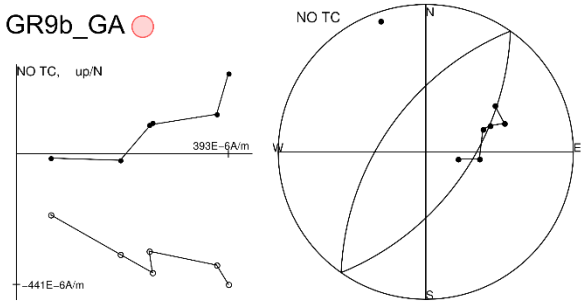

GR10_B

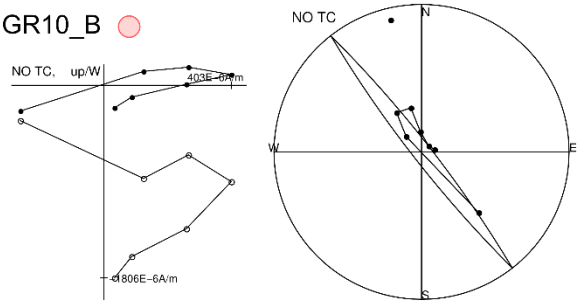

GR11_E

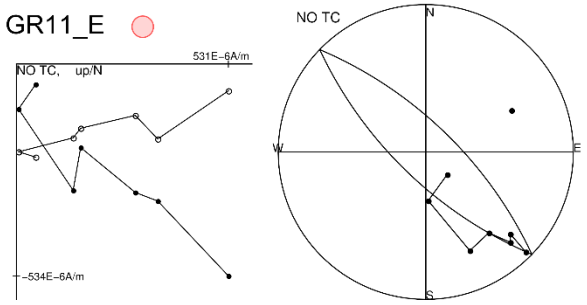

GR12_A

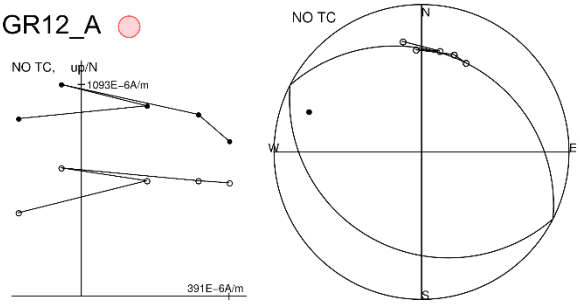

GR4_FB

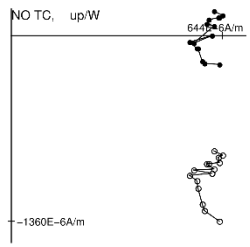

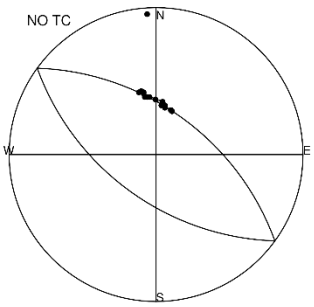

GR5_HA

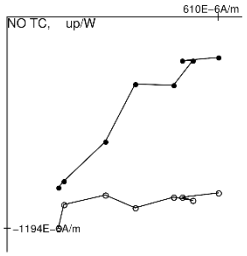

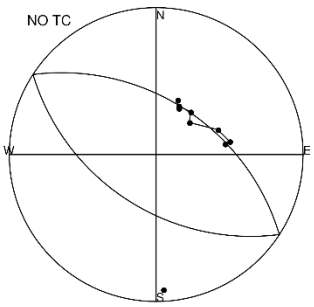

GR14_BA

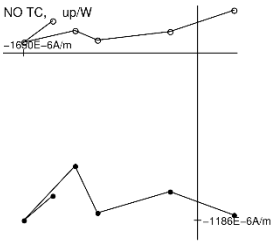

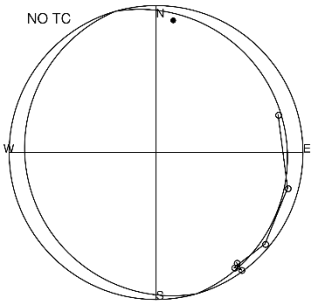

PM1_FA

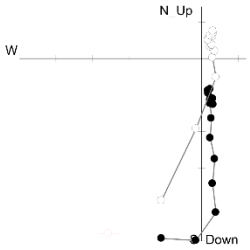

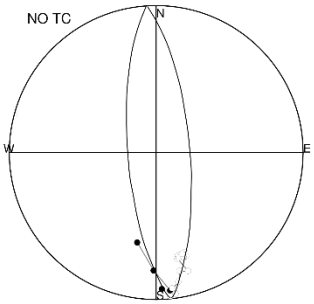

PM2_CA

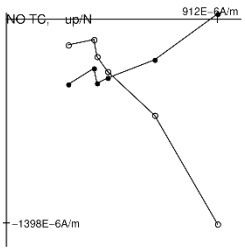

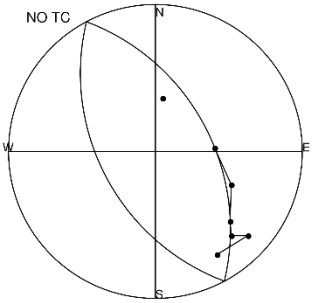

PM6_GA

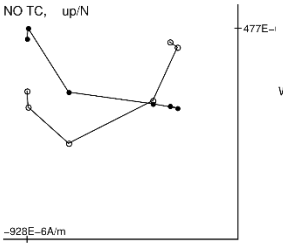

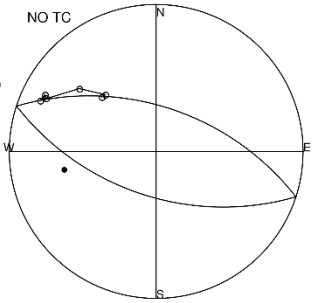

PM8_4

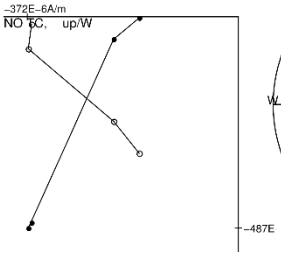

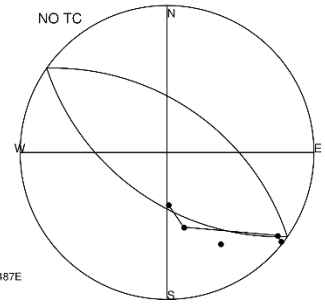

Appendix E: PalFit results

This appendix shows equal area plots of the results of the PalFit program for each site. PalFit fits the best fitting point on a greatcircle with all other data points of that site. Colours of the dots according to appendix B.

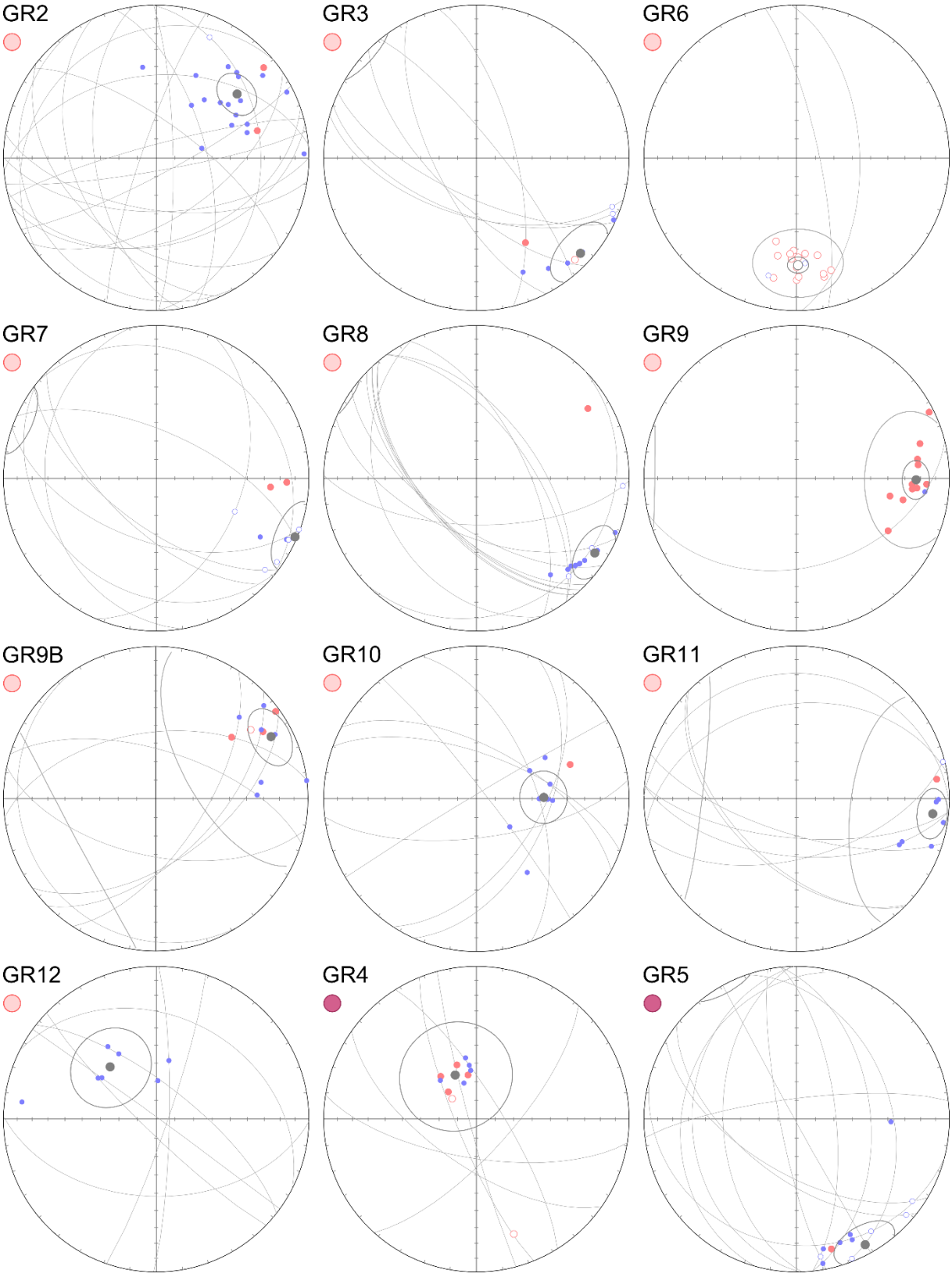

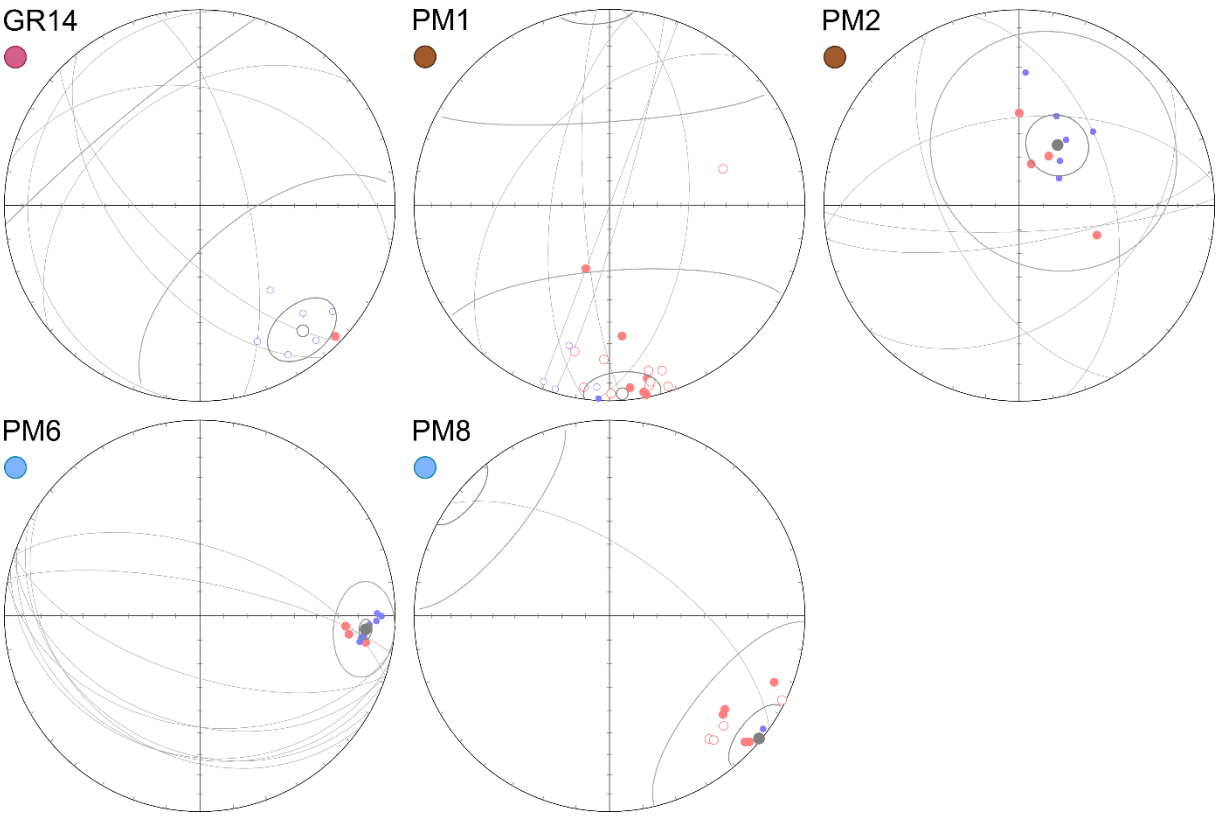
GR14
PM1
PM2
PM6
PM8

Appendix F: 45-degree cutoff results

This appendix shows the result of the 45 degree cutoff, for each individual site. There are two plots per site, the left plot shows the VGP while the right plot shows an equal area projection of the directions. Data points that were outside of the 45 degree are coloured red, and these points are not used for calculating the average directions. Coloured dots following appendix B.

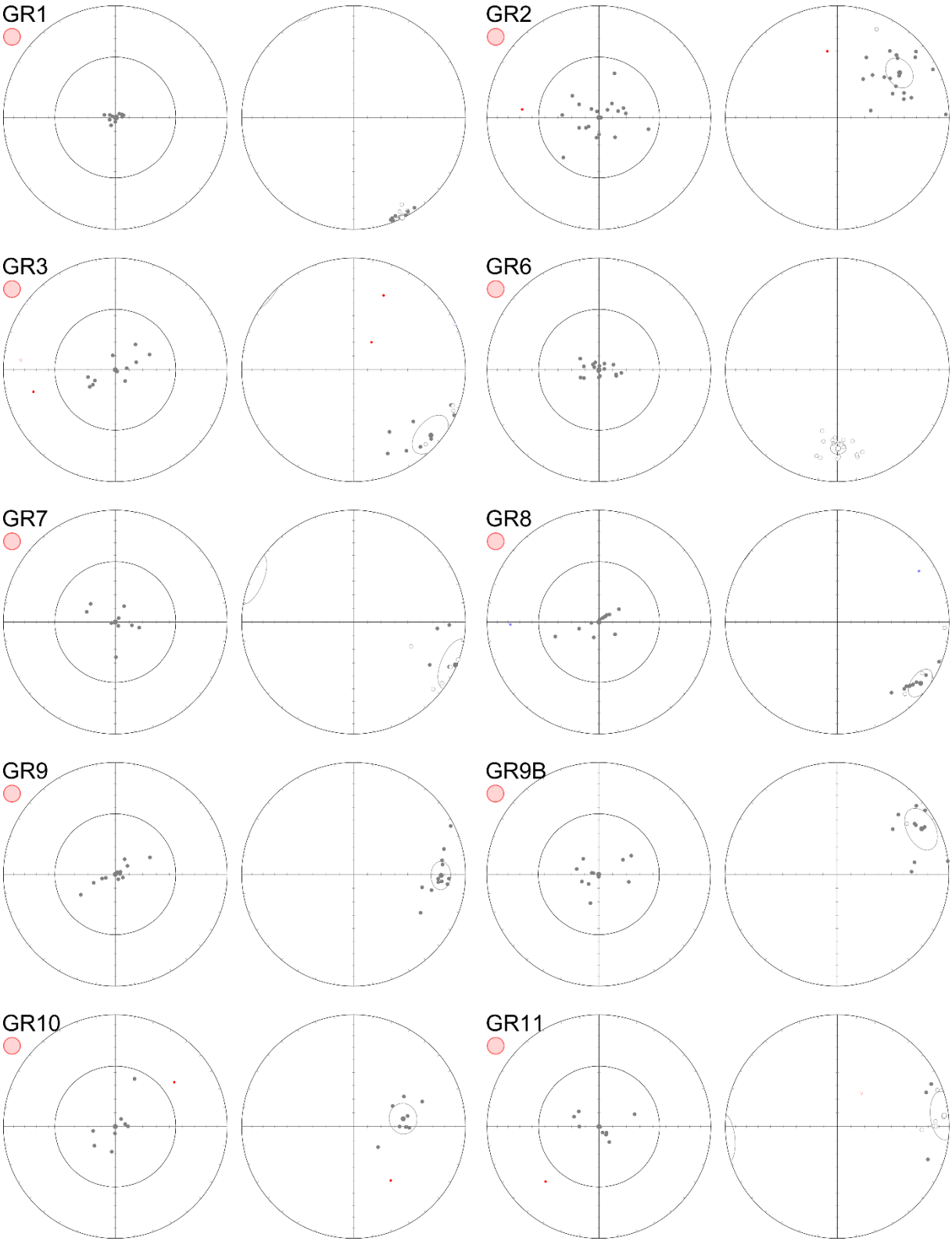

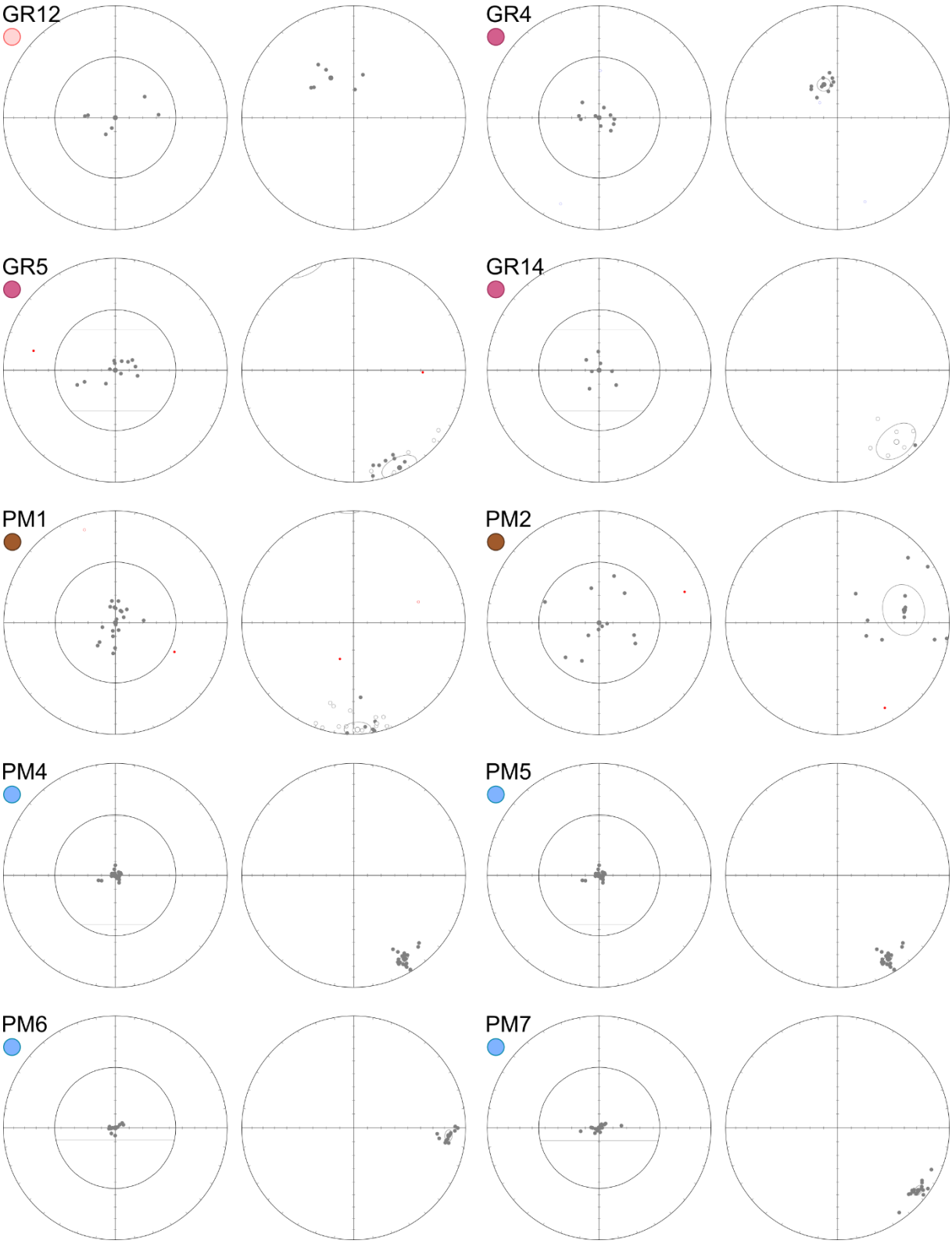
GR12
GR4
GR5
GR14
PM1
PM2
PM4
PM5
PM6
PM7

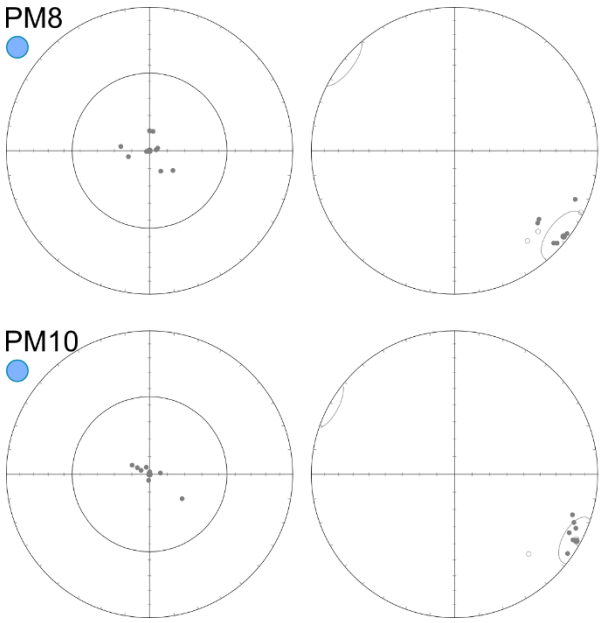
PM8

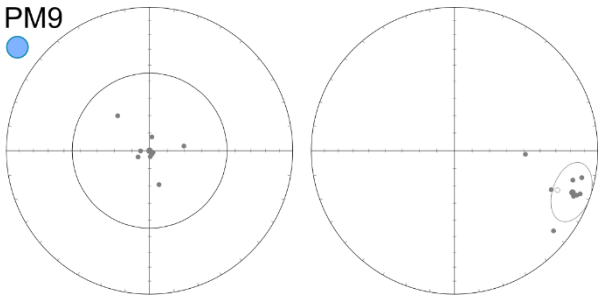
PM9

PM10

Appendix G: Mullion spacing

The spacing of the D_x mullions was calculated from a drawing of the tracings of the mullions. This data could not be used in this project, since a complete analysis of the mullions requires more data on their exact geometry, and this was outside of the scope of this project.

The mullion spacing was calculated from a photograph which also contains a scale bar of known size, and tracings were drawn for each mullion (*figure G-1*). The short axis of the best fitting ellipse for each individual mullion, which is a measure of the spacing, was calculated using the image processing software ImageJ.The spacing follows a log-normal distribution (*figure G-2*), as in other geological features (Budd & Peletier 2000; Pastor-Galán et al. 2009). The spacing ranges from 0.1 centimetres to 15,7 centimetres, with a mean spacing of 3,5 centimetres.

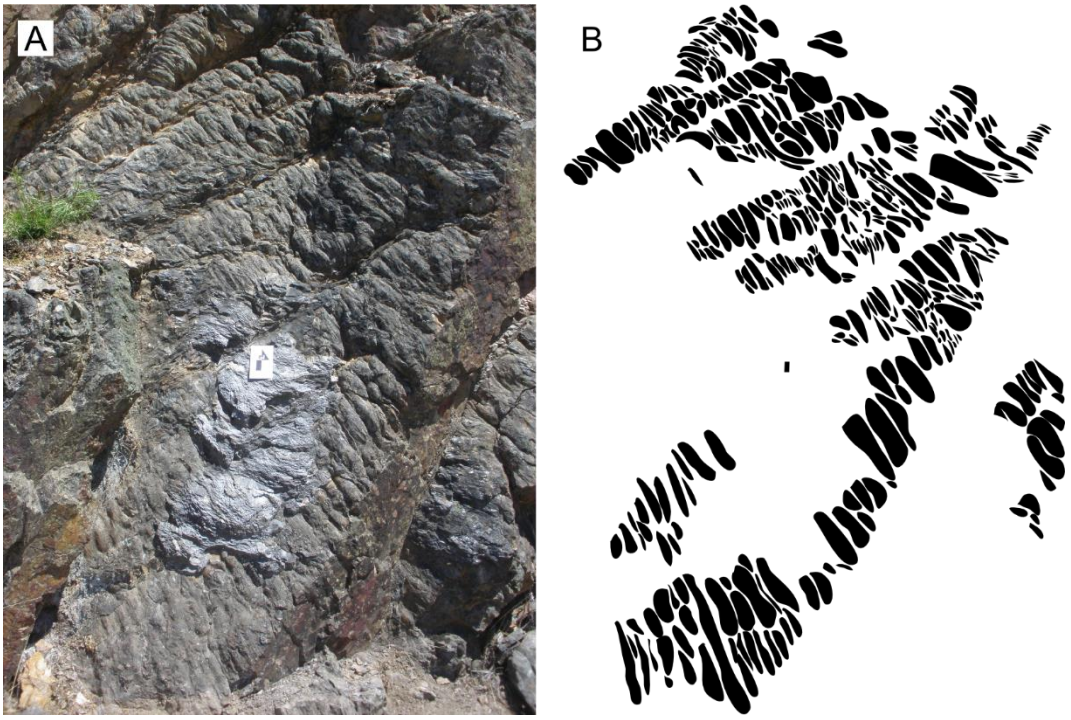

Figure G-1. A) field picture of quartzite layer with mullions and scale-bar. B) tracings of each individual mullion.

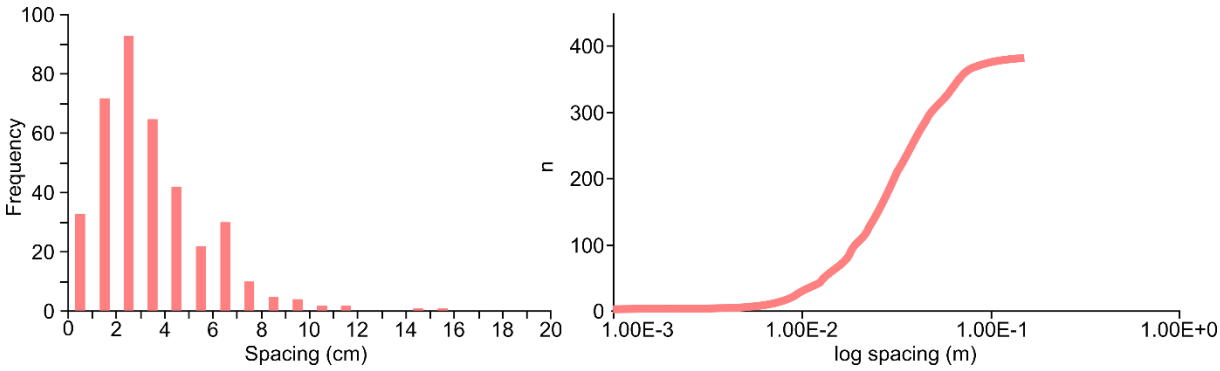

Figure G-2. Distribution of the mullion spacing, which follows a log-normal distribution.

Appendix H: Thin section analysis

Information and pictures of the thin-sections that were studied for the structural analysis. The left column contains the name of the thin-section, if the labels A, B and/or C are present, more thin-sections were taken from the same handsample. The lab arrow and the coloured lines give an overview of the orientation, which is presented as a projection relative to the nort. The bar diagram indicates the relative abundance of the different minerals. The pictures, with scale bar, are used to illustrate what the different foliations look like. The orange lines represent S_{1+3}, while the red lines represent S_2.

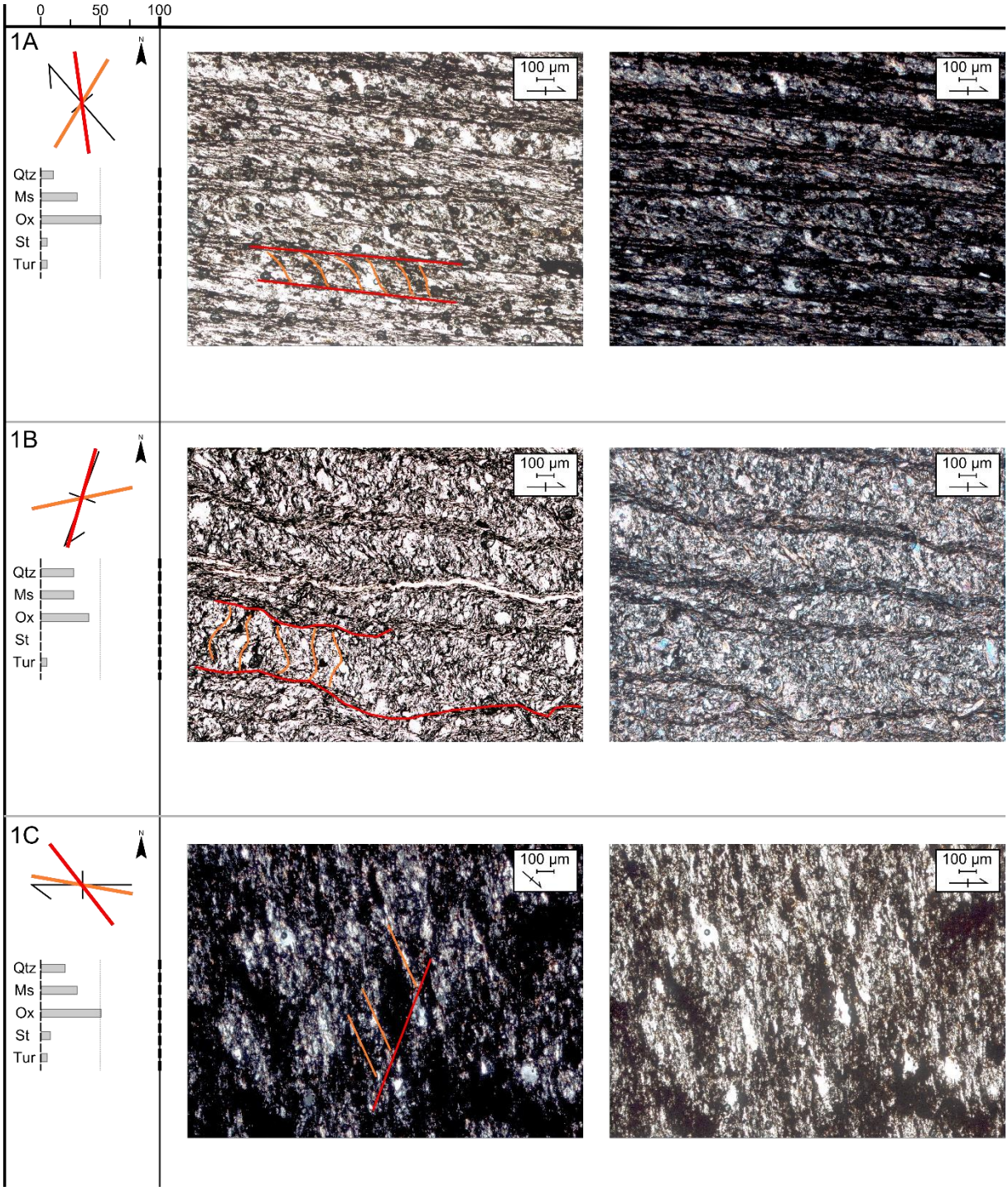

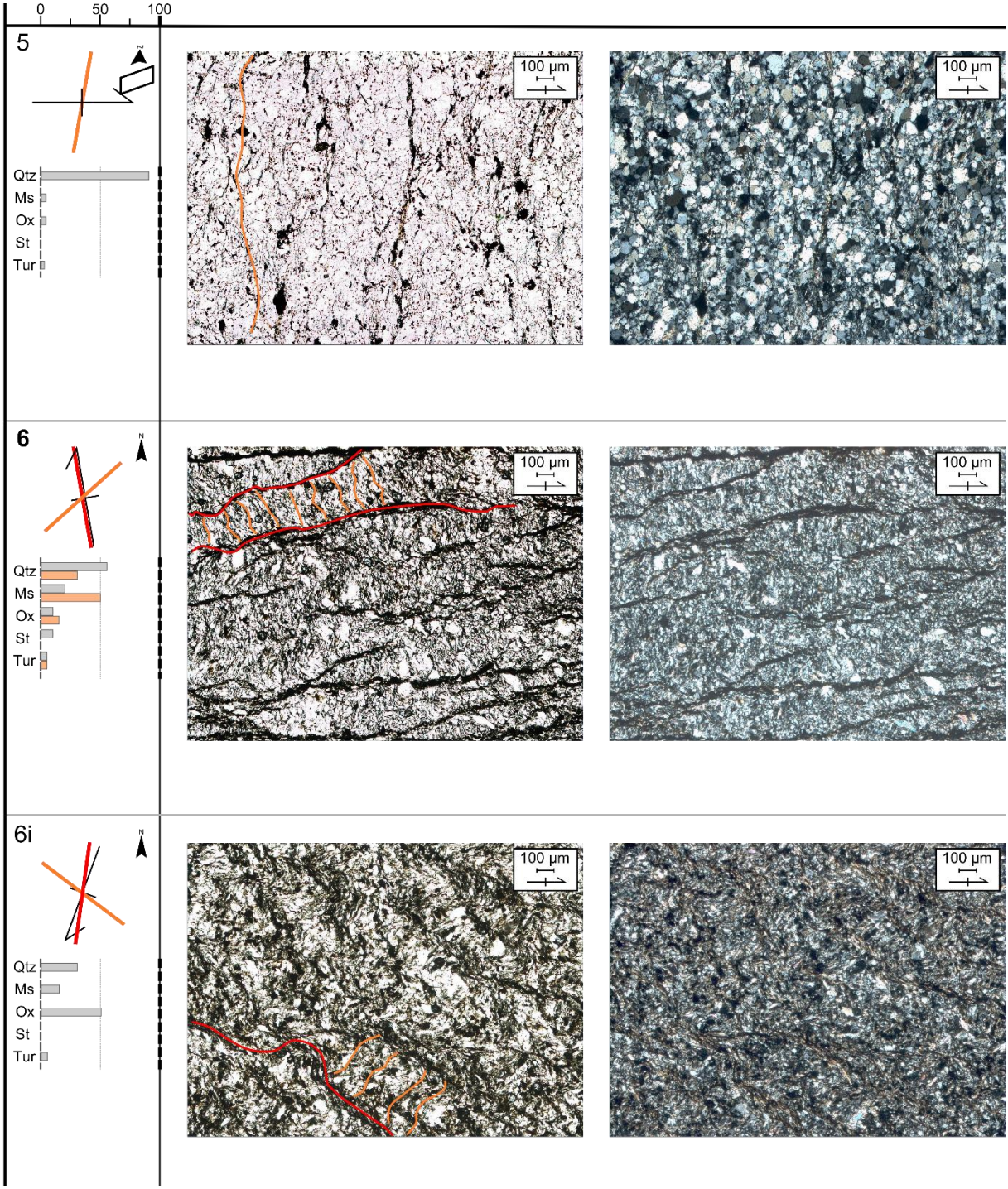
0
50
100
5
Qtz
Ms
Ox
St
Tur
100 µm
100 µm
6
Qtz
Ms
Ox
St
Tur
100 µm
100 µm
6i
Qtz
Ms
Ox
St
Tur
100 µm
100 µm

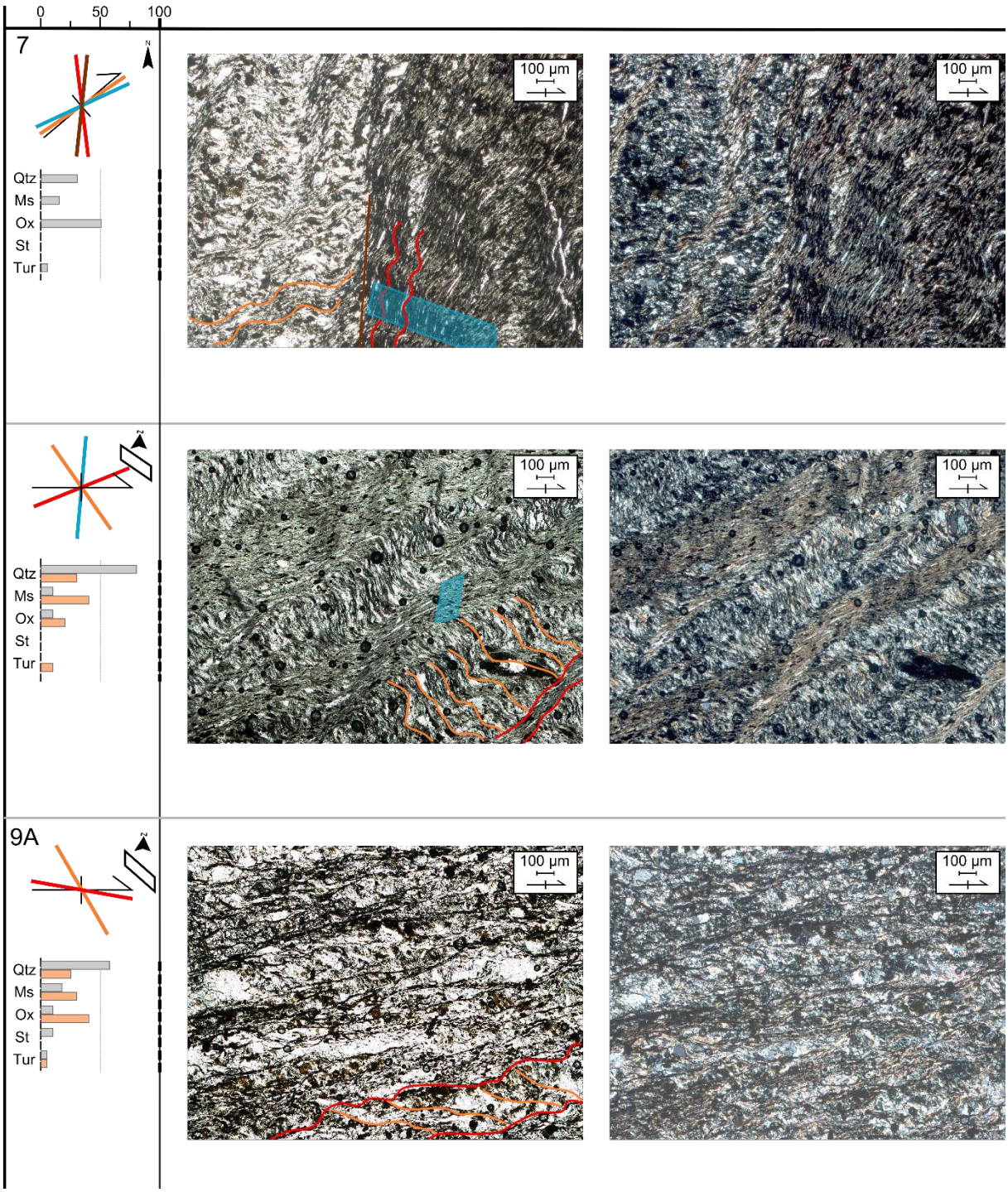
0
50
100
7
N
Qtz
Ms
Ox
St
Tur
100 µm
100 µm
N
Qtz
Ms
Ox
St
Tur
100 µm
100 µm
9A
N
Qtz
Ms
Ox
St
Tur
100 µm
100 µm

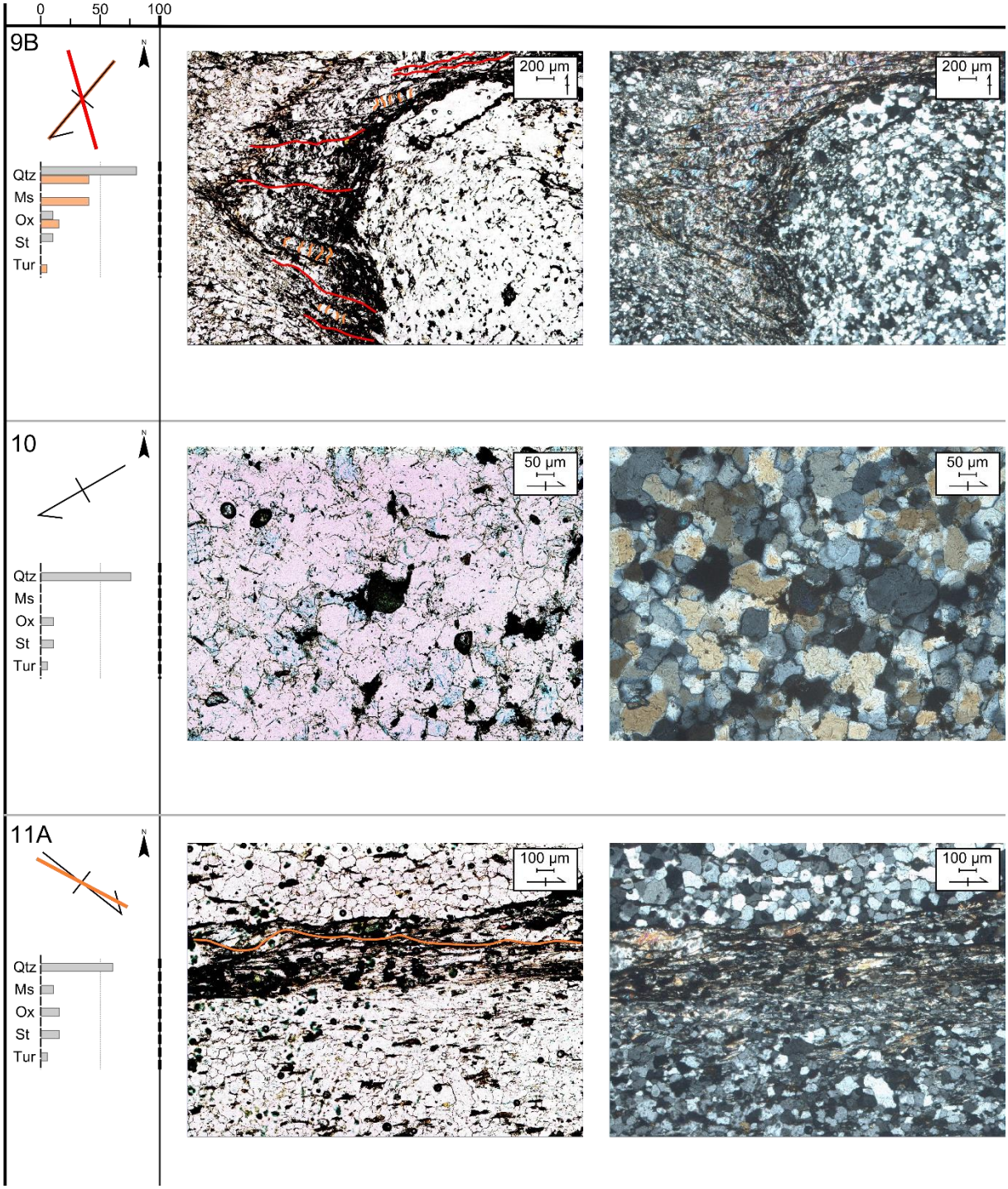
0
50
100
9B
N
Qtz
Ms
Ox
St
Tur
200 µm
200 µm
10
N
Qtz
Ms
Ox
St
Tur
50 µm
50 µm
11A
N
Qtz
Ms
Ox
St
Tur
100 µm
100 µm

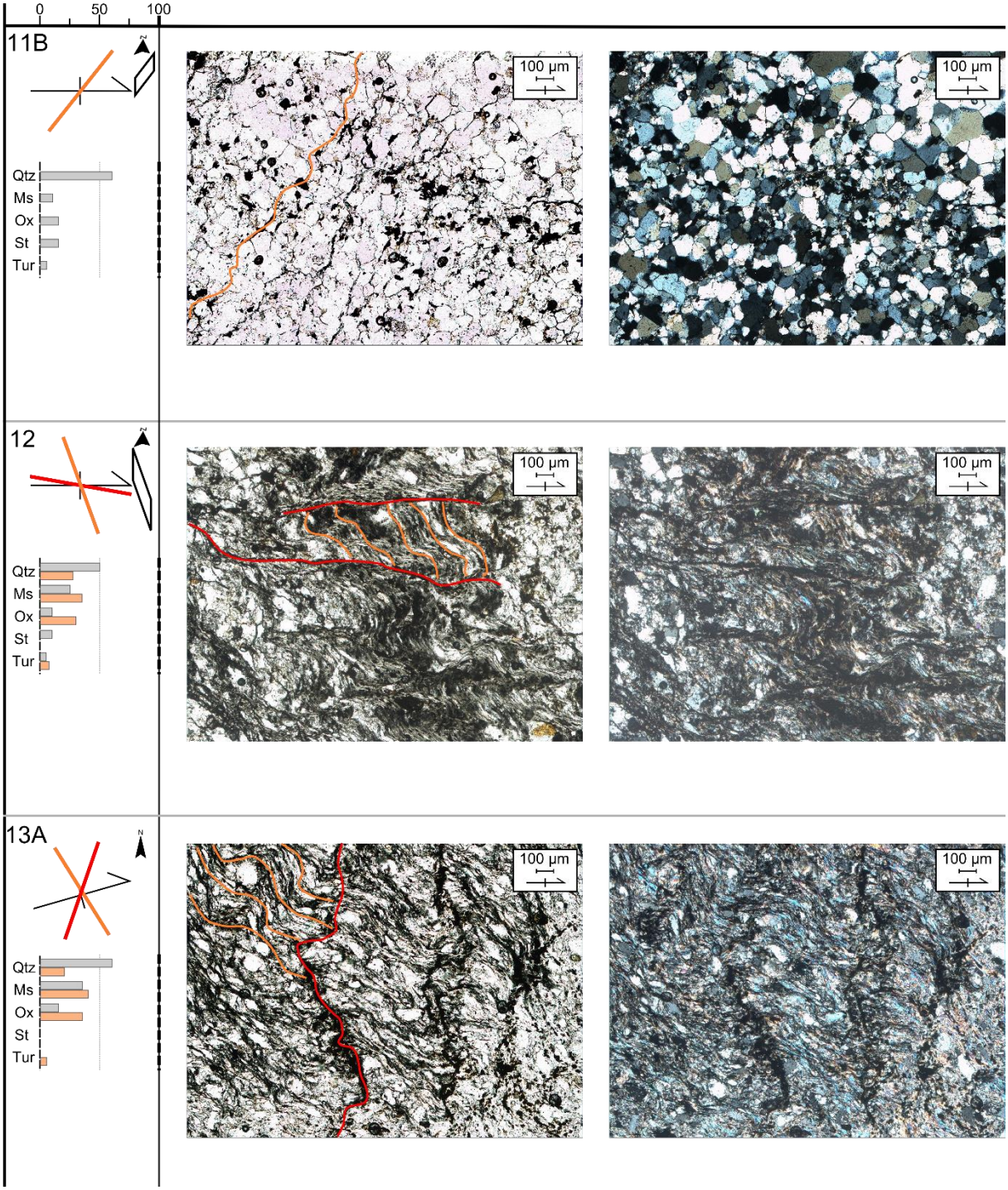
0
50
100
11B
N
Qtz
Ms
Ox
St
Tur
100 µm
100 µm
12
N
Qtz
Ms
Ox
St
Tur
100 µm
100 µm
13A
N
Qtz
Ms
Ox
St
Tur
100 µm
100 µm

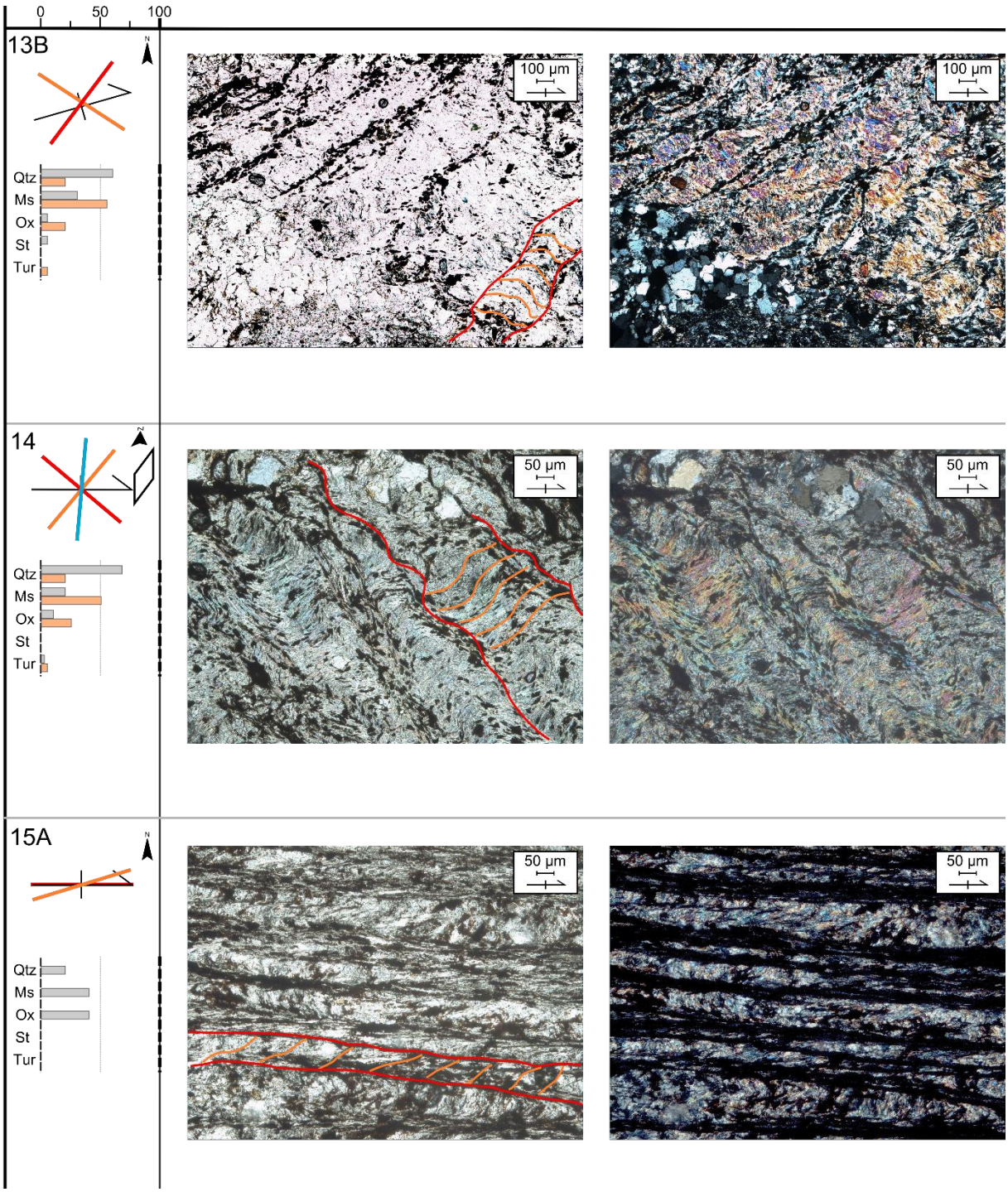
0
50
100
13B
N
Qtz
Ms
Ox
St
Tur
100 µm
100 µm
14
N
Qtz
Ms
Ox
St
Tur
50 µm
50 µm
15A
N
Qtz
Ms
Ox
St
Tur
50 µm
50 µm

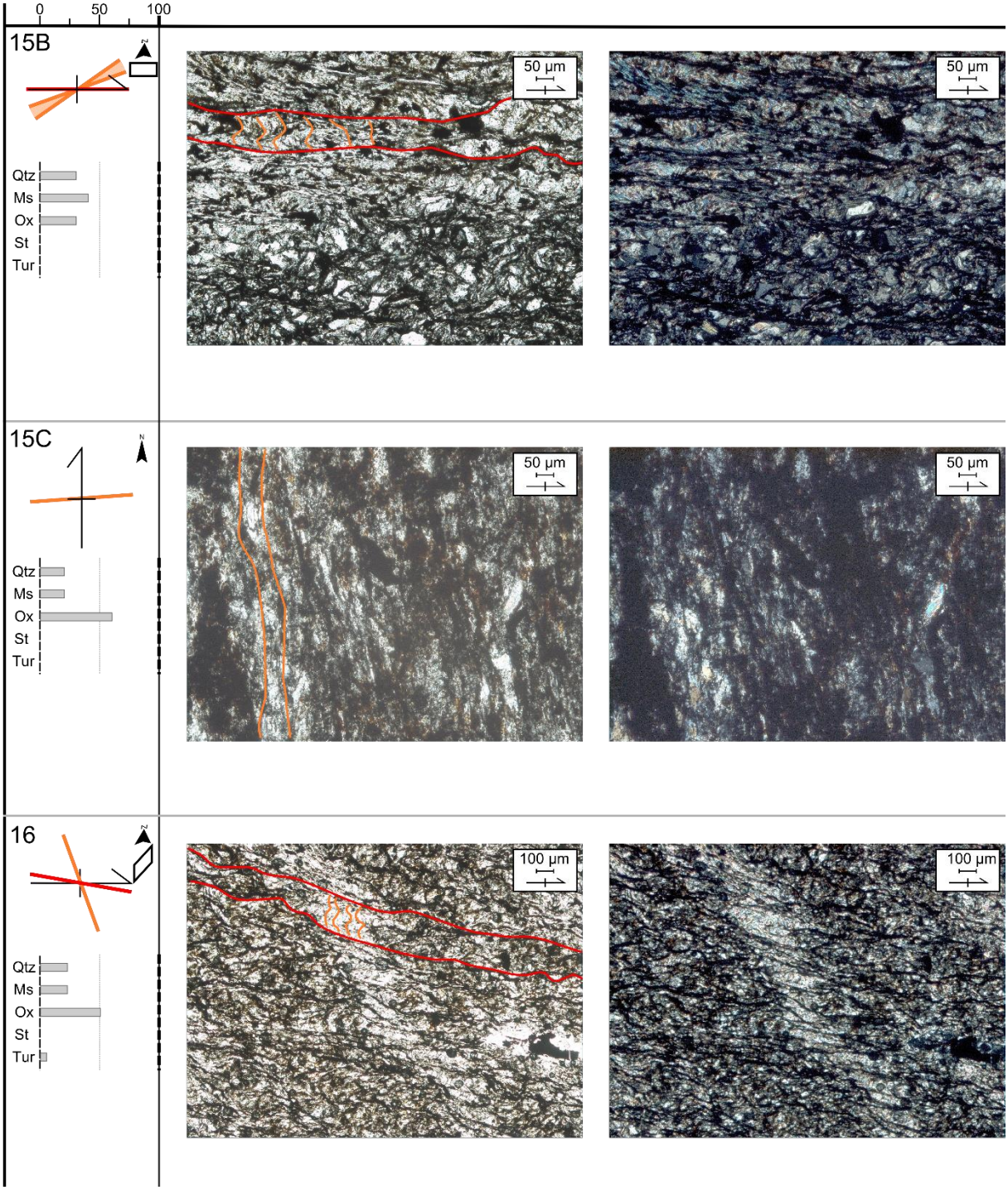
0
50
100
15B
Qtz
Ms
Ox
St
Tur
50 µm
50 µm
15C
Qtz
Ms
Ox
St
Tur
50 µm
50 µm
16
Qtz
Ms
Ox
St
Tur
100 µm
100 µm

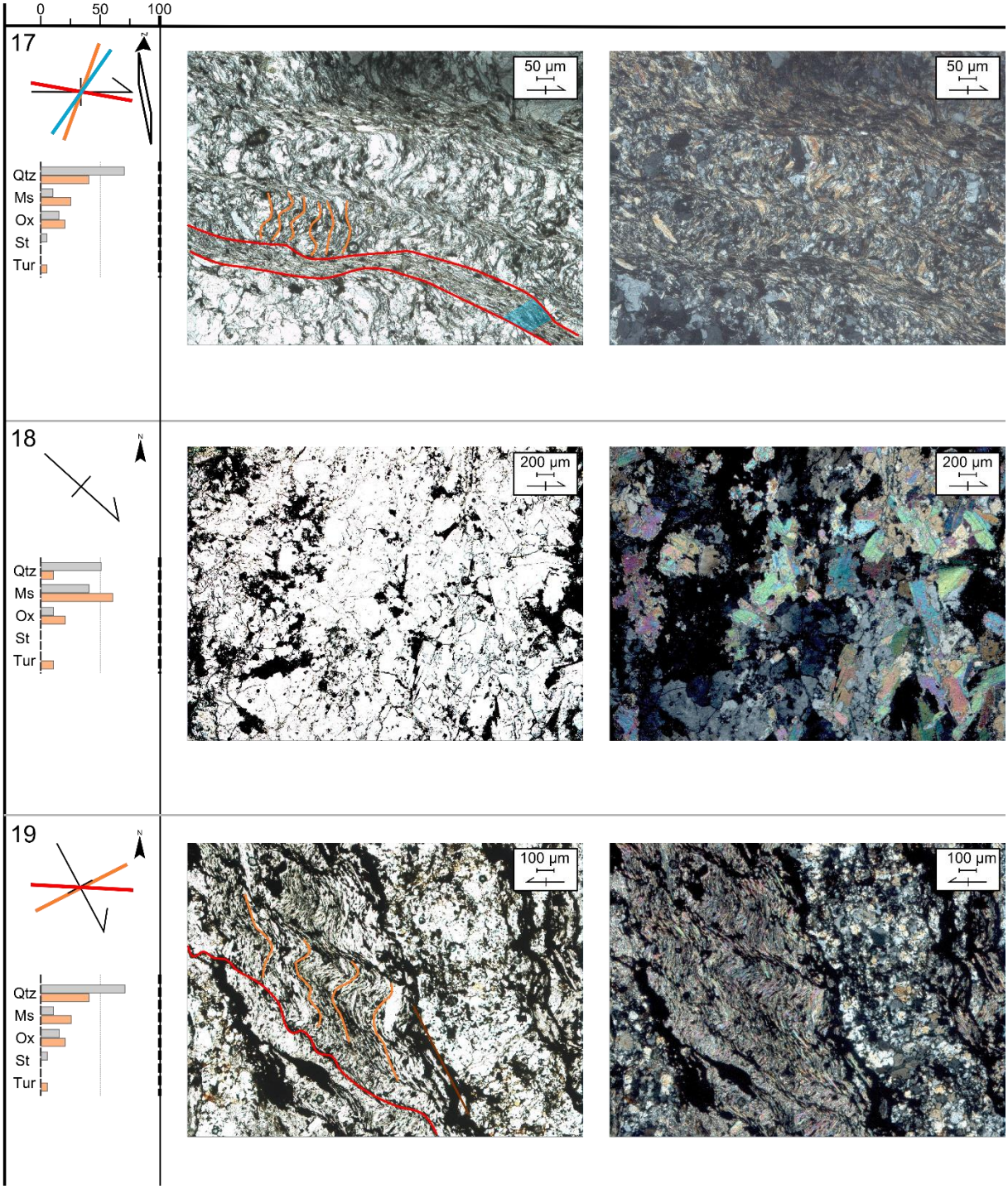
0
50
100
17
Qtz
Ms
Ox
St
Tur
50 µm
50 µm
18
N
Qtz
Ms
Ox
St
Tur
200 µm
200 µm
19
N
Qtz
Ms
Ox
St
Tur
100 µm
100 µm